Innovative Organic Electroluminescent Devices: Diarylethenes as Light-responsive Switches and Emissive Graphene Quantum Dots

Giovanni Francesco Cotella

London Centre for Nanotechnology and

University College London - UCL

A dissertation submitted for the degree of Doctor of Philosophy

September 2019

I, Giovanni F. Cotella, confirm that the work presented in this thesis is my own. Where information has been derived from other sources and work which has formed part of jointly-authored publications, I confirm that this has been indicated in the thesis.

To my lovely wife Imma

To my family

To my homeland

Acknowledgements

My research was totally funded by the European Commission Horizon 2020 Research and Innovation programme (2014-2020) under the Marie Sklodowska-Curie Initial Training Network, Grant Agreement No. 642196 (iSwitch).

Firstly I want to thank my supervisor Prof. Franco Cacialli for giving me the opportunity to join his research group at UCL, for his inspiration and guidance.

Thanks to my second supervisor Prof. Hugo Bronstein, for his support. I would like to express my gratitude to all the collaborators and members of the iSwitch ITN network that made this work possible. In particular, a special thanks goes to the project coordinator Prof. Paolo Samorí and the project manager Dr. Nicolas Weibel, then to Dr. Aurelio Bonasera, Prof. Stefan Hecht, Dr. Lili Hou, Marco Carroli, Dr. Agostino Galanti, Dr. Akimitsu Narita, Prof. Klaus Müllen, Dr. Giovanni Ligorio, Ana Margarida Gama Santiago da Silva, Dr. Peter Erk, Dr. Jasmine Santoro, Dr. Michal Valášek, Dr. Thomas Mosciatti, Vitaly Parkula, Dr. Pierpaolo Greco, Dr. Giuseppe Paternó, Dr. Valentina Robbiano and Prof. Francesco Scotognella.

I am enormously grateful to my colleagues and members of the 'Organic semiconductors and nanostructures' group at UCL. In particular to: Dr. Giuseppe Carnicella, Dr. Alessandro Minotto, Tecla Arcidiacono, Dr. Andrea Zampetti, Dr. Alexandros Rapidis and Ioannis Ierides. We faced daily technical and personal challenges and, together, we managed to overcome them.

Last but not least, I am grateful to UCL, the London Centre for Nanotechnology, the City of London and the United Kingdom which kindly adopted me, taught me and shaped my personality over the last four years.

Abstract

The awarding in 2016 of the Nobel Prize in Chemistry to prof. J. Sauvage, J. F. Stoddart and B. L. Feringa, "for the design and synthesis of molecular machines" proves the interest of the scientific community and high-tech industry towards stimuli-responsive multifunctional materials and devices. In this direction, the research activity described in this thesis is focused on light-responsive emissive devices, which can be controlled remotely and reversibly via irradiation with light of specific wavelengths. A range of photochromic diarylethene derivatives were judiciously selected in combination with commercially available organic semiconductors to generate the light-responsivity in our devices.

At first, optically switchable green-emitting OLEDs and micro-OLEDs were investigated achieving the maximum ON/OFF ratio of ~20 and ~90 for current density and luminance, respectively. Additionally, through the studying of the performance of light-responsive single carrier devices, it was demonstrated that electrons are more affected than holes by the switching of the photo-active dopant.

The device emissive area was further scaled-down working on the characterization of light-emitting transistors (OLETs) having channel length of 2.5 μm. For the first time such devices covered the whole visible spectrum and a maximum ON/OFF ratio exceed 500 was achieved for both drain current and luminance.

Finally, another macro-trend of the display community was addressed, the constant search for innovative chromophores as alternative to poorly stable and highly expensive iridium-based phosphorescent materials or highly toxic cadmium-based colloidal quantum dots. In this direction, air stable and potentially non-toxic red-emitting graphene quantum dots (GQDs) were embedded in electroluminescent devices. The LEDs showed high colour

purity (FWHM= 30 nm), maximum luminance of 1300 cd/m^2 and EQE of 0.67 % which are among the best performance ever reported for LEDs based on red-emitting GQDs.

Table of Contents

List of Figures

List of Abbreviations

AFM	Atomic force microscopy
CCD	Charge-coupled device
DBOV	Dibenzo[hi,st]ovalene
DAE	Diarylethene
EET	Electronic energy transfer
EL	Electroluminescence
EQE	External quantum efficiency
ETL	Electron transport layer
F8BT	Poly[(9,9-di-n-octylfluorenyl-2,7-diyl)-alt-(benzo[2,1,3]thiadiazol-4,8-diyl)]
F8T2	Poly(9,9-dioctylfluorene-alt-bithiophene)
F8	Poly(9,9-di-n-octylfluorenyl-2,7-diyl)
FC	Franck-Condon
FRET	Förster resonance energy transfer
GQD	Graphene quantum dot
HOMO	Highest occupied molecular orbital
HTL	Hole transport layer
ITO	Indium tin oxide
JVL	Current density-luminance vs voltage

LED	Light-emitting diode
LUMO	Lowest unoccupied molecular orbital
LRD	light-responsive device
MDMO-PPV	Poly[2-methoxy-5-(3′,7′-dimethyloctyloxy)-1,4-phenylenevinylene]
NIR	Near infrared
OLED	Organic light-emitting diode
OLET	Organic light-emitting transistor
OSOLED	Optically switchable OLED
OSOLET	Optically switchable OLET
OTFT	Organic thin film transistors
PEDOT:PSS	Poly(3,4-ethylenedioxythiophene)-poly(styrenesulfonate)
PL	Photoluminescence
PLQY	Photoluminescence quantum yield
PS	Polystyrene
PSS	Photostationary state
TCSPC	Time-correlated single-photon counting
VLC	Visible light communication

List of Publications

- Hou L., X. Zhang, G. F. Cotella, G. Carnicella, M. Herder, B. M. Schmidt, M. Pätzel, S. Hecht, F. Cacialli, and P. Samorì, "Optically switchable organic light-emitting transistors," Nat. Nanotechnol., vol. 14, no. 4, pp. 347–353, Apr. 2019.G.F.
- Ligorio G., G. Cotella, A. Bonasera, N. Z. Morales, G. Carnicella, B. Kobin, Q. Wang, N. Koch, S. Hecht, E. J.W. List-Kratochvil and F. Cacialli, "Modulating the luminance of organic light emitting diodes via optical stimulation of a photochromic molecular monolayer at transparent oxide electrode", submitted.
- Robbiano V., G. M. Paternò, G. F. Cotella, T. Fiore, M. Dianetti, M. Scopelliti, F. Brunetti, B. Pignataro, and F. Cacialli, "Polystyrene nanoparticle-templated hollow titania nanosphere monolayers as ordered scaffolds," J. Mater. Chem. C, vol. 6, no. 10, pp. 2502–2508, Mar. 2018.
- Ciesielski A., S. Haar, A. Aliprandi, M. El Garah, G. Tregnago, G. F. Cotella, M. El Gemayel, F. Richard, H. Sun, F. Cacialli, F. Bonaccorso, and P. Samorì, "Modifying the Size of Ultrasound-Induced Liquid-Phase Exfoliated Graphene: From Nanosheets to Nanodots," ACS Nano, vol. 10, no. 12, pp. 10768–10777, Dec. 2016

1 Impact Statement

Today devices based on organic thin film technologies are on the market and are expected to increase their economic impact in the upcoming years [1]. Displays based on organic light-emitting diodes (OLEDs) are constantly subtracting market share to the screens based on standard liquid crystals technology. Differently, the technology based on organic thin film transistors (OTFT) is close to its maturity and it might serve areas, such as wearable and flexible electronics.

An emerging and intriguing research branch involving organic thin film technologies focuses on the design and fabrication of responsive devices, able to react, changing their working regime, to external stimuli. Among the others, the ability to control a device via light irradiation could allow to control devices remotely, reversibly generate arbitrary patterns on the emissive area, and combine in a single device both the emission and the sensing of light, a desirable feature in visible light communication (VLC) technology. Organic semiconductors are naturally suited for light-responsive devices (LRDs) fabrication thanks to the large flexibility of their properties and processing methods [2]–[6] [7]–[13].

In organic thin film devices the light-responsivity can be generated by embedding in one of the functional layers a photochromic compound, whose isomers are able to induce a different macroscopic effect on the device performance. In this scenario, the most prominent class of photochromic dopants are the diarylethenes (DAEs) derivatives, see section 2.5. Their success is due to three factors: (i) the vastly different optical, electrical and energetic properties between the two, thermally stable, isomers; (ii) the high reversibility and fatigue resistance of the photochemical reaction; and (iii) the large versatility of the DAEs chemical structure which allows fine tuning of the molecule

properties.

The work presented in this thesis investigates further the interaction of DAE molecules with organic semiconductors. Initially, for each system investigated, the retention of the dopant photochromic activity in the solid state has been investigate via both absorption and photoluminescence spectroscopy. Finally, both two- and three-terminal optically-switchable emitting devices, namely OLEDs and, for the first time, organic light-emitting transistors (OLETs), were designed, fabricated and characterized. We studied this interaction in both macroscopic and microscopic devices. Given the unconventional device behaviour, specific characterization setup and data elaboration scripts were built. For the first time, the effect of the DAEs isomerization on the transport of both the charge carriers has been directly assessed via the characterization of specifically designed hole-only and electron-only devices.

In addition, to address the constant research on innovative chromophores, we investigated electroluminescent devices based on a new class of air-stable and non-toxic red-emitting graphene quantum dots (GQDs). Such devices showed performance among the highest ever reported for this class of materials.

The information gathered in this thesis supports and enrich previous results on light-responsive devices toward a more complete understanding of the semiconductor-photochromer interaction thus favouring the development of such innovative devices. The development of the red-emitting GQDs-based LEDs paves the way to the use of this air stable, heavy-metal-free and biocompatible emitting materials for future lighting and display technologies.

Overview of the thesis

This thesis work is structured in six chapters. The first two chapters provide the background knowledge sufficient to achieve a clear understanding of the rest of the thesis. Indeed, here the fundamental properties of materials, devices and investigation techniques involved in the experimental activity, are described. The remaining three experimental chapters cover the design and fabrication of different electroluminescent devices, light-responsive or based on innovative emitting materials. Detailed description of the content of each section are given as follows.

Chapter 1 focuses on the theoretical description of the properties of materials and devices involved in this work. Here the fundamental properties of organic semiconductors are discussed, with particular emphasis on optical and electronic aspects. Here we cover the basic mechanisms involved in the charge transport and light generation in organic semiconductors. Another emerging class of conjugated emitting material is briefly described here, the graphene quantum dots (GQDs). Afterwards, the working principles of organic optoelectronic devices, such as organic light emitting diodes (OLEDs) and organic light emitting transistors (OLETs), are covered. Finally, chapter 1 is completed with the description of the photochromic dopant used in this work, the diarylethene derivatives, their unique properties and their recent use in LRDs with particular emphasis on OTFT and OLEDs.

Chapter 2 gives a description of the basic techniques used to study the emitting systems touched in this thesis. For the characterization of the optical properties of our organic blends the attention is focused on PLQY measurement, via the use of the integrating sphere, and the fluorescence decay lifetime via the time-correlated single photon counting

equipment. The final part of this chapter hosts a more technical description of the fabrication ad characterization methods of OLEDs and OLETs devices.

Chapter 3 describes the work done to understand better the interaction between DAEs and organic semiconductor in OLEDs. The effect of the molecules isomerization on the device performance is tested for different dopant concentrations. In addition, its influence on the different charge carriers is demonstrated, for the first time, via the characterization of single-carriers optically switchable devices. The final part of this chapter is focused on the attempt to fabricate optically switchable micro-OLEDs.

In chapter 4 the pursuit of a micro-sized, optically switchable, emitting device is achieved via the fabrication and characterization of OLETs having a channel length of 2.5 μm. In particular, we realized and characterized optically switchable OLETs emitting in the whole visible spectrum. The light-responsivity of such devices allowed us to generate arbitrary micro-patterns on the device emissive channel via irradiation with focused light.

Chapter 5 investigates the design, fabrication and characterization of electroluminescent devices exploiting the innovative and promising class of fluorescent compounds of graphene quantum dots (GQDs). Such atomically defined GQDs, synthesized via a bottom-up approach, allows high PLQY and narrow emission. Importantly, they are air stable and heavy-metal-free. Device reported in this work are among the best performing red-emitting LEDs based on this class of materials.

Chapter 6 includes a summary on the achievements obtained in this work and an outlook on potential future work.

2 Materials Properties and Devices

2.1 Organic semiconductors

Organic semiconductors are a specific class of oligomers and polymers whose carbon backbone is the alternation of single and double bonds. This peculiar structure, also known as conjugated chain, allows the electrons distribution to be delocalized on the entire molecule, thus inferring to this plastic materials unexpected electrical and optical properties similar to those observed for inorganic semiconductors. The first discovery of the electrical conduction in doped polyacitylene was published by Shirakawa, MacDiarmid and Heeger (Nobel laureate in 2000) in 1977 [14]. Differently, the photoluminescence of organic conjucated systems was reported in 1963 by Pope at al. and in 1990 by Burroughes et al. for single-crystals anthracene and poly(p-phenylene vinylene) respectively [15], [16]. Conjugated polymers attracted immediately the interest of the scientific community as they were considered to be the ideal candidates for the fabrication of flexible, low-cost and robust electrical and optoelectronic devices. Another huge advantage of such polymeric materials is that their optical and electrical properties can be finely tuned during the synthetic process [2]. The same result with inorganic semiconductors requires a radically different and more expensive approach, which involves high vacuum epitaxial crystals growth and controlled ionic bombardment [17]. Aware of such a game-changing potentialities huge efforts were spent by academic and industrial research groups on the designing, fabrication and optimization of organic optoelectronic devices such as OLEDs, OLETs, photovoltaic cells (OPV) and OTFT [16], [18]–[22]. Most of this technologies have seen a continuous improvement in the last 20 year and are now close to the up-scaling process. A different, much more rewarding, evolution was observed for OLED technology. Indeed, not only it has already reached the

mass-production and the commercialization, but it has had a disruptive impact on the market. Today, it is the leading technology for display applications and it has already widely replaced liquid crystal displays in the high-hand mobile display sector. Such result was possible also thanks to the increasing interconnection of disciplines such as solid state physics, chemistry and device engineering which together led the a deeper understanding of the materials properties, of the processes that govern the device operation such as charge transport, energy transfer mechanism and light generation [23]–[26].

2.1.1 Electronic properties

2.1.1.1 π-conjugated properties

The electrical conductivity of organic semiconductors find its roots in electronic properties of the carbon atoms in a π-conjugated system.

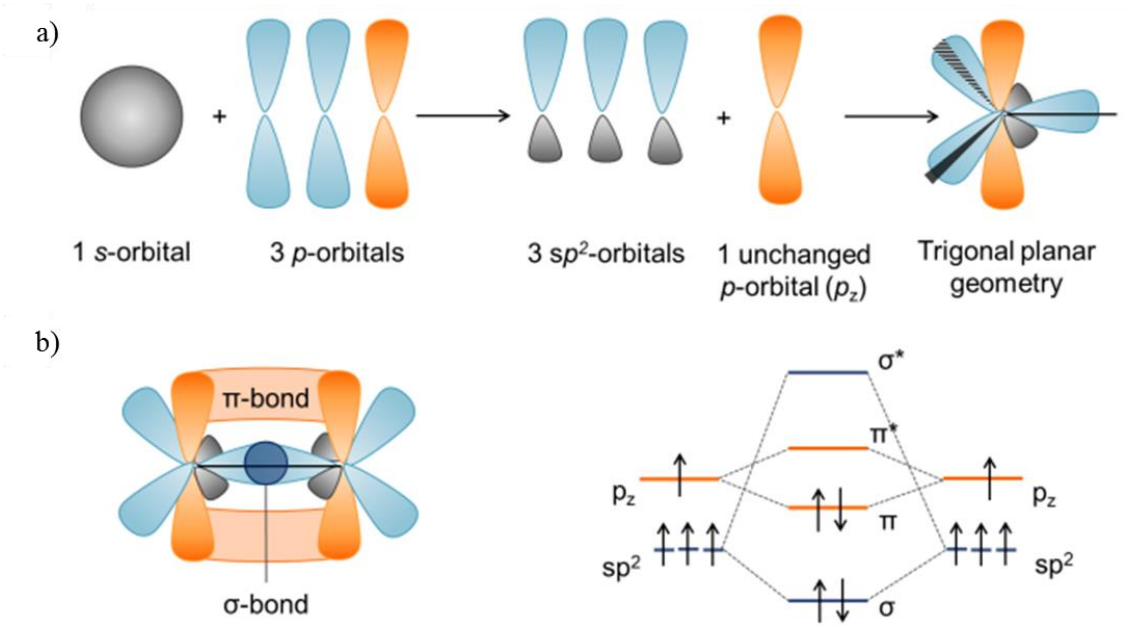

Figure 1: a) formation of sp^2-hybrid orbitals in a carbon atom. Two 2p-orbitals and the 2s-orbital generated 3 co-planar hybrid-sp^2 orbitals, the atomic orbital $2p_z$ remains normal to the plane. b) σ- and π- bonds formation in carbon-carbon double bond and the related energy diagram showing the formation of bonding and anti-bonding molecular orbitals. Reproduced from [27].

The formation of a double bond between two carbon atoms (ethene) is explained via the molecular orbital hybridization theory, see Figure 1. Here two bilobate p-orbitals (p_x, p_y) are "mixed" with the symmetric s-orbital to give three coplanar, equally spaced, sp^2 orbitals which generate σ-bonds, see Figure 1b. The remaining p_z orbitals, oriented normally to the plane, are overlapped only partially and allow the formation of a weaker π-bond. The stronger double bond shrinks the C-C interatomic distance (~ 1.33 Å) and locks the rotational motion of the each carbon atom around the σ-bond in a quasi-planar structure. In the molecule energetic configuration, each of the new bond formed is split in two new energy levels: bonding and antibonding (the latter is starred). Electrons will favourably occupy the bonding orbitals having lower energy than the original atomic ones, leaving the anti-bonding levels totally empty as shown in Figure 1b.

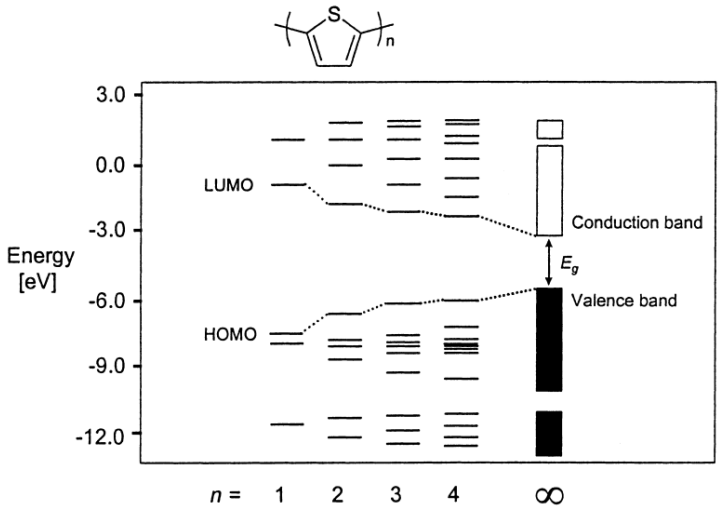

Figure 2: From discrete molecular orbitals to energy bands. Calculated energy levels for oligothiophenes (n from 1 to 4) and for polythiophene. Reproduced from [28].

In a conjugated polymer, the electrons in the π-system result delocalized over the carbon backbone allowing the material conductivity. The increasing number of double bonds generates manifold of energy levels which ultimately can be seen as energy bands. In particular, the electronic configuration of the carbon atoms, with sp^2 hybridization,

generates a fully occupied band and a completely empty one, whose frontier levels are described as HOMO (highest occupied molecular orbital) and LUMO (lowest unoccupied molecular orbital) levels, respectively. Figure 2 shows the result of the calculation of the energetic configuration for thiophene oligomers having an increasing number of repetitive units. Here, starting from a discrete atomic energy levels a semiconductor-like band structure is gradually achieved moving towards the polymer [28]. The work form Van Mullekom et al. highlights well that the energy gap (E_g) is reducing increasing the oligomer length, as consequence of the growing conjugation length. Indeed, in organic semiconductors the E_g is finely tailored acting both on chemistry of the compound and on its interaction with the surrounding molecules, as described in Figure 3.

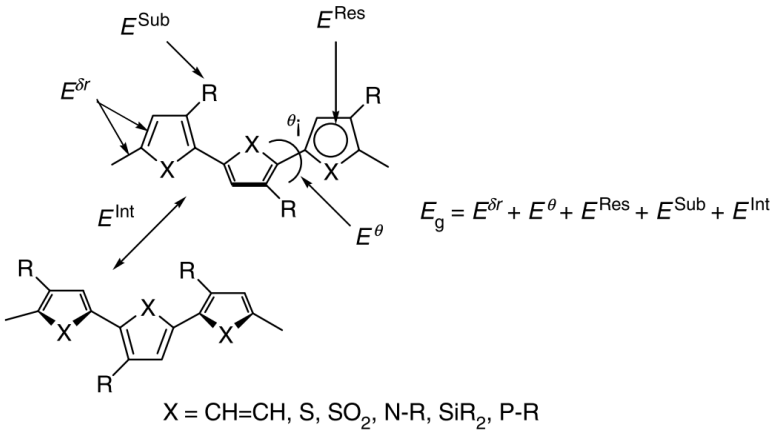

Figure 3: Synthetic approach for bandgap engineering. Factors affecting the E_g of organic semiconductors: $E^{\delta r}$, type of carbon backbone; E^{res}, resonance and conjugation length; E^{sub}, electronic effect of sobstituents; E^{θ}, steric effect of substituents; E^{int}, interaction with others molecules. Reproduced from [2].

The main factors influencing the E_g are the organic backbone type ($E^{\delta r}$) and the number of resonance chemical structures allowed (E^{res}), they define the maximum potential extension of the conjugated system. The delocalized electrons distribution can be altered via substituents groups which can have a dual effect, electronic (E^{sub}) and steric (E^{θ}). The

former refers to the electron-withdrawing or electron-donating (inductive or mesomeric) effects which modulate the HOMO and LUMO energy levels position, thus the E_g. Bulky substituents will introduce a steric obstacle to the planarity of the conjugated system, they will induce a twisting angle to the carbon backbone which will ultimately reduce the actual length of the conjugated system, thus blue-shifting the E_g. Finally, also the interaction of the organic semiconductors with the external environment (E^{int}) might introduce variation on the material band gap. The actual conjugated segment of an organic semiconductor is referred often as chromophore, therefore, a conjugated polymer can be described as a sequence of chromophores.

2.1.1.2 Electronic excited states and charge transport

Organic semiconductors are characterized by a lower dielectric constant and a much lower degree of crystallinity compared to their inorganic counterparts. As results, the charged excited states can be stabilized by chain distortions which lowers the overall energy of the charged configuration. Furthermore, the low dielectric constant provokes a low shielding of the charges within the material, which result in stronger coulombic interaction between charges states. Thus excited states in organic semiconductor have a strong interaction with the surrounding environment and therefore are referred to as quasi-particles, they play a major role in both charge transport and light generation in conjugated systems. When a charged excited state is formed, due to a redox process, charge injection or photo induced charge transfer, such quasi-particle (hole or electron) will be coupled with a local organic backbone distortion, this combination is defined a polaron, see Figure 4. Being charged, polarons will move through the conjugated systems and between different chains under the effect of an electric field. Further oxidation on the same chain will generate a bipolaron which is a dication or dianion. Given the larger chain

distortion generated, thus a larger energetic gain, in case of repeated oxidation the formation of a bipolaron is favoured compared the formation of two polarons [2]. From the energetic point of view, both polaron and bipolaron will form extra energy levels within the material energy gap. While polarons have spin momentum, bipolarons are spinless.

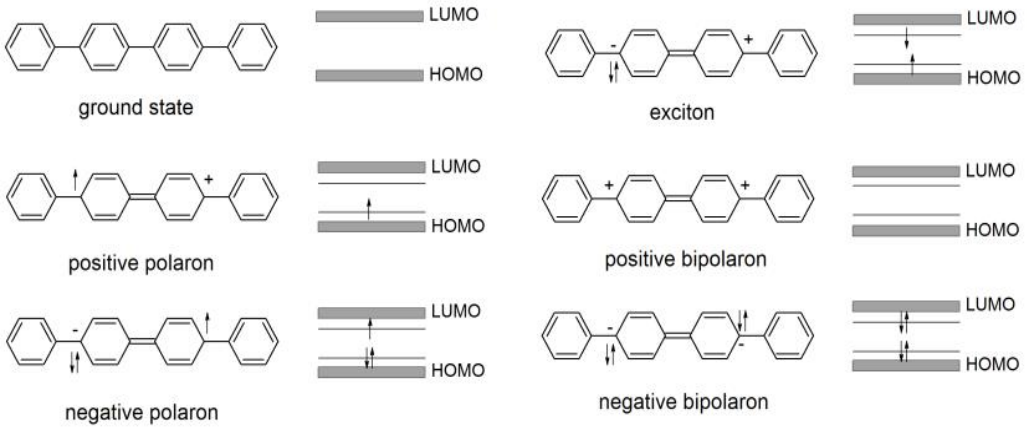

Figure 4: Structural and electronic variations of poly(p-pheyilene vinylene) induced by localized charges. Intra-gap energy levels are generated and the conjugated system is distorted to a quinoid-like geometry. Reproduced from [27]*, originally revised from* [29], [30].

A neutral quasi-particle which has a fundamental role in the light generation process in organic materials is the exciton, it consists in the coupling between a positive and negative charge via coulombic interaction. Because of the low dielectric constant (2-4) of organic materials, excitons formed in such materials have larger binding energy (0.1-1 eV) than those formed in inorganic semiconductors (~ 0.025 eV). The former are known as Frenkel excitons, the latter as Wannier-Mott exciton. Excitons can be formed via the interaction between positive and negative polarons, or via the promotion, due to the absorption of a photon, of an electron to an excited state. Depending on the total spin *S*, we can have singlet (*S*=0) or triplet excitons (*S*=1). While the photo-excitation mainly generates singlet excitons, electrical excitation, which can generate positive or negative polarons, leads to

the formation of triplet and singlet excitons in a ratio 3:1 [31]. Once generated, excitons can undergo radiative (i.e. photoluminescence) or non-radiative (i.e. charge separation) recombination, the ratio between these two decay paths is strongly dependent on inter- and intra- molecular interactions.

Charge transport in organic semiconductor is still under debate, band-like transport has been reported for both highly ordered planar molecular systems or in case of highly doped conjugated polymers [23], [32]–[35]. In the first case, the coupling of electron wavefunctions among different conjugated molecules allows their delocalization over the thin film. Differently, has been demonstrate that when polypyrrole is heavily doped a large concentration of bipolarons is achieved which generates empty energy bands available for the carriers conduction [2].

Beside these specific conditions, in presence of localized states, charge transport occurs via hopping mechanism between these states and upon thermal activation. Typical mobility values, at room temperature range from 10^{-6} up to 10^{-3} $cm^2\,V^{-1}\,s^{-1}$ for disordered polymers and up to 0.1 – 1 $cm^2\,V^{-1}\,s^{-1}$ for more ordered structures.

2.1.2 Optical properties

2.1.2.1 Jablonski diagram

As mentioned in the previous paragraph, once an exciton in formed it can undergo either radiative or non radiative recombination. The decay paths of optically generated excitons are visually summarized in the Jablonsky diagram see Figure 5. Here, each electronic molecular state, singlet (S_{xy}, where 'x' is the electronic state and 'y' the vibrational state) and triplet (T_{xy}) state, is represented as a manifold of vibrational states. When a photon with energy $h\nu \geq S_{10}\text{-}S_{00}$ is absorbed, one electron is promoted to a singlet excited state. Indeed, because of the selection rules in the electric dipole approximation, the spin

multiplicity must be retained after the electronic transition. The electron promoted to higher excited molecular and vibrational states will rapidly (~ 10^{-15} s) thermalized to the ground vibrational level of the first excited singlet state S_1. Here, the molecule can go through a radiative relaxation path, which leads to the release of photon having energy equal to optical transition to S_0 electronic level. Such process referred to as fluorescence has a typical decay time in the range of few nanoseconds (10^{-9} s).

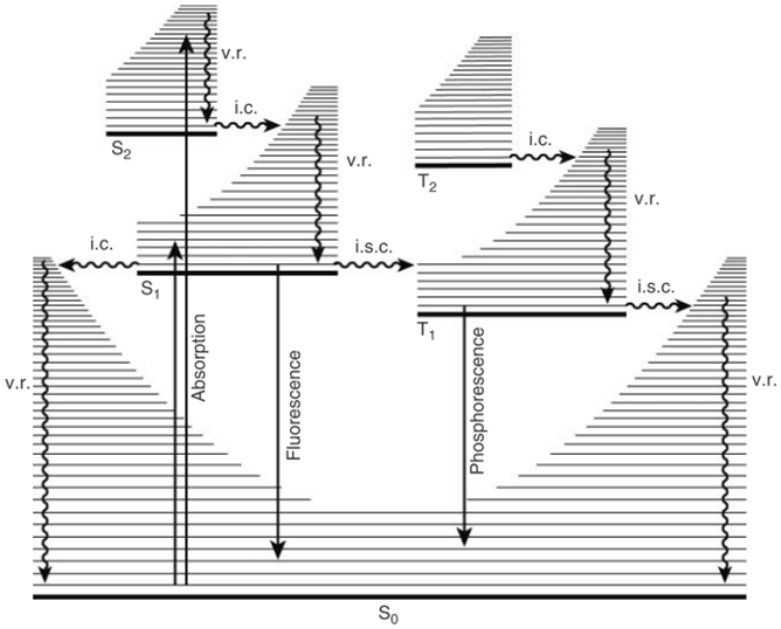

Figure 5: Jabonsky diagram to describe the possible optical excitation paths in organic compounds. Radiative transitions (both absorption and emission) are indicated by straight arrows, non-radiative ones are indicated by wavy arrows. Reproduced from [36].

Differently, the non-radiative de-excitation path can involve vibrational relaxation or the transfer of the excitation to a neighbouring molecule. Additionally, from S_1 the electron can also populate the triplet state T_1 via intersystem crossing. For fluorescent materials the radiative transition T_1-S_0 is forbidden in the electrical dipole approximation. Importantly, in presence of heavy metal (i.e. Ir-based organometallic complexes), the radiative transition from a triplet to a singlet state has a non-zero probability. In this case

the luminescence generated is named phosphorescence and it is characterized by a decay time in the range of the milliseconds. Thus, the effectiveness of the radiative transitions depend on both the molecular structure and the molecular species surrounding the excited molecule. The electronic distribution of the vibrational states plays a major role in the intensity of a given electronic transition. Indeed, in the semi-classical interpretation of the electronic transition the Franck-Condon principle considers the electronic transitions (10^{-15} – 10^{-16} sec) as instantaneous compared to the nuclei motions (10^{-13}-10^{-14} sec). Thus, the electronic distribution over the vibrational levels can be seen as frozen during the electrons excitation. As result, the intensity of an electronic transition is proportional to the square of the overlap integral between the vibrational wavefunctions of the two states involved in the transition.

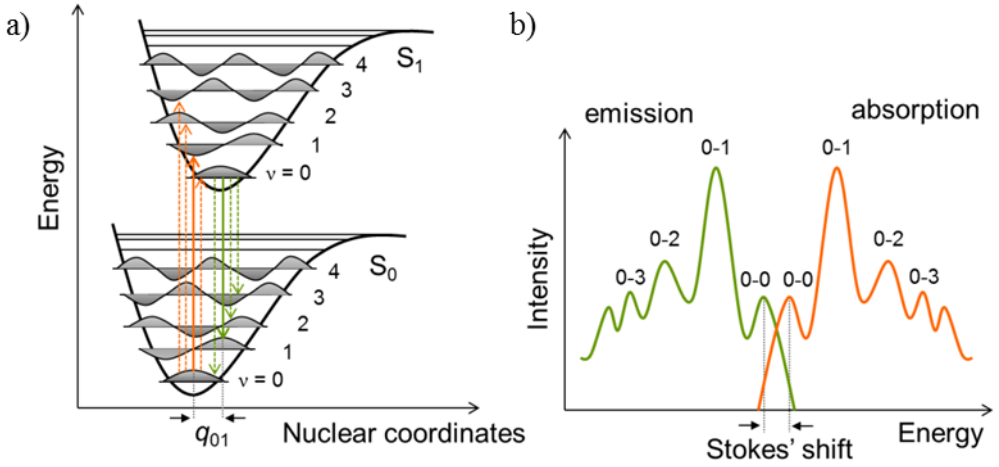

Figure 6: a) Morse-like potential for a molecule in its ground (S_0) and excited (S_1) electronic states. For the Franck-Condon principle the most probable transition involves the levels $S_{00} \rightarrow S_{11}$. b) If the molecule in the excited state maintain the same potentials geometry and nuclear coordinates, its fluorescence will resemble the mirror image of the absorption spectrum. Reproduced form [27].

If the nuclear displacement between ground and excited state is unchanged after the transition, the absorption and emission spectrum result as mirror images of one another.

The energy difference between the 0-0 transition in absorption and emission spectra is named Stokes'shift, which represents the energy lost in the thermalization process. Conjugated polymers, which can be seen as chain of chromophores having slightly different conjugation lengths are characterized by a relatively large (> 50 nm) Stokes' shift. Indeed, the excitation photo-generated in the shorter conjugated segments (having a larger E_g) will undergo energy transfer towards longer conjugated chromophores which will eventually relax with emission of a photon having considerably lower energy than the exciting one. The photoluminescence quantum yield (η_{PL}, or PLQY), defined as the ratio between emitted and absorbed photons, indicates the ability, for a given material, to decay efficiently through a radiative path. Rigid conjugated systems, having fewer vibrational degrees of freedom, show generally higher values of PLQY [37].

2.1.2.2 Energy and electron transfer

As mentioned in section 2.1.1.2, the excitation generated on a chromophore can be transferred, via non-radiative process, to other conjugated acceptors. The most relevant electron energy transfer (EET) mechanisms are the Föster resonance energy transfer (FRET) and the Dexter energy transfer. The former is due to the resonant dipole-dipole interaction between the dipole transition moments of the donor excited state, μ_1, and the acceptor one, $\mu 2$, see Figure 7. Here, the energy released during the non-radiative relaxation of the donor state excites the acceptor system. Differently, the Dexter EET is a donor-acceptor electron transfer. Here, simultaneously, one electrons passes from the ground state of the acceptor to the ground state of the donor state, while another electron is transferred, in the opposite direction, between the donor-acceptor excited states. While the rate of both processes is proportional to the spectral overlap integral, between the

fluorescence of the donor compound and the absorption of acceptor system, they scale differently with the donor-acceptor distance.

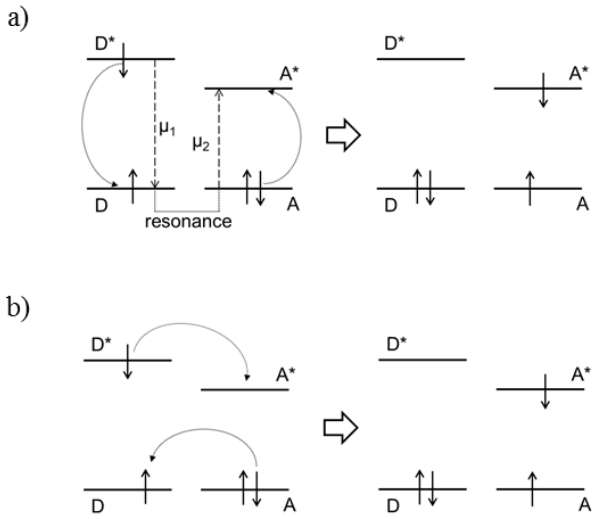

Figure 7: Schematic representation of the Foster (a) and the Dexter (b) energy transfer mechanisms. Reproduced from [27]*, originally adapted from* [38].

As a coulombic interaction, FRET allows interactions over a larger range (1 - 10 nm), indeed the rate of energy transfer is inversely proportional to the sixth power of the donor-acceptor distance. Dexter electron transfer requires the overlap between the donor and acceptor electronic orbitals, thus its probability shows an exponential dependence to the donor-acceptor distance, which makes this interaction effective within the shorter range of 1 – 4 nm. Another important difference is the spin multiplicity of the state involved in the EETs. While FRET, being a dipole-dipole interaction is allowed only between singlet donor-acceptor states, Dexter electron transfer can involve also triplet states.

2.1.2.3 Intra- and inter-molecular interactions

Conjugated units in a polymer can lead to interchain interaction. These multi-body interaction, which can involve two or more conjugated systems, are favoured by specific types of chromophores, having, in example, rod- or disk-like, or C- or handlebar- shaped

segments [39]. If the interaction involves molecules in their ground states, the resulting systems are defined as aggregates. Differently, if one or the interacting species is in its excited state, the bimolecular species can be defined as excimers (a contraction of 'excited dimers'), when only identical chromophores are involved, or exciplexes, if the coupling takes place between different conjugates systems. Excimers and exciplexes have a partial charge transfer character, their formation is confirmed by the distinctive, red-shifted, featureless emission band. Its spectral position will define the spectral shift, energy difference from the monomer emission peak, which is the energy gained by the system via the interchain interaction.

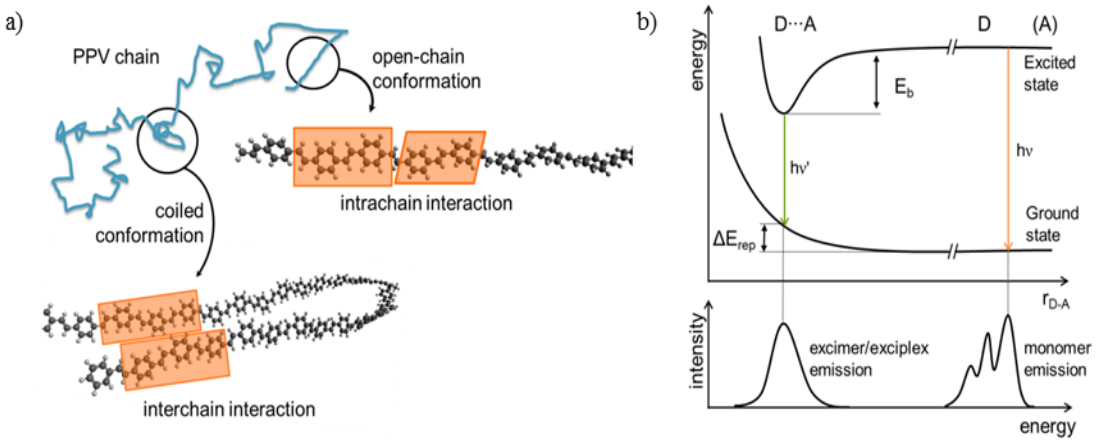

Figure 8: a) Conformational disorder in a poly(p-phenylene vinylene) polymer chain. Organge Boxes indicate the chromophore subunit. b) Potential energy diagram describing the emission from an excimer (if D=A) or exciplex versus the monomer. Reproduced from[27]*, originally revised from* [39]–[42].

2.2 Graphene quantum dots as emissive material

Graphene-based emitting materials are attracting the attention of a continuously growing portion of the scientific community. Initially, the enthusiasm for graphene's high carrier mobility was mitigated by the observation of poor optical properties due to the absence

of an optical band gap [43]. To overcome this limitation, a range of approaches have been investigated to elicit semiconducting properties from graphene-related materials [44]–[48]

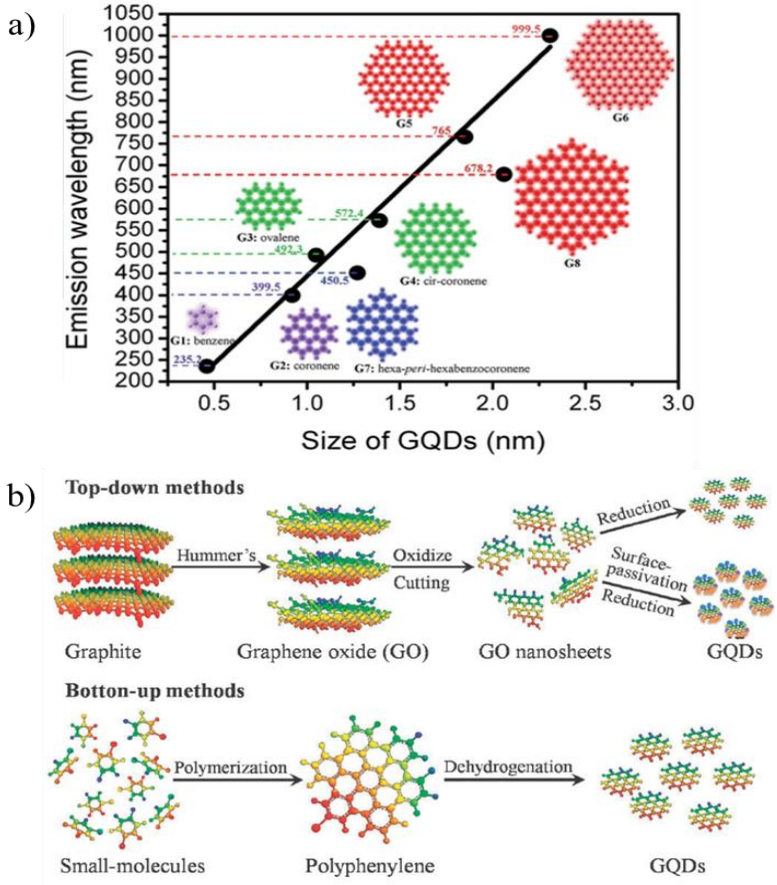

Figure 9: Graphene quantum dots. a) tuning of the optical properties for different GQDs sizes; b) Schematic of top-down and bottom-up (hydrothermal) synthesis [49], [50].

. Among them, structural confinement of graphene sheets into nanoscale graphene fragments (< 20 nm), which can be regarded as graphene quantum dots (GQDs), has appeared to be the most successful [51]–[53]. Results achieved in this direction make light-emitting GQDs a biocompatible and environmentally friendly alternative to Cd2+/ Pb2+ based colloidal semiconductor quantum dots (QDs) [54]–[56]. Importantly, GQDs are conjugated systems and the emission wavelength can be finely tuned in the visible range via controlling the GQDs dimension (see Figure 9a). In terms of synthesis, GQDs are mainly prepared via top-down (exfoliating a graphite crystal) or hydrothermal

treatment of small-molecule precursors, as shown in Figure 9b [57], [58], [46], [50], [53], [59]. A shared challenge for such synthetic routes is the control on the GQDs optical and electric properties. Indeed, the reaction product generally shows a large size distribution, defects inside the aromatic core and undefined edge structures, which are typically passivated not only with hydrogen but also with different oxygen-containing functional groups such as hydroxyl, carboxylic acid and carbonyl, leading to poor and/or excitation dependent photoluminescence[60]–[65]. Furthermore, these electron-withdrawing groups act as trap states for electrons when these materials are embedded in light-emitting devices, further lowering the overall device performances [66]–[69]. The broad or current dependent emission of carbon based dots has often led to white-emitting or "colour switchable" optoelectronic devices [70]–[74]. Improved synthetic techniques allowed GQD showing excitation independent fluorescence suitable for LEDs emitting in the visible spectrum [71], [75]–[77]. Among them, red-emitting devices were the least performing one as the undefined and defective GQDs edge structure was particularly detrimental for the larger dots [75], [77]. In contrast, bottom-up molecular synthesis provides access to structurally defined graphene quantum dots, based on the expertise of the modern synthetic organic chemistry. GQDs can thus be synthesized with designed shaped, edge structures, and edge substitution, allowing for the tuning of diverse parameters such as optical and electronic properties and self-assembly behaviour. However, LED based on such a bottom-up GQDs have seldom been reported and examples of GQDs with strong red emission have remained scarce [78], [79].

2.3 Organic light-emitting diodes (OLEDs)

2.3.1 Device structure

The simplest OLED device is formed by an organic electroluminescent semiconductor (~ 100 nm) sandwiched between a transparent anode and a highly reflective cathode. In highly efficient OLEDs the charge carriers injection and accumulation in the emissive layer, are favoured and balanced by a number of additional layers, which, depending on their properties, are referred as hole and electron injection, transport and blocking layers (HIL, HTL, HBL, EIL, ETL, EBL). For this reason high performance commercial OLEDs have a device stack having at least five organic functional layers. For the study of new materials or/and new device working principles, simpler stack architectures are preferred and viable. For this reason, in our experiment, we typically adopt a two-layer architecture (as shown in Figure 10), where the hole injection is improved by a ~ 40 nm thick layer of poly(3,4-ehtylenedioxythiophene)-poly(styrenesulfonate) (PEDOT:PSS) at the anode interface. The latter is usually indium-tin-oxide (ITO, ~150 nm), a highly transparent oxide (up to 90% at 550 nm), having a sheet resistance ranging between 7 to 20 Ω/sq, depending on the deposition conditions, and high work function of ~ 4.7 eV.

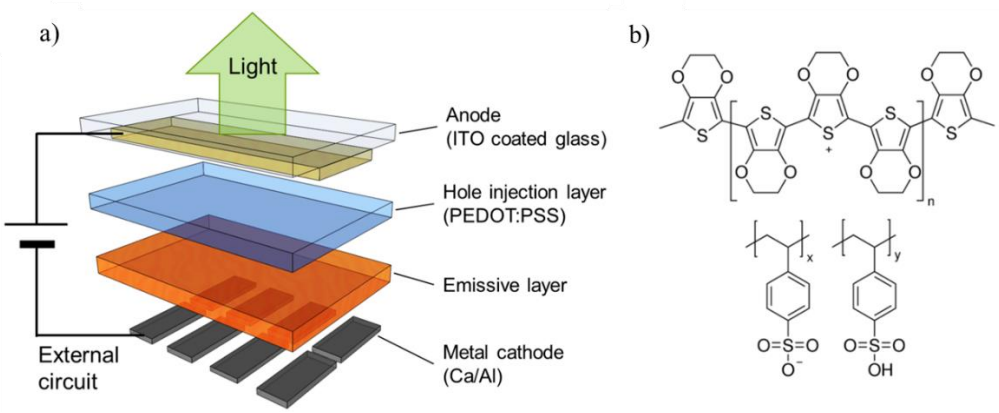

Figure 10: a) Basic OLED architecture used in this thesis. b) Chemical structure of PEDOT:PSS. Reproduced from [27].

Materials selected as cathodes must have low work function to inject efficiently electrons in the emissive material. Calcium (Ca) is a common choice (~ 30 nm) as its ~ 2.8 eV work function well serves this purpose. The stack is completed with ~ 150 nm of aluminium (Al), which acts as highly reflective capping layer to prevent detrimental Ca oxidation process.

2.3.2 Device operation

The application of a sufficiently large electric potential to an OLED induces the injection and transport of charge carriers within the device. Under the effect of the electric field, positive and negative polarons (see section 2.1.1.2) migrate throughout the device in opposite directions. The device stack is optimized to maximize the polarons concentration in the emissive layer, increasing, locally, the probability of exciton formation and thus photons emission. Such light emission is referred to as electroluminescence.

Figure 11a shows the energy level diagram of the materials involved in the simplest OLED architecture (ITO/EML/Metal cathode) before the contact between the layers takes place. Given an organic emissive material, characterized by its charge transport and optical properties, the selection of electrodes materials play a crucial role in the device performance determination. Indeed, their work functions (Φ_{ITO} and Φ_{metal}) must minimize the charge injection barriers (Φ_h and Φ_e) at the metal/semiconductor interface. Follows that hardly electrons and holes can be injected from the anode and cathode, respectively. Given the asymmetric electrodes (metals having different work functions), when functional layers are brought into contact a charges migration takes place within the device to equilibrate the Fermi level (E_f) throughout the device layers, until a sufficient, equal to the difference between the electrodes work functions, built-in voltage is generated (V_{BI}).

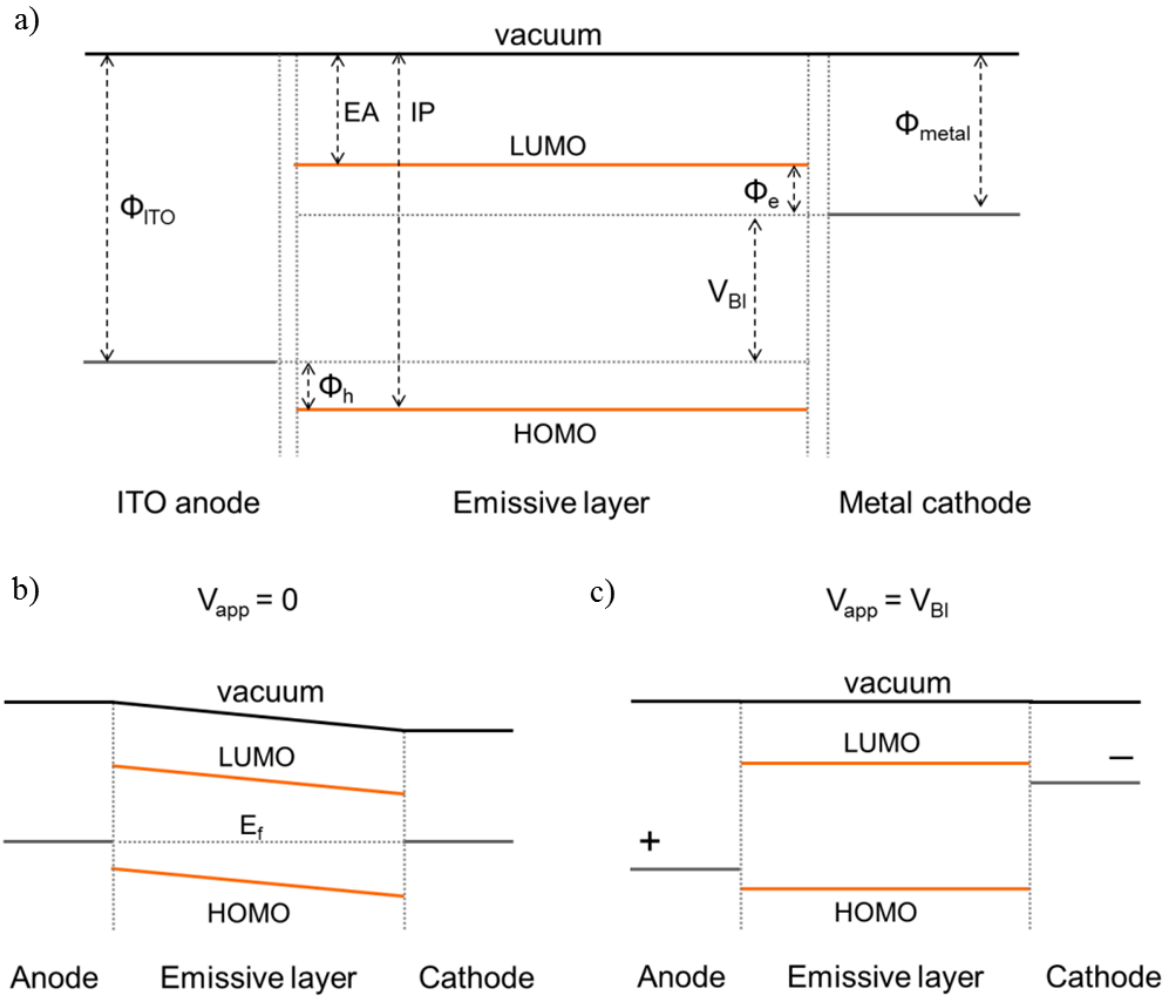

Figure 11: Energy levels, referred to the vacuum level, of the materials involved in an OLED device. a) as isolated materials, b) after the contact between the materials and the Fermi levels (E_f) alignment, c) at the flat-band condition ($V_{app}=V_{BI}$). Reproduced from [27], *originally adapted from* [80].

In the absence of an external applied field (V_{app}) the V_{BI} can be estimated by knowing the semiconductor E_g and the electrodes work function using the following equation:

$$E_g = eV_{BI} + \Phi_e + \Phi_h$$

The band diagram of our device can be described with rigid band model as the depletion layer in organic polymer extends for distances larger than the actual thin film thickness

(~ 100 nm), thus band bending is negligible. In the absence of an external applied voltage, bands are rigidly tilted because of the presence of the built-in voltage.

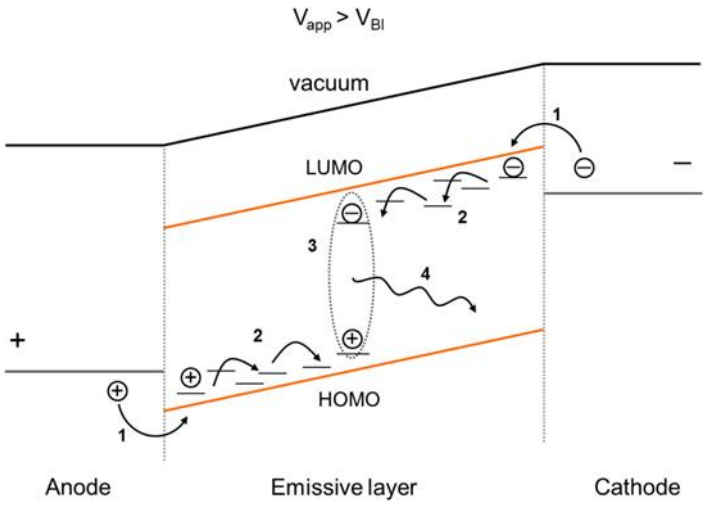

Figure 12: OLED device operation in forward bias: 1) charge carriers injection, 2) charge transport through the organic semiconductor, 3) charge coupling and exciton formation, 4) exciton radiative recombination and photon emission. Reproduced from [27]

When a forward bias is applied, the bands slope is decreased until V_{app} equals V_{BI}, defined as flat-band condition, which is the minimum bias required for charge injection. In Figure 12 is shown the basic operation of an OLED for $V_{app} > V_{BI}$, the photon generation is achieved through 4 steps: charge injection, charge transport, exciton formation and exciton radiative recombination. In case of low injection barriers at the semiconductor/metals interfaces, the injection can be described with the Richardson-Schottky model, where charges with sufficient thermal energy can overcome the barrier and be injected in the polymer. Differently, in case of higher energy barriers, the current flowing through the device is injection limited and the Fowler-Nordheim model describes better this scenario. Here the injection take place via a field-induced tunnelling across a triangular potential barrier.

In conjugated polymers, charges are transported under the effect of the applied electric

field and of the concentration gradient (diffusion current) via hopping, a thermally assisted tunnelling of carriers between localized sites, see section 2.1.1.2. In case of low injection barrier, the hole-current flowing through the device will be described by the space charge limited current (SCLC) model. Here, because of the limited hole mobility, at high voltages, positive carriers accumulates in proximity of the anode and hinder the injection of further carriers. Differently, electrons current is generally trap limited, as electron transport in strongly affected be trap states resulting from, in example, defect states and impurities [34], [81]–[85]. Generally the electron injection is less effective which results in a charges concentration imbalance within the device. Holes and electrons can form excitons via a recombination process which is often described as a bimolecular Langevin process. Here the recombination rate is limited by the diffusion, in opposite direction, of holes and electrons through the devices [86]. For high performance devices, the exciton generation rate is maximized by finely tuning the layers thickness and combining charge transport and blocking layers to achieve both a balanced charges concentration within the device and a recombination zone within the emissive layer. Indeed, when two or more organic semiconductors are placed in contact a band heterojunction is formed due the difference between their energy gaps and HOMO-LUMO levels energies.

Once holes and electrons form the excitons, the quasi-particles can decay via a radiative or a non-radiative relaxation path. In organic semiconductors, charges are injected statistically with respect to their electron spin, therefore, the recombination of holes and electrons is expected to generate singlet and triplet excitons in a ratio 1:3 under electrical operation [31]. For fluorescent emitters the radiative decay of triplet excitons (75%) is spin forbidden, only the single excitons can contribute to the photons generation. Different is the situation in case of phosphorescent emitters, where, the radiative

relaxation of triplet excitons is a partially allowed transition. Here, thanks to an efficient inter system crossing (ISC), often induced by the presence of heavy-metal atoms, the excitation can be transferred from singlet to triplet state thus all the excitons generated can undergo radiative decay.

Given the complexity of the process involved in the electroluminescence generation, the external quantum efficiency of a LED, the ratio of photons collected outside the device over the charges injected, can be written as follow:

$$EQE = \eta_{PL} \cdot r_{st} \cdot \gamma \cdot \eta_{out}$$

Where η_{PL} is the photoluminescence quantum efficiency of the emitting material, r_{st} is the expected ratio between singlets and total number of excitons, γ is the charge balance factor and η_{out} is the light out-coupling efficiency. For technological application it is fundamental to achieve devices having large EQE. Indeed, a more efficient device will output a certain luminous intensity with at a lower current density, this has direct implication on crucial aspects such as device lifetime and power consumption.

2.4 Organic light-emitting transistors (OLETs)

2.4.1 Device structure

An organic light-emitting transistor is a three terminal device where an electroluminescent organic semiconductor is the active material. In the simplest configuration the device is an emitting bottom-gate bottom-contact OTFT. A 230 ± 10 nm of gate insulant, SiO_2, is thermally grown on highly doped ($n = 3 \times 10^{17}$ cm^{-3}) n-type silicon layer which acts as gate contact. Source and drain contacts, a double layer of ITO (10 nm) and gold (30 nm), are deposited on the insulator and patterned via lift-off

lithography. The substrates for this device architecture are commercially available, and this circumstance makes them particularly suitable for testing electrical performance of organic materials. The trap states formed on the insulator surface, mainly due to hydroxyl groups and dangling bonds, are typically passivated via the formation of a self-assembled monolayer of hexamethyldisiloxane (HMDS) or octadecyl-trichlorosilane (OTS) [87]–[89]. A thin film of organic electroluminescent semiconductor is deposited via spin-coating to complete the device stack. Because of the symmetric, with high work function, ITO/Au contacts this architecture favours the injection and thus transport through the organic semiconductor mainly of positive charge carriers. Indeed, in case of electroluminescent polymer, the light generation it is limited to region surrounding the drain electrode as the minority carriers are not effectively injected, thus the excitons generation and radiative decay can only take place in the proximity of the contacts [87]–[89]. The simplicity of this architecture, which allows to test and investigate systematically the electrical properties of organic semiconductors, is not suited to achieve the highest optoelectronic performance due to the vast charge injection imbalance resulting by the symmetric electrode. Improved performances can be achieved by using a low work function metal, such as calcium, as drain contact or by adding charge transport layers in a stacked bottom-gate top-contacts architecture. In this case both holes and electrons will be efficiently injected, favouring the exciton formation and light generation [90]–[94]. Considering that my research activity is focused on the understanding of the interactions between photochromic compounds and organic semiconductors, and not primarily on the improvement of the device performance, the simpler and commercially available architecture, based on symmetric contact, was chosen as investigation platform.

2.4.2 Device operation

The electrical operation of an OLET is analogous to an OTFT, which is a specific type of field effect transistor (FET). A FET is basically a capacitor in which one of the two shields is formed by a conductive channel and two ohmic contacts named source and drain electrodes. The charge density in the channel is modulated via the bias applied to the gate electrode, which can be seen as the other shield of the capacitor. Even if the FET working principle was proposed in 1930 by Lilienfeld, only in 1960 the silicon-based metal-oxide-semiconductor (MOSFET) was fabricated [17]. A MOSFET structure is shown in Figure 13.

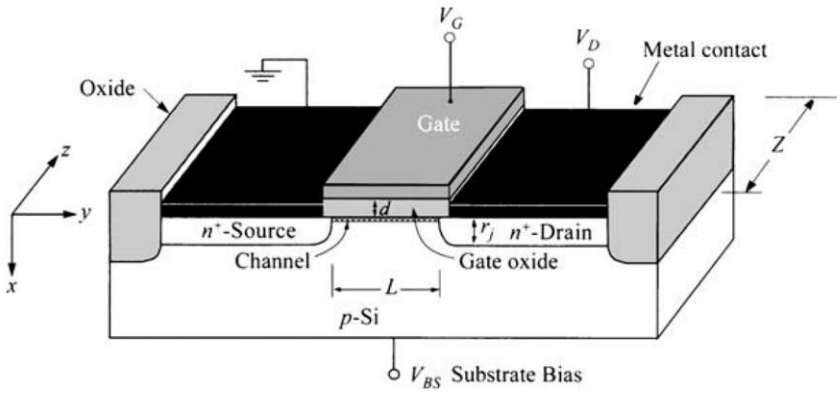

Figure 13: Schematic of a MOSFET device. Reproduced from [17].

Two n^+ areas are generated, via ion implantation, on a p-type silicon substrate. Above these regions, source and drain contacts are deposited and defined via a photolithographic procedure. The gate electrode, isolated from the semiconductor, is deposited on the SiO_2 dielectric layer. Drain and gate electrodes are normally polarized against the source electrode which is normally grounded. In absence of an applied bias, the source-drain circuit is equivalent to two p-n junctions inversely polarized, thus only the saturation current can flow through the device. The transistor is in the OFF state. Appling a potential to the gate electrode, a pool of charge carriers can be generated at the semiconductor-

insulator interface leading to the increase of the source-drain current (I_{DS}), the device is in the ON state. The working principle of a MOSFET can be better understood studying a simpler device first, the diode metal-insulant-semiconductor (MIS). As shown in Figure 14, such device is constituted by an insulant layer sandwiched between a grounded semiconductor and a metal contact.

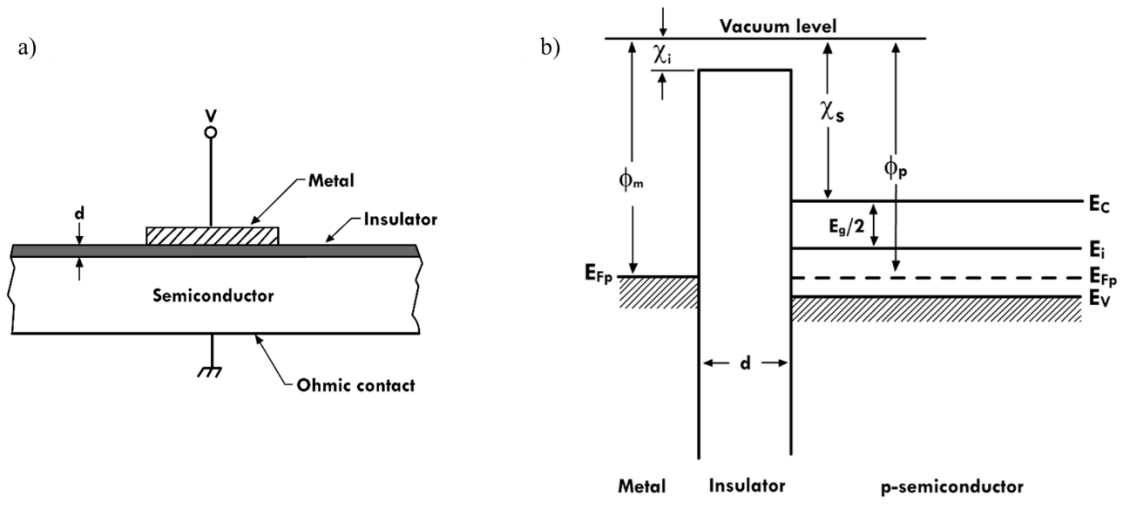

Figure 14: a) Schematic of a diode metal-insulator-semiconductor (MIS), energy levels alignment in a diode MIS. Adapted from [17].

The energy bands diagram of an ideal MIS diode, for a p-type semiconductor, in absence of polarization is shown in Figure 14. A diode MIS is termed ideal because the bands are flat for zero applied voltage, this is fulfilled when $\phi_m - (\chi_s + E_g/2q + \psi_b) = 0$ [22]. Here, ϕ_m is the metal work function, E_g the semiconductor bandgap, q the absolute electron charge, and ψ_b the potential difference between the Fermi level and the intrinsic Fermi level E_i (which is located very close to the midgap). Indeed, in the non-ideal case, a small band curvature exists at the insulator-semiconductor interface and a small potential, called flat-band voltage, must be applied to the metal to get the flat-band condition. When MIS diode is polarized, via a positive or negative bias, three possible scenarios can be induced at the insulant-semiconductor interface. For a negative bias (Figure 15a), the bands bend

up-ward and the top of the valence band moves near to the Fermi level leading to the accumulation of holes at the interface. Differently, the depletion of majority carries occurs in case of moderate positive voltage (Figure 15b). When a large positive voltage is applied to the metal, the bands further bend downward and the intrinsic level eventually crosses the intrinsic Fermi level. In this situation, at the interface, the density of electrons exceeds that of the holes, and the device enters in the inversion regime (Figure 15c).

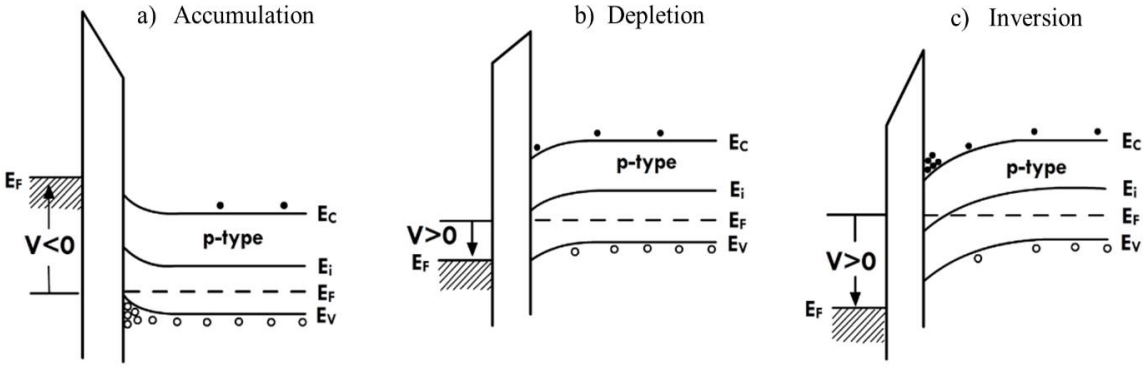

Figure 15: Bands bending in diode MIS working in different regimes: a) accumulation, b) depletion and c) inversion. Adapted from [17].

Analogous results can be achieved using an n-type semiconductor, applying biases having opposite polarity. A MOSFET is in it ON state when the applied gate voltage can generate the inversion state at the semiconductor-dielectric interface. In this circumstance, when a small voltage V_D is applied to the drain electrode, a current $I_{DS,}$ proportional the V_D, flows through the conductive channel. Here the channel behaves like a resistor thus I_{DS} has a linear trend with the applied voltage. If V_D rise further the pinch-off point is reached ($V_D = V_{D,sat}$), here the depth of the channel x_i at y=L (see Figure 16) is zero. Above this point I_{DS} remains constant as the depletion region is extended around the drain contact and the pinch-off point moves towards the source contact. The voltage in y remains constant, $V_{D,sat}$ and thus so the charge carriers coming from the source contact to y. The

output characteristic of a MOSFET is shown in Figure 16b. For a given value of gate voltage (V_G) the current follow a linear trend until, because of the channel pinch-off, it saturate its maximum value. The saturation current is higher for larger gate voltages as a larger number of charges form the channel. Important parameters such as carriers mobility, threshold voltage (V_{th}) and ON/OFF ratio are extracted and calculated from the transfer characteristics. Here, the I_{DS} is collected during a V_G sweep while V_D is kept constant to a value larger than $V_{D,sat}$.

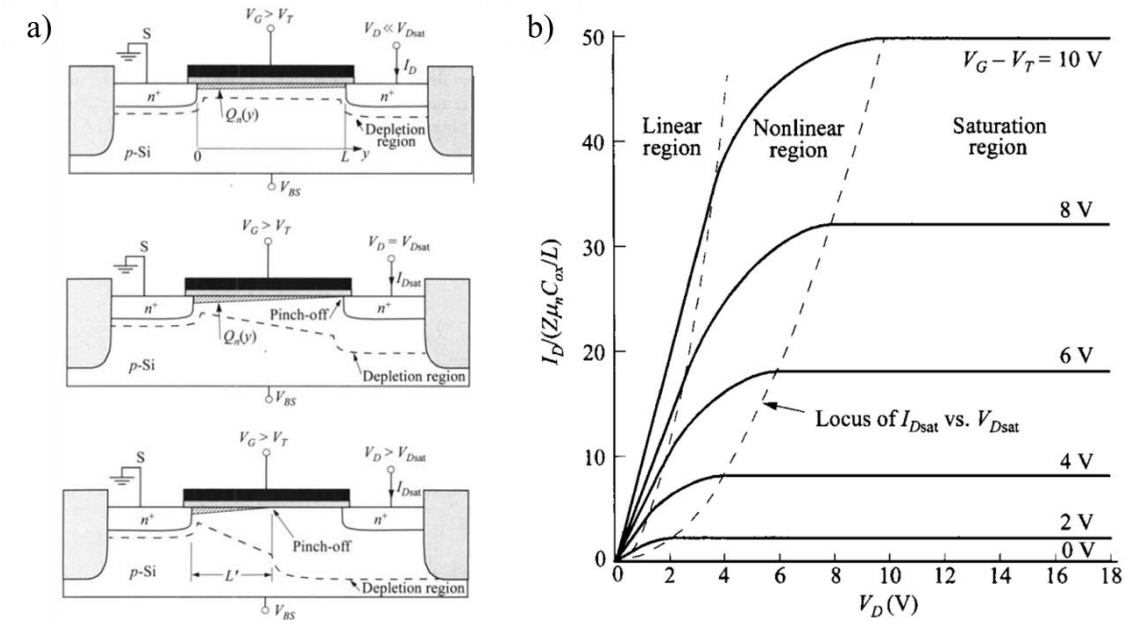

Figure 16: a) schematic of a MOSFET under V_D scan, which induces the pinch-off of the conductive channel. b) MOSFET output characteristics. Adapted from [17].

In the case of a thin film transistor (TFT) and specifically OTFT (see Figure 17) source and drain electrodes form ohmic contacts directly with the conductive channel and the gate electrode is the doped substrate. In addition, differently from MOSFETs, TFTs operate in the accumulation regime. In case of organic semiconductors the valence and conduction band edges are equivalent to the HOMO and LUMO levels, respectively. In case of OLETs, the electroluminescence is generated as the injection of both carriers in

the emitting polymer allows the excitons formation and radiative recombination. In case of largely imbalanced injection, the light is generated in the proximity of the drain electrode. Differently, in case of efficient ambipolar injection the location of the recombination zone can be shifted, within the channel, tuning the gate voltage [94].

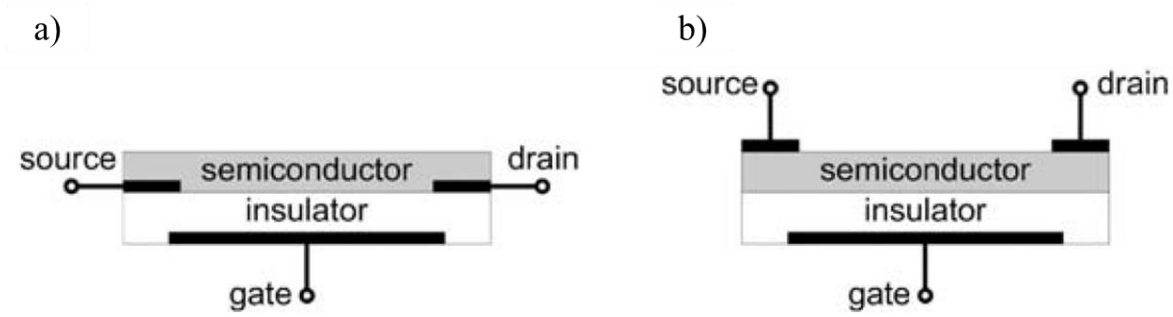

Figure 17: Device architecture for a thin film transistor (TFT). a) bottom-gate bottom-contacts configuration, b), bottom-gate top-contacts configuration. Reproduced from [17].

The simpler planar structure of OLETs devices make them suitable for display application, where the simple fabrication of pixels in the microscopic range is highly desirable. In literature have been reported OLETs showing efficiencies larger than OLEDs based on analogous active materials [95]. On the other side, such devices require large driving voltages which makes, at the moment, their use in display prototypes highly challenging.

2.5 Photochromism of diarylethenes

2.5.1 Introduction

In this work to create "smart", light responsive, devices we used different diarylethene derivatives (DAEs). They are among the most relevant families of photochromic compounds with a number of properties that make them particularly suited for technological applications. In general, the photochemical interconversion between the two isomers is highly efficient, both isomers are thermally stable and they are regarded

as the class of photochromers possessing outstanding fatigue resistance [96], [97]. Additionally, they are subjected to only minor structural changes during their isomerization reaction, which makes them ideal candidates to act as photoswitches in constrained environments like thin films [98], [99]. The most important feature of DAEs is the pronounced change of their π-electronic system during the photochemical reaction producing isomers having largely different optical and electronic properties.

2.5.2 Theoretical background

The photochromism of diarylethenes is based on the 6π-electrocyclization and cycloreversion reaction between a 1,3,5-hexatriene and a 1,3-cyclohexadiene core. As the hexatriene core is incorporated in a tricyclic structure, normally containing a two heteroaromatic moieties, its thermal cyclization to the ring-closed isomer has an endoergonic character, thus only the photochemical reaction pathway is available.

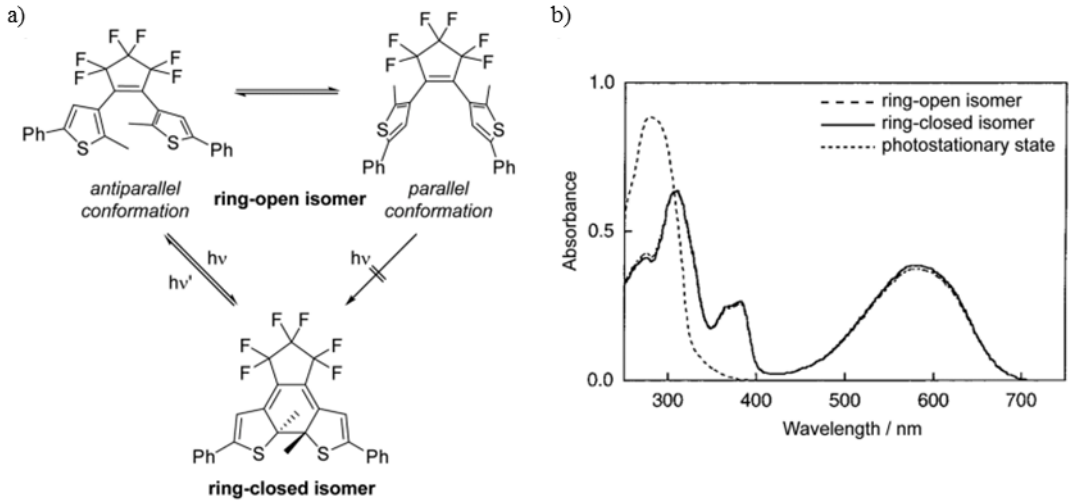

Figure 18: a) Cyclization of the antiparallel conformer of a prototype DAE. b) UV/VIS spectra of the ring-open and ring-closed isomer and the photostationary state after irradiation with 313 nm light in hexane. Reproduced from [100].

Theoretically, considering that the ring-opened isomers can be found in two energetically similar conformers, parallel and antiparallel, only 50 % of the optically excited molecules

could undergo the cyclization reaction. Such theoretical value can be largely improved if a preference of the antiparallel conformer exists in the ground state [101]. As the activation energy barrier for both cyclization and cycloreversion is high, both the isomers are thermally stable [96]. Typically the ring-open isomer absorbs in the UV region of the visible spectrum which reflects the electronically decoupled, cross-conjugated aryl moieties. After the excitation, the closed isomer extends the conjugated system over the entire molecule backbone which results in a marked, characteristic, absorption band in the visible range. As both the isomers absorb the UV light, a photostationary state (PSS) evolves, with the equilibrium composition strongly depending on the quantum yields of the forward and backward reactions. Often on the DAE core the substitution pattern choice makes the cyclization yield one order of magnitude larger than the cycloreversion, resulting in a cycloconversion of up to 90 % upon UV irradiation [101].

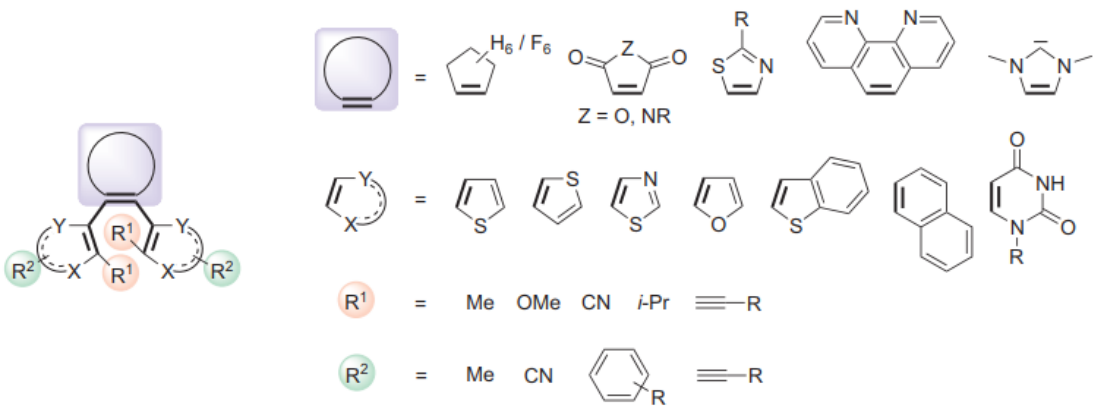

Figure 19: Versatility of diarylethenes molecular backbone. Reproduced from [102].

Differently, the cycloreversion is quantitative as only the closed-isomer presents absorption in the visible. The DAE molecular structure is extremely versatile, it ca be divided in four building blocks out of which the photochromic core has to be assembled: the bridging moiety, two hetaryl rings, substituents R1 at the ring-closing carbons and substituents R2 at the periphery of the DAE. The incorporation of the central double bond

of the hexatriene in a cyclic structure avoid the possibility of cis/trans (or Z/E) isomerization which would compete with the cyclization reaction. Placing the other two double bonds of the hexatriene system into a 5-membered hetaryl rings has a dual advantage: it ensures that cyclization is an endergonic process and at the same time, it provides an extensive conjugation, absorbing in visible range, when the closed isomer is formed. The substitution R1 on the reactive carbon is mandatory to avoid oxidation of the ring-closed isomer to the phenanthrene analogues. In addition, a relatively bulky substituent in this position will increase the population of antiparallel conformer in ground state which has positive effect on the ring-closure quantum yield. The substituents R2 the DAE "borders" may significantly influence the photochemical properties and thermal reversibility of the molecule. Two main trend have been observed: first, strong electron accepting moieties can decrease the thermal stability of the closed-form [103]; second, the more the conjugated system is extended by the substituent, the more the absorption bands (for both open and closed isomers) will be shifted towards longer wavelengths [104]. In addition, the peripheral substituent is often exploited as anchoring point for the implementation of desired specific functionalities.

2.5.3 Diarylethenes as optically controllable switches

2.5.3.1 General principles and incorporation methods

An emerging and interesting research branch involving organic thin film technology is the design and fabrication of responsive devices, able to react, changing their working regime, to external stimuli. Photochromic DAEs are particularly suited for the fabrication of such type of devices. Indeed, they offer a large optical and electronic properties variation upon isomerization, the possibility to be reversibly triggered with a large fatigue resistance. This photochromic molecules can be incorporated in thin film devices mainly

in three different ways: 1. by blending them with an organic semiconductor; 2. by depositing them as functional layer using cross-linkable DAEs derivatives; 3. by creating a self-assembled monolayer of specifically designed DAEs on a device electrode. The variation of the energy of the frontier molecular orbitals (HOMO – LUMO) upon isomerization, is the most relevant cause of the light responsivity of the thin film device performance. Indeed, DAEs in the open-form have a much larger energy gap compared to the molecule after cyclization. Depending on the specific application (see section 2.5.3.2) this unique characteristic can be exploited to generate optically switchable trap states in an organic semiconductor or charge injection/blocking layers in optoelectronic devices, resulting in a direct control of the device working regime via light irradiation.

2.5.3.2 Diarylethenes in organic thin film devices

The impact of the DAEs isomerization on electrical and optical performances has been proved for different types of organic thin film devices. In a recent work by E. Orgiu et al., specifically designed DAEs derivatives were blended with an organic semiconductor poly(3-hexylthiophene) (P3HT) [105]. The working principle of this light-responsive device relies on the introduction of photo-tuneable trap states in the bandgap of the semiconductor [106]. Indeed, the authors engineered the energy levels of the blends, Figure 20 (lines: measured via cyclic voltametry, boxes: measured via ultraviolet photoelectron spectroscopy) to influence dramatically the charge transport within the device. Specifically, two different DAEs derivatives were tested, each of them generating shallower and deeper traps states of holes in the host E_g. As expected, the latter gave the largest current variation under illumination as result of a larger trapping efficiency. Remarkably, this relatively simple approach allowed to photo-tune the device performances over repeated switching cycles without exhibiting fatigue.

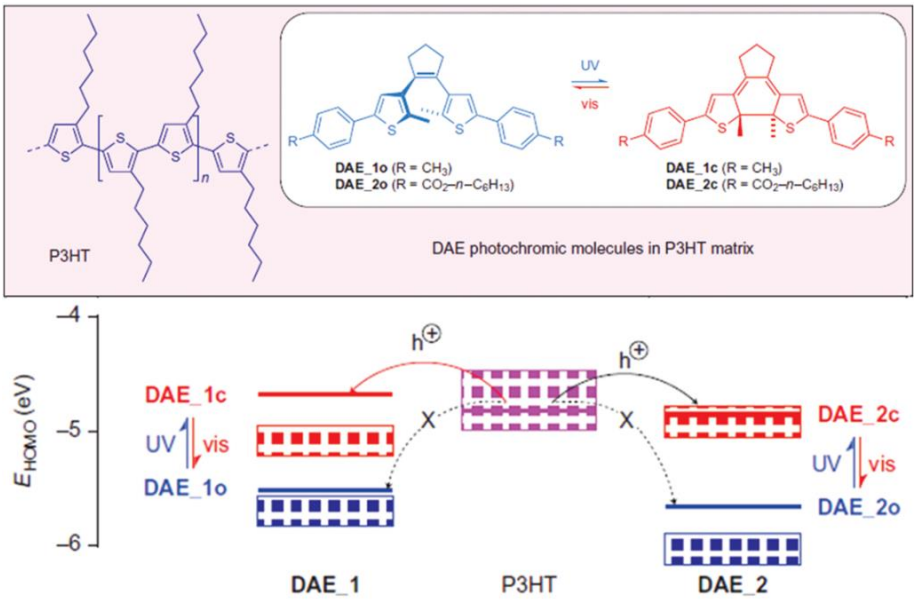

Figure 20: top: Chemical structures of the molecules used in the bi-component film, DAEs are shown it the two isomeric states. Bottom: Energy diagram of the HOMO levels of the materials involved and schematic of the holes-trapping mechanism upon isomerization. Reproduced from [106].

The most insightful works on photo-responsive two-terminal devices are about organic memories (OMEMs) and OLEDs. The group of Prof. Meerholz successfully designed and fabricated OMEMs based on cross-linkable DAE derivatives (XDTE). The authors engineered a stacked hole-transport layer incorporating the photo-switchable cross-linkable molecules. Here the DAEs isomerization, and consequent HOMO-LUMO variation, generates a photo-switchable hole injection layer which modulates the current passing through the device as a function of the irradiation dose. The fabrication of XDTE-based OMEMs having up to 15 unique logic states was demonstrated [107]. By means of in-situ reflectance absorption spectroscopy all the molecules in the closed form can be monitored, in this way, the variation of the current values can be associated to a specific fraction, X, of closed isomer. Interestingly the switching was achieved using both electrical and optical stimuli, each of them giving a different device response. In particular, the electrical switching gave larger current values for the same ratio of closed isomer.

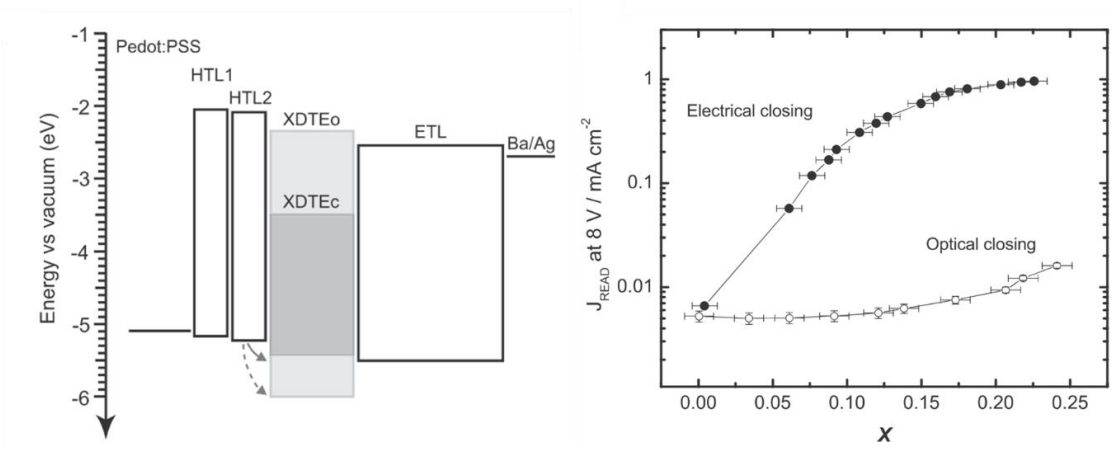

Figure 21: left: Energy level diagram at flat band condition for the solution processed multilayer device, highlighting the change in hole injection barrier between hole transporting layer 2 (HTL2) and XDTE upon isomerization (Δ HOMO = 580 mV). Right: Comparison of the JREAD response to increasing close isomer ratio (X values) for electrical (filled black circles) and optical (empty black circles) closing. Reproduced from [107].

The groups suggested that while the optical switching generates a quasi-isotropic distribution of closed DAEs in the film, the electrical switching favours a filament-like distribution which leads to higher currents [108], [109]. In the same research group, Zacharia et al., adopted cross-linkable DAEs as tuneable hole-transport layer in light responsive OLEDs [110]. Also in this work, a quite complex stack design of such layer was chosen to achieve the optimal light responsivity (ON/OFF ratio of ~ 10^3) in a blue-emitting device. Interestingly, they observed that blending their XDTE with the emissive material, resulted in an irreversibly quenching of the electroluminescence. While this approach gave successfully light-responsive devices, it is worth to stress that cross-linkable materials requires additional specific functionalities to be included during an already challenging synthetic process.

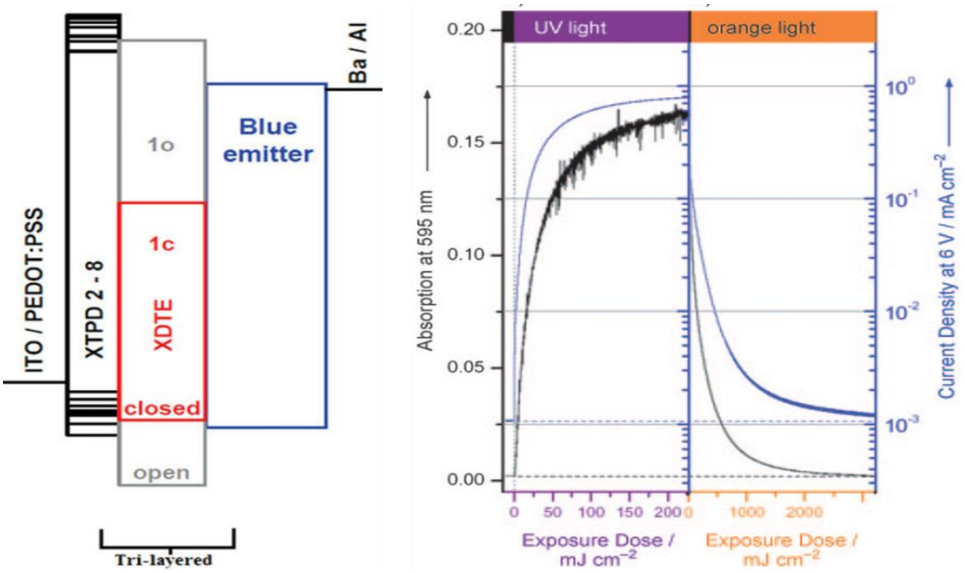

Figure 22: left: Device stack and energy levels alignment for the photo-switchable device. Right: Switching dynamics of the optimized device, simultaneously measuring the absorption of the photochromic layer (left axis) and the current density (right axis) under UV (312 nm) and visible (590 nm) light irradiation. The applied voltage was 6 V. Adapted from [110].

In 2015 Yan Qian *et al.* published a work on switchable OLEDs where a diarylethene derivative (BMTA) was blended directly in the emitting layer [111]. The three component blend was based on Methyl-9,10-bis(naphthalen-2-yl)anthracene (MADN, blue emitter) and T4TB (a previously published yellow emitter [112]) which offered a large spectral overlap between the T4TB emission and the absorption of the photochromic compound. Regardless the simple structure of this device, it showed a memory behaviour with ON/OFF ratios of luminescence and current density of 1.9 x10^3 and 1.4 x 10^2, respectively. The authors generated patterns on the emissive area via UV irradiation, with micrometric resolution, using a mask-free Digital Micro-mirror Device (DMD) micro-lithography system, see Figure 23. This work did not fully identified the leading process responsible of the device performance modulation. Indeed, upon isomerization, only holes transport can be affected as the DAEs LUMO levels variation is only ~100 meV. The authors,

initially ascribe the luminescence quenching to the hole-trapping process which is favoured by the closed BMTA.

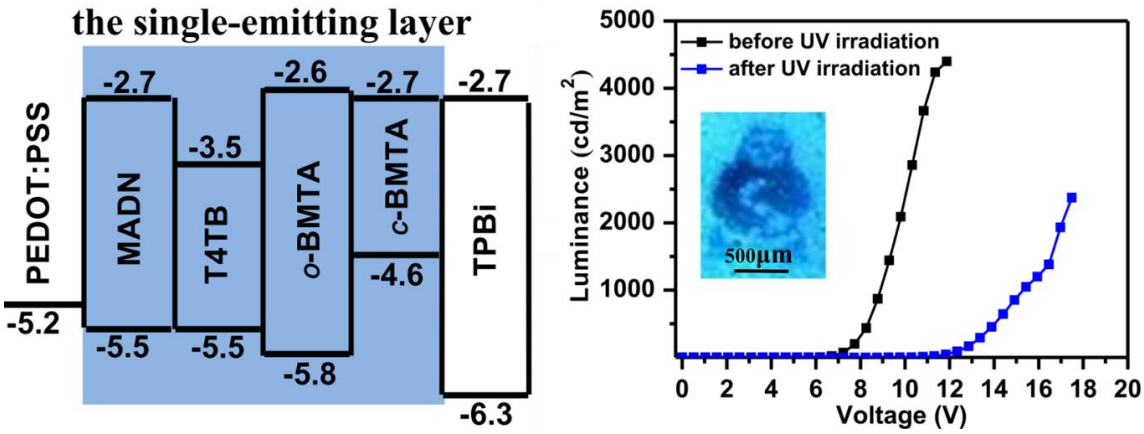

Figure 23: left: Bandgap diagram of the materials involved in the device stack (MADN, T4TB and o/c-BMTA are blended in the emitting layer). Right: luminance–voltage characteristics of the devices before and after UV irradiation (5.86 mW); inset: images of the emissive OLED (12 mm2) after micro-patterning at 8.2 V with the DMD system. Reproduced from [111].

On the other side, the control device, prepared with the same host material but without the emissive T4BT dopant, gave almost negligible current and luminescent ON/OFF ratio of 14 and 6 respectively. As conclusion, they suggest that the interplay between Förster resonant energy transfer (FRET), charge trapping and absorption form the closed BMTA isomer result in the device light-responsivity.

3 Experimental techniques

3.1 Optical properties

3.1.1 Photoluminescence quantum yield (PLQY)

In this thesis, the method used to evaluate the PLQY of emitting materials, in thin films and in solutions, has been proposed by de Mello et al. [113]. The optical set-up requires a stable laser source, an integrating sphere and a spectroradiometer. The laser is the exciting beam and must have its peak wavelength in the phosphour absorption range. The integrating sphere is internally coated with a highly reflective material such as barium sulphate or Teflon (PTFE). The exit port of the integrating sphere must be equipped with a shutter which prevents any radiation to reach the detector without being diffused in the sphere. The PL quantum yield for a specific emitting material is the ratio between the photons emitted over those absorbed upon optical excitation.

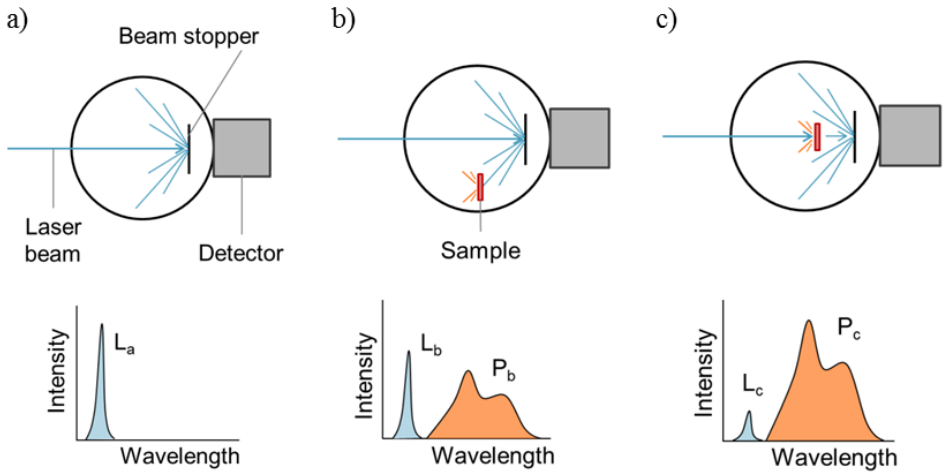

Figure 24: Experimental steps for the PLQY calculation via three separate acquisitions. a) Empty integrating sphere, b) the sample is in the sphere but the laser is not impinging on it, c) the laser impinging on the sample. Reproduced from [27], *originally revised from* [113].

Experimentally, is it possible to calculate this value through three different PL acquisitions, indicated by the letters A, B and C as shown in Figure 24. In experiment A,

no sample is placed in sphere and the collected signal is the incident beam, the photons potentially impinging on the sample. The sample is placed in the sphere during experiment B, but it does not intercept the exiting beam. Here the collected signal is the composition of the light source, which is diminished by the amount of scattered light absorbed by the sample, which triggers a weak PL signal. In experiment C, the sample intercepts the incident beam (the sample orientation must avoid the reflected beam to leave the sphere through the entrance port). The collected signal will present a larger intensity reduction of the exciting peak, due to the direct and scattered light absorption from the sample, and the corresponding larger PL signal. In each case, the area under the laser profile is proportional to the amount of unabsorbed light, we refer to this area as L_a, L_b and L_c. The area under the emission profile, P_b and P_c, is proportional to the amount of emitted light. By the analysis of these spectra, it is possible to extract the absorption coefficient and the external PL quantum efficiency for the sample with the following formula:

$$\mu_{PL} = \frac{P_c - (1 - A)P_b}{L_a A}\ , \quad A = (1 - \frac{L_c}{L_b})$$

Where A is the absorption coefficient.

3.1.2 Time-correlated single-photo counting

Time-correlated single-photon counting (TCSPC) is a techniques for PL lifetime measurements [37]. The principle of TCSPC is described in Figure 25. The sample is excited with a short pulse of light, in Figure 25a is shown the waveform obtained if many fluorophores were excited and a large number of photons were collected simultaneously. In reality the conditions are adjusted so that less than one photon is detected per laser pulse, the detection rate is typically 1 photon per 100 excitation pulses. The time is

measured between the excitation pulse and the observed photon and it is stored in a histogram where the x-axis is the difference between the excitation pulse and detected photon. When much less than 1 photon per exciting pulse is detected, the histogram represent the waveform of the decay. Differently, the measurement is biased to shorter times, as, at present, only the first photon can be detected.

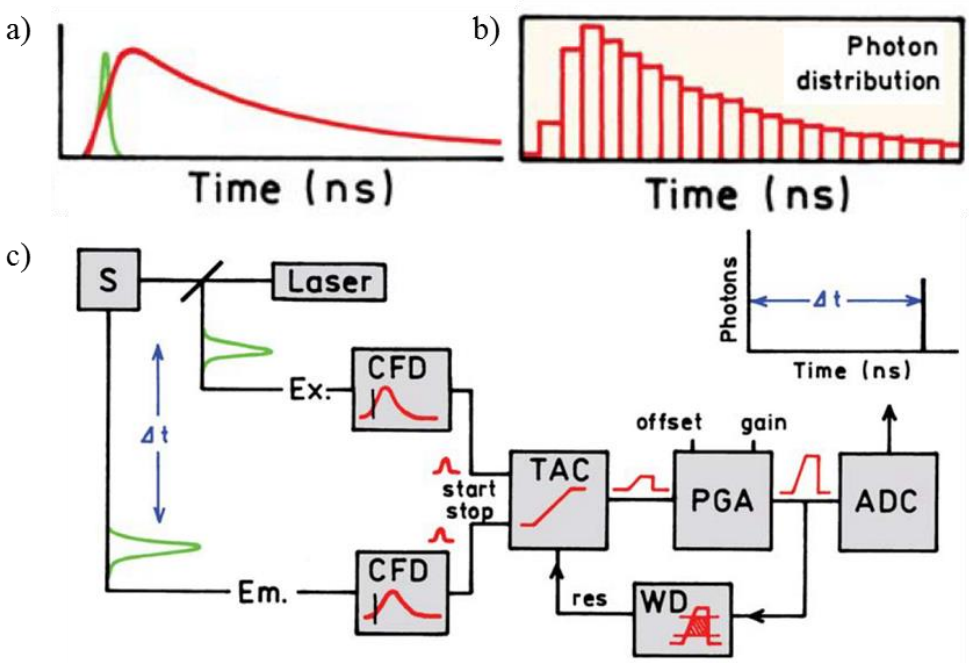

Figure 25: Time-correlated single photon counting measurement. a) Excitation peak and PL waveform, b) histogram describing the collected photon distribution, c) schematic of the equipment electronics. Adapted from [37].

The experiment starts with the excitation pulse that sends a signal to the electronics and impinges on the sample, see Figure 25c. This signal passes through a constant function discriminator (CFD), which accurately measures the arrival time of the pulse. The time-to-amplitude (TAC) is triggered and generates a voltage linear ramp in the nanosecond scale. A second channel detects the pulse from a single detected photon. The arrival time of the signal is accurately determined via a second CFD which send the signal to stop the

voltage ramp. The TAC now contains a voltage value proportional to the time delay (Δt) between excitation pulse and the collected photon. It is amplified via a programmable gain amplifier (PGA) and converted to a digital value through an analog-to-digital converter (ADC). A window discriminator (WD) minimized the possibility of false readings as it restricts the voltage ranges within a specific limit. The probability histogram is built summing over a sufficient number of detection cycle. For the interpretation analysis of the PL decay signal it is important to consider the instrument response function (IRF), defined as the response of the instrument at zero lifetime sample. The width of the IRF arise from the width of the excitation pulse and the time accuracy of the detector and electronics. IRF is obtained performing a TCSPC measurement using a highly scattering not emissive sample.

Once the time-resolved PL decay is detected, the relevant parameters are extracted through a reconvolutive exponential fitting on the decay. The fitting uses exponential functions of the form:

$$R(\mathrm{t}) = A + \sum_{i=1}^{n} B_i e^{-\frac{t}{\tau_i}}$$

Where n is the number of decay times, B_i are the pre-exponential factors, τ_i the lifetimes and A is a constant that takes into account the background. The quality of the fitting is assessed with a least-squared analysis where the χ^2 gives the goodness-of the fit. Time resolved fluorescence decay were collected via the spectrometer Lifespec II (Edinburgh Instruments).

3.2 Organic optoelectronic devices

3.2.1 Light measurement: radiometric vs photometric units

The device electroluminescence can be expressed either in radiometric or photometric units. While the former refers to the number of photons emitted, the latter weight the light intensity to the sensitivity of the human eye. As consequence, photometric units can be used for wavelengths in the visible range, differently, radiometric units must be used for emission at wavelengths above 700 nm or below 350 nm.

In radiometric units the light intensity is expressed as radiance in W sr^{-1} m^{-2}, while the luminance, in cd m^{-2} (or nit), is the analogous measurable in case of photometric units. Commercial apparatus have luminance performances ranging from ~ 300 cd m^{-2} up to thousands cd m^{-2} for illumination. The candela (cd) in the unit of luminous intensity according to the SI, it is defined as: '[…] the luminous intensity, in a given direction, of a source that emits monochromatic radiation of frequency 540 10^{12} hertz and that has a radiant intensity in that direction of 1/683 watt per steradian'. The selected frequency converts in 555 nm, the wavelength at which the human eye is most sensitive. The steradian (sr) is the SI unit for the solid angle (Ω). In OLED and OLET devices are approximated to Lambertian light sources where the luminous intensity is proportional to the cosine of the angle between the normal to the emitting surface and the direction of the observer.

3.2.2 OLEDs

3.2.2.1 Fabrication

The OLED reported in this thesis were fabricated as follows. Commercially available ITO coated (150 nm) glass substrates substrate (from Ossila, 20 Ω/square) were cleaned via ultrasonication in different solvents (5 minutes each) having decreasing polarity (de-

ionized water, acetone and iso-propanol). After drying via a nitrogen gun, the substrates underwent a 10 minutes long oxygen plasma treatment (Harrick PDC-002), at an oxygen pressure of $1.1 \cdot 10^{-1}$ mbar. Such treatment had a dual effect as it ensures the removal of organic contaminants to a molecular level and increases further the ITO work function [114], [115]. The hole injection layer (PEDOT:PSS from Sigma Aldrich) was filtered, through a 0.2 μm porous filter, and spin-coated at 4000 rpm to a thickness of ~ 40 nm. The sample was then baked at 170 ºC for 10 min in N_2 atmosphere. In glove box the emitting layer was spin-coated at 1200 rpm to a thickness of ~100 nm. The layers thicknesses were determined via profilometric measurements. In high vacuum (10^{-6} mbar), a 30 nm thick Ca electrode and a 150 nm thick capping layer of Al were thermally evaporated. Devices were encapsulated using glass coverslips and UV-curable epoxy resin.

3.2.2.2 Characterization

The current density and luminance versus voltage (JVL) characteristics was measured with a Keithley 2400 source-meter and a calibrated Si photodiode (having an area of 100 mm^2 and placed at 4.5 cm from the device) connected to a Keithley 2000 multimeter via a signal amplifier. Details about the data elaboration routine can be found in sections 9.1 and 9.2. A unified model has been recently proposed to interpret the current-voltage characteristics in the space charge limited regime (SCLC) [71].

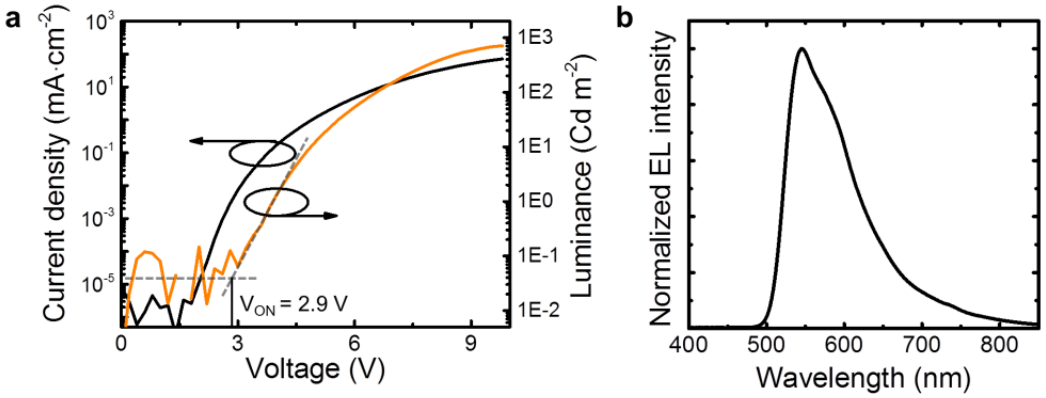

Figure 26: a) OLED JVR device characteristics, b) Normalized F8BT-based OLED electroluminescence spectrum (arbitrary units). Reproduced from [27]

At low voltage a linear trend is observed which can be described the Ohm's law. For higher voltages, the curve is fitted by a quadratic function called Child's law and, finally, the last region is described with a higher than quadratic relationship where mobility is dependent on temperature, electric field and/or charge carrier concentration. Currents below the threshold voltage are due to micro short circuits, imperfections and are referred to as residual leakage current. The device V_{ON} is extracted as the voltage at the intercept between the noise level and the linear fit on the luminance curve (see Figure 26a), from the semi-logarithmic plot of the EL intensity versus the voltage. The EL spectrum is collected with an ANDOR-Shamrock spectrograph coupled with an ANDOR-Newton charge-coupled device (CCD) unit.

3.2.3 OLETs

3.2.3.1 Fabrication

OLET devices in this thesis were fabricated on commercially available substrates of n^{++} Si as bottom gate and 230 nm of thermally grown SiO_2 as gate dielectric (IPMS Fraunhofer Institute). Interdigitated gold source and drain electrodes are pre-patterned with a channel width of 1 cm and a length of 2.5 µm. The substrates were cleaned by

ultrasonication in acetone and isopropanol for 20 min, dried with a nitrogen gun, and then treated with UV/ozone for 5 min (Novascan, Digital UV Ozone system). A self-assembled monolayer of Octadecyltrichlorosilane (OTS, Sigma-Aldrich) was chemisorbed on SiO_2/Si substrates by immersion of the substrates in a 10 mM OTS in toluene at 60 °C for 2 h before they were left at room temperature overnight in the glove box, and washed with toluene and isopropanol. The photo-responsive blend is generated via a two-steps intercalation process. First the emitting polymer is spin-coated on the substrate and thermally annealed in a nitrogen-filled glovebox. Then, the photochromic dopant, dissolved in n-butyl acetate, a bad solvent for the underlying polymer, is spun on it. The subsequent annealing step is vital for the diffusion of the dopant in the emitting matrix.

3.2.3.2 Characterization

Devices were characterized in a dry and nitrogen-filled Mbraun glove-box. Electrical characteristics of OLETs were collected through the PM5 Cascade Microtech probe station connected to a Keithley semiconductor analyser model 4200-SCS. The light output of devices was calculated from the photocurrent signal of a calibrated silicon photodiode, amplified by the Eg&G Instruments 5182 preamplifier. The area of the photodiode is 15 mm2, the distance between device and photodiode amounted to 5.2 mm, and the area of device emissive was 0.025 mm2, see Figure 27a. Electrical and optical characteristics were collected simultaneously. The EL spectra of emitting devices were collected via an optical fibre connected to an ANDOR-Shamrock 163 spectrometer coupled to an ANDOR-Newton charge-coupled device (CCD) unit Figure 27b.

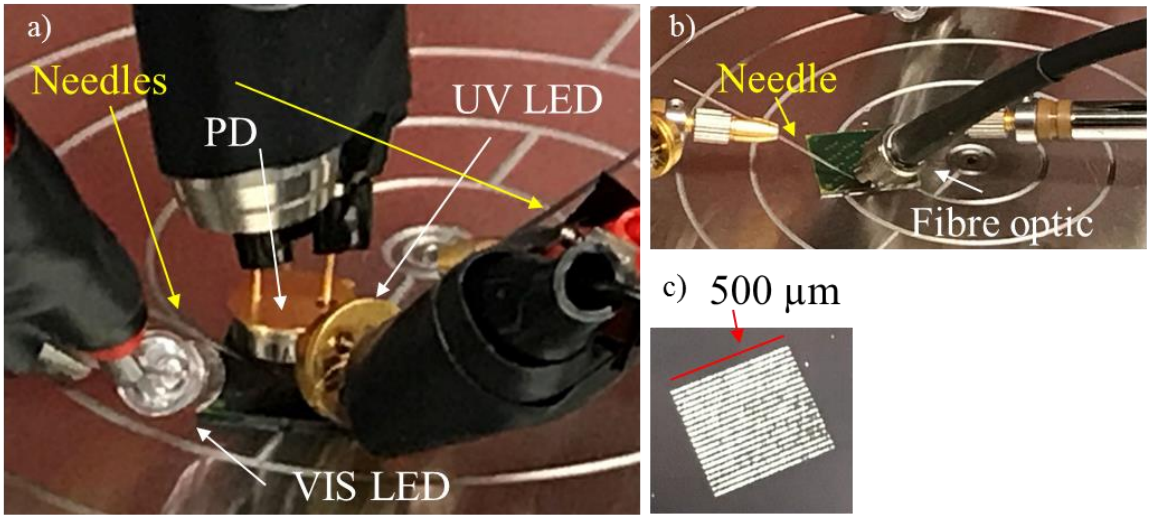

Figure 27: OSOLETs characterization. a) Experimental setup for the optoelectronic characterization and irradiation of the device, b) Experimental setup for the collection of the device electroluminescence, c) Micrograph of the OSOLET electroluminescence.

At first, an output characteristic (scanning on V_{DS} for different V_{GS} values) was carried out on our devices to assess their electrical behaviour as transistors and identify the V_{DS} range in which the device was in the saturation regime. Afterwards, the trans characteristic (scanning on V_{GS} at $V_{DS} > V_{DS,sat}$) was performed. The latter allows one to access the key parameters of a FET, which are the carrier field-effect mobility (µ), the on/off ratio and the device threshold voltage (V_{th}). The mobility quantifies the average drift velocity of the carriers per units of electric field, while, the on/off ratio is calculated between the I_{DS} value for the device in the on (above the V_{th}) and off (below the V_{th}) states. The threshold voltage (V_{th}) is the minimum gate bias to be applied to the device to induce the accumulation regime. The charge carriers field-effect mobility can be calculated via the linearization of the equation below, which describes the I_{DS} in the saturation regime.

$$I_{DS,sat} = \frac{WC_i\mu(V_{GS} - V_{th})^2}{2L}$$

Here, C_i is the gate insulant capacitance, while W and L are the conductive channel depth and length, respectively. The on/off ratio changes depending on the V_{GS} values at which the IDS is sampled for the calculations, generally the values for V_{GS} = 0 V, for the off state, and V_{GS} = -100 V (in case of p-type semiconductors) are used.

4 Optically Switchable Organic Light-emitting Diodes (OSOLEDs)

In this chapter is described the design, fabrication and characterization of OSOLEDs based on poly(9,9'-dioctylfluorene-alt-benzothiadiazole) (F8BT) doped with a diarylethene derivative. The specific materials selection was guided by energetic and spectroscopic considerations which are addressed in the following sections. The photochromic activity of the dopant in the solid state has been investigated both via UV and PL spectroscopy, while the blend morphology was measured via AFM. Light responsive devices embedding different loading dopant (1, 2.5, 5 and 10 w/w %) showed optical responsivity. The impact of the diarylethene isomerization on the charge carriers was separately investigated, for the first time, via the design, fabrication and characterization of single-carrier switchable device. Furthermore, the same blend was used to attempt the fabrication of switchable µ-OLED.

The diarylethene derivatives were received from Dr. Aurelio Bonasera from the Prof. Stefan Hecht's group (Humboldt University of Berlin) who also determined the HOMO/LUMO level for the materials. The ITO patterning via laser ablation to the meso-scale was performed, during an industrial secondment, at Scriba Nanotecnologie s.r.l (Bologna, Italy) under the supervision of Dr. Thomas Mosciatti and Dr. Pierpaolo Greco.

4.1 Active layer design: materials selection

We designed the device emitting layer (EML) to generate optically switchable trap states for both holes and electrons and thus achieve a marked light responsivity, as the transport of both the charge carriers can be optically hindered. We blended the well-known green-

emitting polymer F8BT with a specific DAE derivative characterized by a fluorinated bridge and trifluoromethylated harms (hereafter named DEA_tf); molecular structures and optical characterization of these compounds are shown in Figure 28a-b. The materials selected for the blend are the result of a judicious evaluation over a number of aspects. First of all, F8BT is a highly performing fluorescent polymer, which has been largely studied and which have a marked ability to transport electrons, a desirable property for optoelectronic applications. On the other side, to ensure the necessary light-responsivity and reliability of device performances we choose DAEs as photochromic switches. Indeed, high fatigue resistance and the ability to reach up to 96% of closed-isomer at the photo-stationary state (PSS) have been already reported for this class of materials [116], [117]. Specifically, HOMO and LUMO levels of the DEA_tf closed isomer (photo-generated after UV irradiation) creates a type I junction with the frontier molecular orbitals of the fluorescent matrix as shown in Figure 28c. In this situation, the transport of both holes and electrons within the organic blend is hindered due to the photo-generation of trap states at energies ~ 200 – 300 meV from the host bandgap edges. Additionally, the large spectral overlap between the F8BT fluorescence and the c-DEA_tf absorption spectrum should favour the host-guest energy transfer which is expected to further reduce the device brightness. It is worth to mention that a potential drawback related to the pronounced host-guest spectral overlap, might be the self-switching of the DAE-tF to its open form due to the host emission. Conversely, visible light irradiation triggers the reversible photochemical reaction switching the DAE to its open form o-DEA_tf as demonstrated via absorption and photoluminescence spectroscopy in section 4.3.1. In this case, HOMO and LUMO levels of the dopant lay outside the F8BT bandgap, thus the charge carriers transport in the matrix is restored.

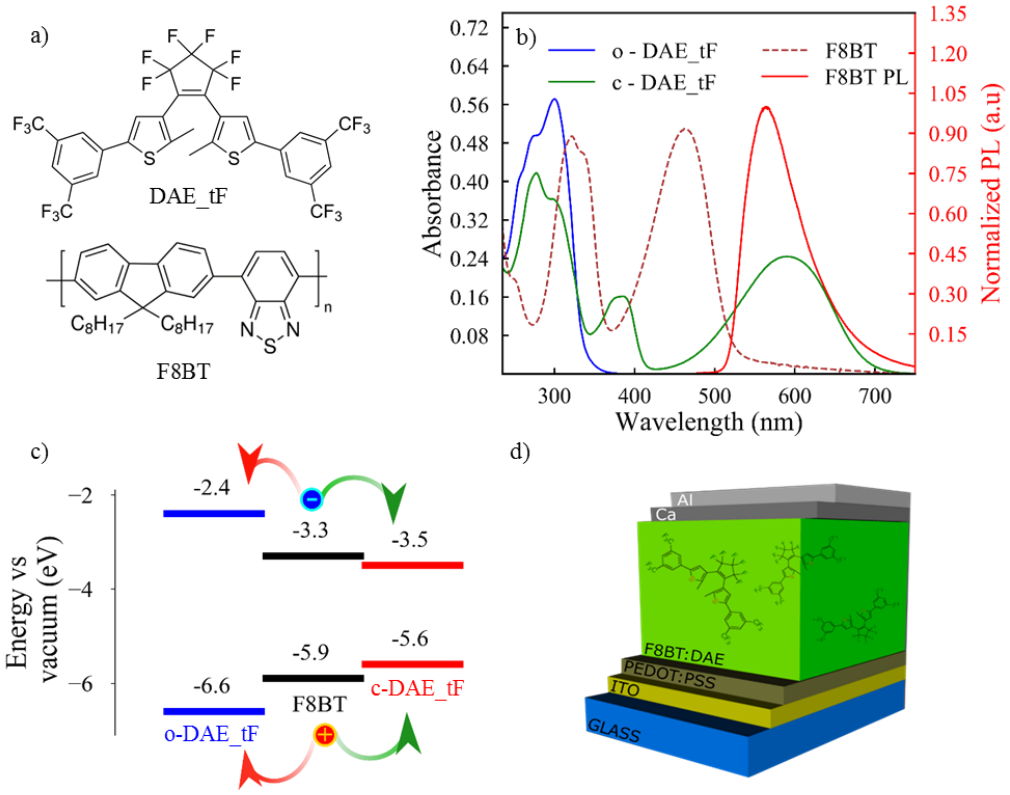

Figure 28: Emissive layer design, host (F8BT) and photochromic guest (DAE_tF) materials properties: a) molecular structure; b) absorption and normalized PL spectra (DAE_tF in acetonitrile $3 \cdot 10^{-5}$M, F8BT in the solid state); HOMO-LUMO levels alignment after irradiation, d) Optically Switchable OLED architecture.

We fabricated solution-processed emitting devices having the architecture ITO (150 nm)/PEDOT:PSS (40 nm)/F8BT:DAE 5wt% (90 nm)/Ca (30 nm)/Al(150 nm) as shown in Figure 28d.

4.2 Experimental details

4.2.1 Materials and characterizations

Fused silica and ITO-coated glass substrates (Ossila, 20 Ω/square) were cleaned following the procedure described in section 3.2.2.1. In a N_2 filled glovebox, F8BT (Ossila, Mw < 250000 g/mol) and DAE-tF were dissolved in anhydrous toluene and

chloroform (10 mg/ml), respectively, left stirring overnight, filtered via a PTFE filter (pores of 0.2 μm) and then used to prepare blends F8BT:DAE-tF having concentrations of 1, 5, 10 and 20 w/w % . After stirring for further 3 hrs, F8BT and the blends solutions were spin-coated (1200 rpm, thickness of ~ 100 nm) on fused silica substrates for optical and morphological investigations. Following the same procedure, polystyrene (PS – Sigma-Aldrich, M_w ~ 350000 g/mol) was dissolved in chlorobenzene to a concentration of 50 mg/ml and used to prepare the PS:DAE-tF blend with 20 w/w % concentration. Film thicknesses were measured using a Dektak stylus profilometer. Surface morphology investigation of the blends under study has been performed in air via AFM (Bruker Dimension Icon – PeakForce tapping mode) on an area of 1 μm^2.

The absorption spectra after UV (~ 9 minutes) and visible (~ 15 mins) irradiation were collected using the Agilent 8453 spectrophotometer. LEDs emitting in the visible (528 nm, 7 mW) and UV (315nm, 0.6 mW) were fixed on the equipment and connected to a microcontroller to allow the in situ sample irradiation.

Using the same irradiation conditions as the UV/VIS absorption measurement, the PL spectra of pure F8BT and F8BT:DAE-tF 20 w/w % blend, in the solid state, were measured in air, at room temperature. The photo-excitation at 450 nm was provided by a xenon lamp coupled with a Bentham monochromator, the spectra were collected with an ANDOR-Shamrock 163 spectrometer coupled with an ANDOR-Newton charge-coupled device (CCD) unit.

4.2.2 Device fabrication and characterization

Blends of F8BT:DAE-tF (1, 5 and 10 w/w %) were used to realize optically switchable OLEDs, single carriers devices and micro-OLEDs. Methods for the OLED fabrication and characterization are reported in section 3.2.2. The device photo-responsivity was

assessed irradiating them using UV (315 nm, 0.6 mW, ~ 7 min) and VIS (528 nm, 7 mW, ~ 13 min) LEDs connected to a micro-controller.

4.2.3 Micro-OLEDs: direct laser lithography for electrodes patterning

A nickel sheet (thickness: 100 μm) was used to fabricate the evaporation mask. The mask was patterned with the Marko Laser Maker equipped with a pulsed Nd:YAG IR laser, centred at $\lambda = 1064$ nm. Typical cutting parameters were a laser pulse power of 8 W and a repetition rate of 20 kHz. The nickel plate was put freestanding on the Marko's stage using four magnets. The stage is equipped with motors which can move it in the X−Y directions. The position of the focal point of the laser beam was controlled by moving the laser head in the Z direction. The movement was controlled with an accuracy of 1 μm in the X − Y − Z directions. The ablation pattern was designed via a CAD software and transferred to the machine. The optimal cutting speed was found to be 20 μm s^{-1}. A total of 25 passages were needed to achieve a complete cut of the metal plate. The mask was then polished and cleaned. Finally, a sonication in ethanol for 10 min was performed to ensure complete removal of all the remaining metallic powder and polish paste.

The same machine was used to produce ITO micro-patterns on our ITO-coated glass substrates. Here, the laser writer was used in the "raster mode" at a power of 1W and pulse frequency of 20 KHz. In this condition we were able to completely ablate the ITO layer in specific areas.

4.3 Blend characterization

We carried out optical and morphological investigations on the blends to assess the retention of the DEA_tf photochromic activity in the solid state, the impact of the dopants on the matrix PL and the presence of phase segregation between host and guest materials.

4.3.1 Optical switchability of diarylethenes in the solid state

To facilitate the optical characterization of the DEA_tf photochromism in the solid state, the DAE dopant was blended, at 20 w/w % with a transparent, non-conjugated polymer, polystyrene (PS). Indeed, the PS negligible absorption in the visible range, allows to emphasize the blend spectral variations due to the dopant isomerization. Such blend was spun on amorphous silica and characterized via UV-VIS absorption. Figure 29a-b shows the blend absorption spectra under UV and visible irradiation, respectively. We can observe how the absorption band in the visible range, a distinguishing feature of the DAE closed isomer, gradually grows under UV irradiation while vanishes under visible light. The study of the reaction reversibility in the solid state was carried out over several irradiation cycles. The spectra collected ware elaborated to subtract the matrix contribution to the overall absorption spectrum and emphasize the DEA_tf isomer fingerprints. The elaboration process is briefly described in Figure 29c: the blend absorption spectrum (A, B, C, etc.) is collected after each irradiation step; each spectrum is the overlap of the matrix (rectangle 'M' in Figure 29c) and the DAE (triangle in Figure 29c) contributions. While the former is constant during all the acquisitions, the latter will have a specific profile depending on the DAE photo-isomerization. Thus the matrix contribution can be filter out by subtracting to each absorption spectrum the one collected during the previous irradiation step to give what we plot as "Δ Absorbance", see Figure 29d. Such signal has positive and negative contribution depending on the specific irradiation step. When data from multiple irradiation cycles result overlapped in a symmetric (to the x axis) plot, it is the symptom of a fully reversible photochromic reaction, as clearly shown in Figure 29d for our blend.

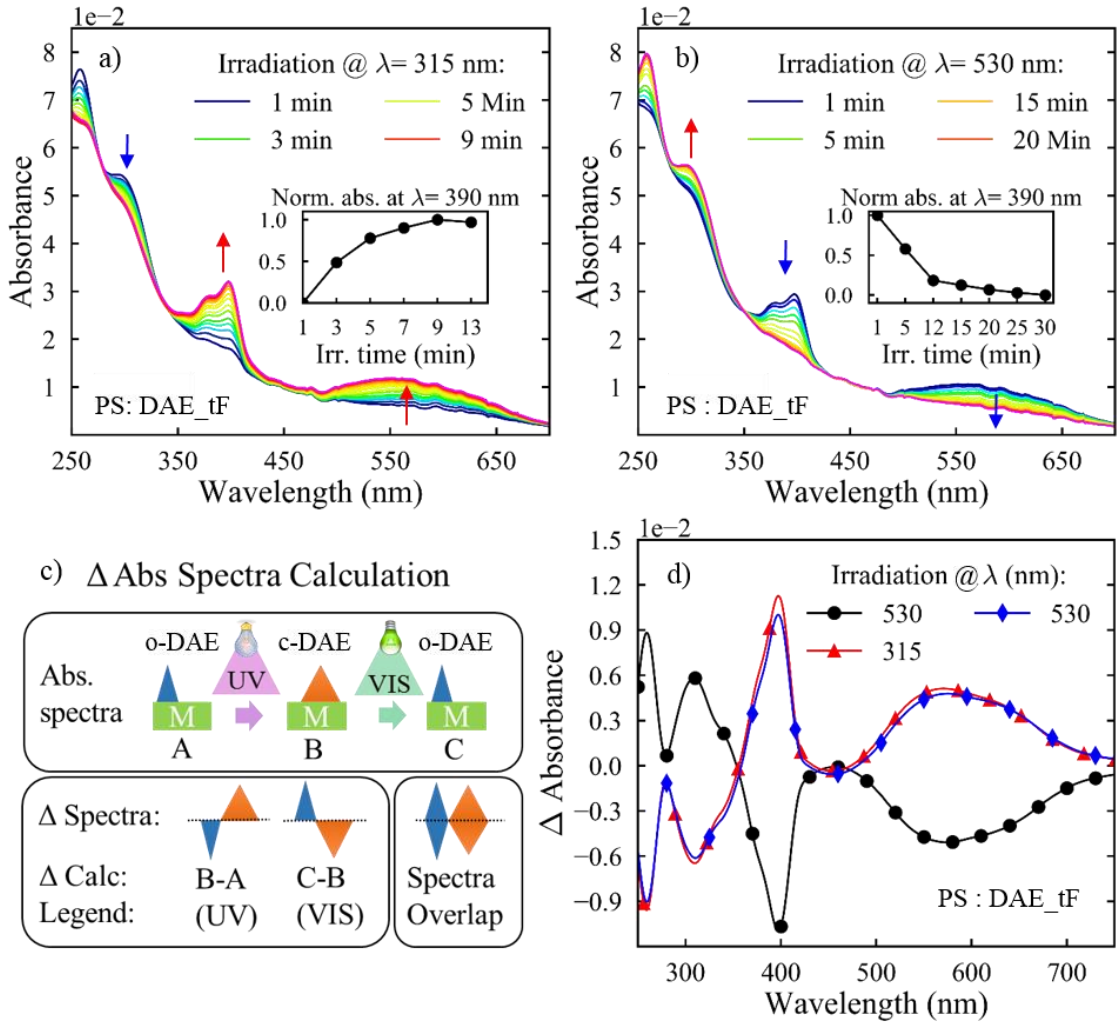

Figure 29: DAE_tF photochromic activity in the solid state (blended, 20 w/w % with PS): absorption spectrum under UV ,from open to close form,(a) and VIS, form close to open form, (b) irradiation. Inset: normalized absorption signal collected at 390 nm; c) schematic on the Δ absorption calculation steps; d) DAE_tF Δ absorption plot for UV (9 min) and VIS (15min) irradiation steps, markers on selected data-points as 'guide to the eye' only.

To further characterize our blend, we studied the impact of the dopant photochromic activity on the F8BT fluorescence. We spun the 20 w/w % blend on fused silica substrates and collected the F8BT emission after each irradiation step. As shown in Figure 30a, the blend emission (peak integral) drops consistently after UV irradiation (~ 25 %), while it fully recovers after VIS irradiation.

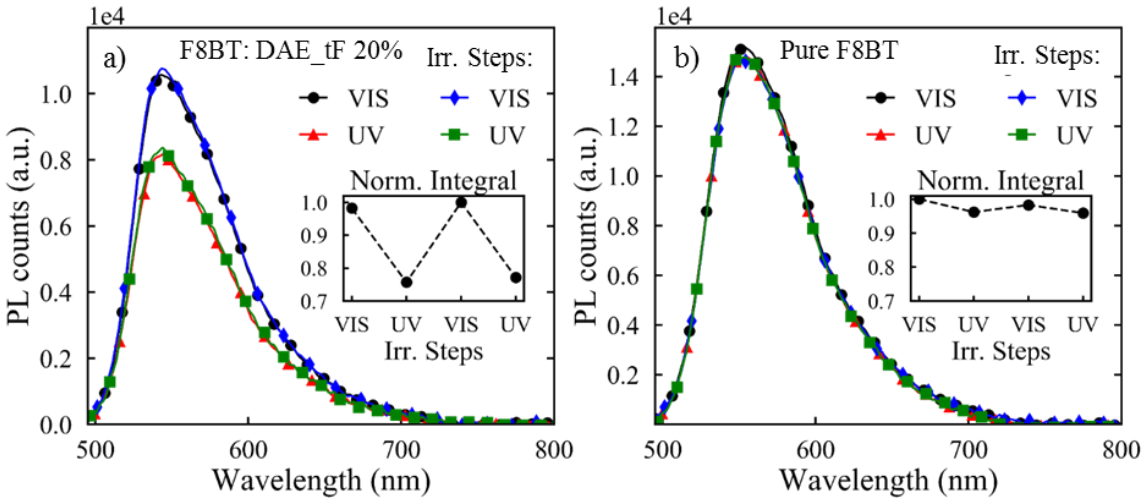

Figure 30: Thin film PL intensity after UV/VIS irradiation: a) F8BT:DAE_tF 20 w/w %; b) neat F8BT. In the insets the normalized variation of the PL peak integral. Markers on selected data-points as 'guide to the eye' only.

Such PL variation can be ascribed to the large host-guest spectral overlap (see section 4.1) which favours PL host-guest FRET and, in certain extent, self-absorption. Differently, the neat polymer (see Figure 30b) shows a fairly constant fluorescence signal under UV and VIS light irradiation.

4.3.2 Thin film morphology

We investigated the surface morphology of thin films of pure F8BT and the most concentrated F8BT:DAE-tF blend via atomic force microscopy, see Figure 31.

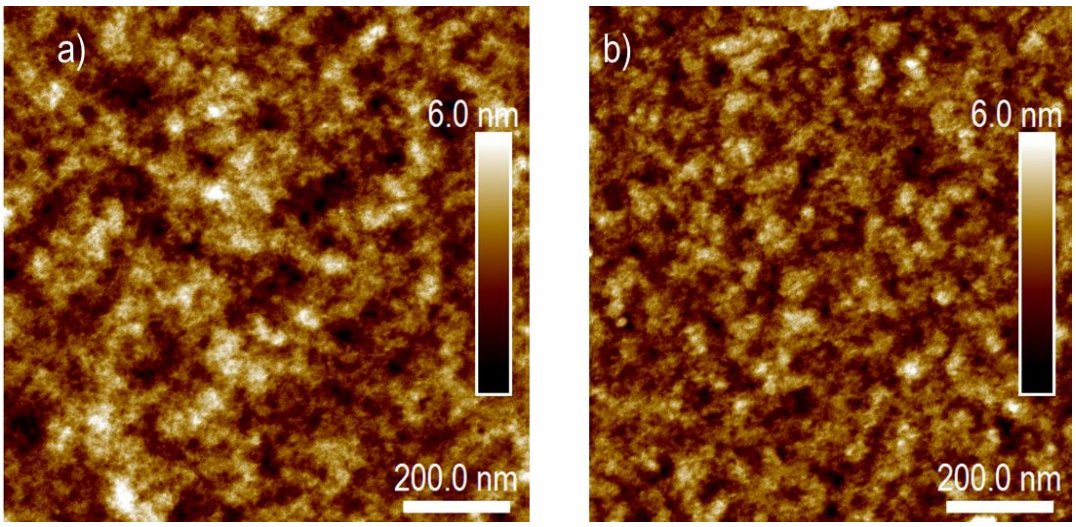

Figure 31: Surface morphology analysis: AFM images of neat F8BT (a) and F8BT:DAE-tF w/w 10% blend (b).

The images does not show major variations in the morphology and this is confirmed by the roughness root mean square (Rrms) values of 0.81 ± 0.15 nm for the neat polymer and 0.79 ± 0.03 nm for the 10 w/w % blend.

4.4 OSOLEDs performance under light irradiation

Solution-processed OLEDs based on F8BT blends (see section 4.1), with increasing concentrations of DAE-tF (1, 5, and 10 w/w %), were fabricated and characterized. In Figure 32 and Figure 33 we report the electrical and optical characteristics of such devices after the UV and visible irradiations. The OLEDs based on pure F8BT (see Figure 32a-b) do not show any photo-responsivity and/or reversible performance variation. Specifically,

the initial drop in current density and luminance after the first UV irradiation, not only is not recovered, but it is worsened after the device exposure to the visible light.

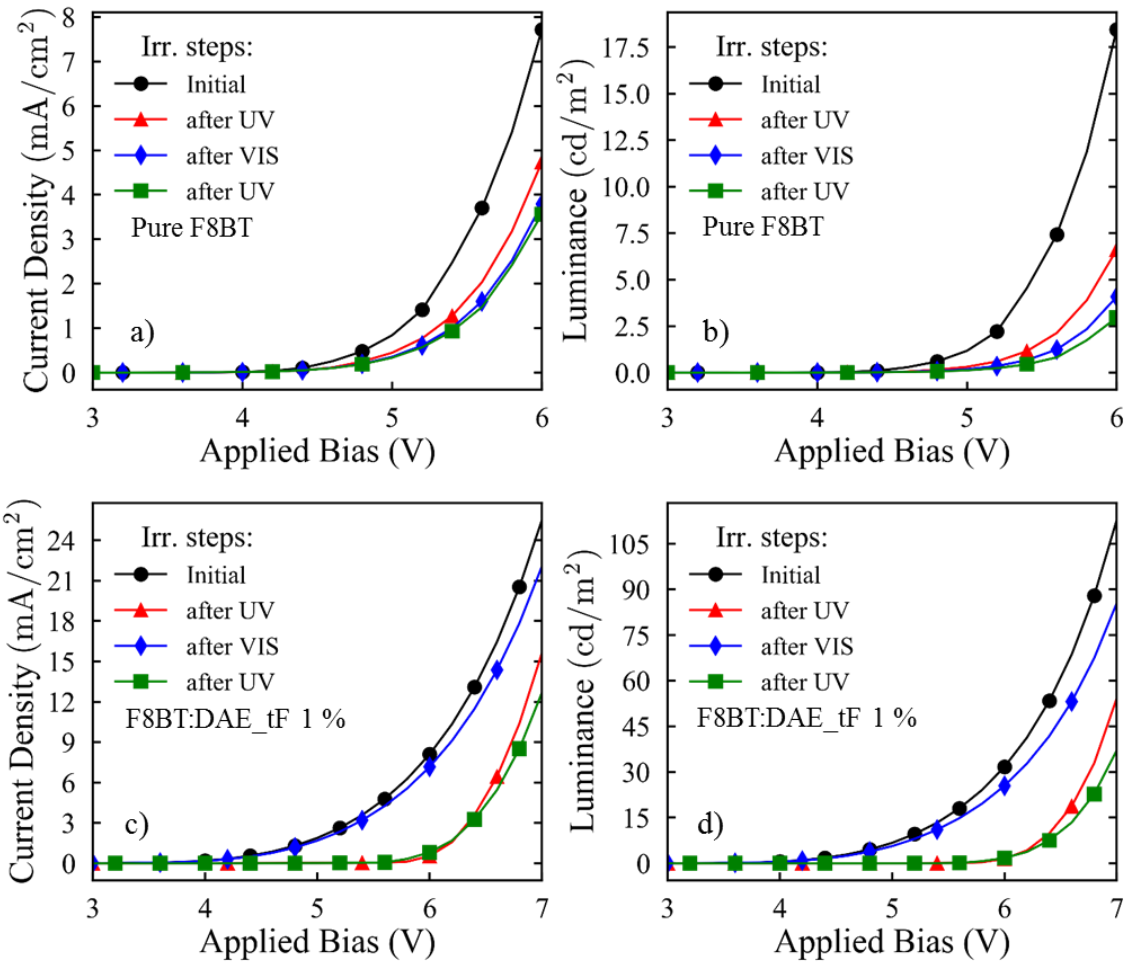

Figure 32: Effect of UV (315 nm, ~ 7 min) and VIS (528 nm, ~ 13 min) irradiation on OLEDs based on pure F8BT and F8BT:DAE_tF 1 w/w % blend. Markers on selected data points as 'guides to the eye' only.

Notably, in the second cycle of irradiations the device performance tends to remain fairly constant. Blending the F8BT with DAE-tF leads to the device light-responsivity already at low dopant concentrations, Figure 32c-d. As expected, the UV irradiation switches the DAEs in their closed form and they act as trap-states for the charge carriers, thus hindering the transport property of the blend. Indeed, the larger trapping effect becomes

evident with the increasing threshold voltage (V_{ON}) shift, after UV irradiation, observed for higher DAEs loadings.

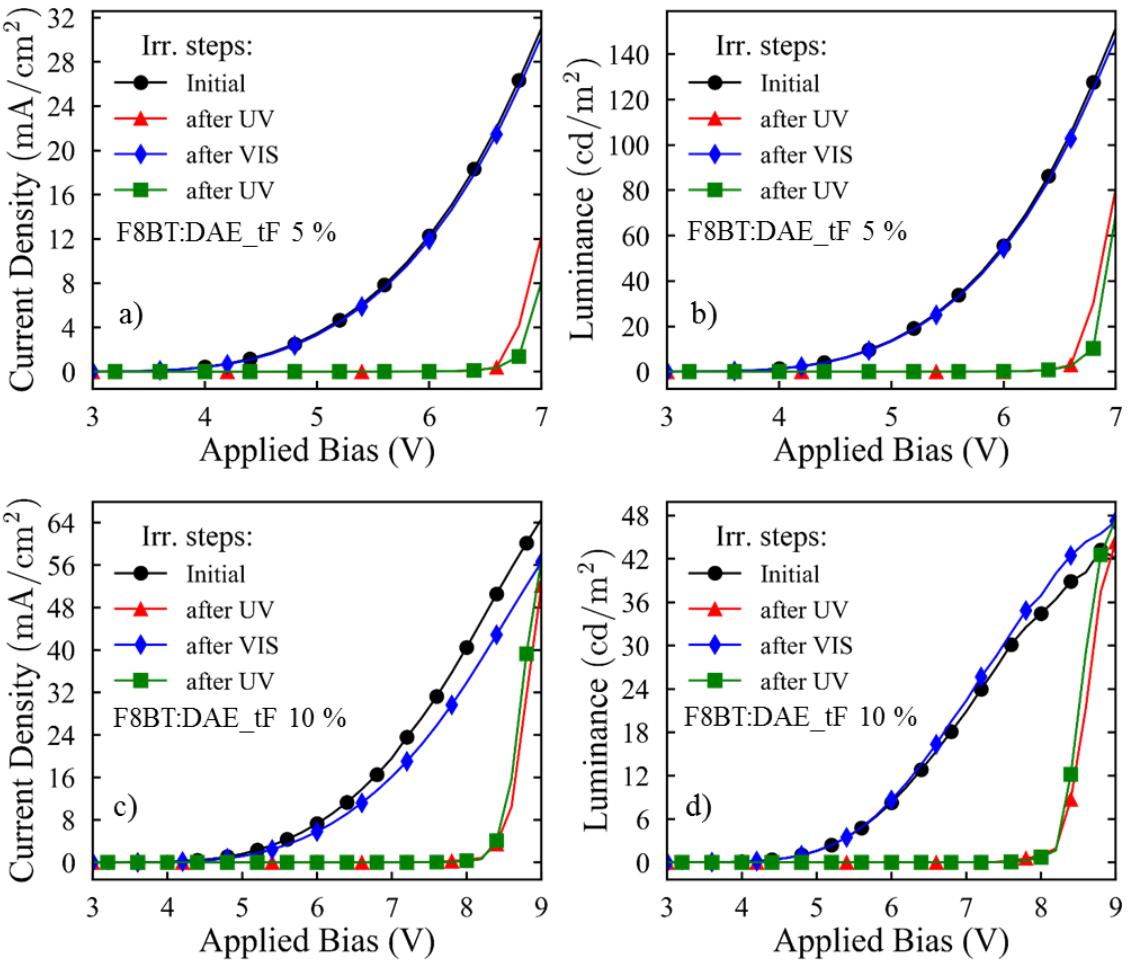

Figure 33: Effect of UV (315 nm, ~ 7 min) and VIS (528 nm, ~13 min) irradiation on OLEDs based on F8BT:DAE_tF 5 and 10 w/w % blends. Markers on selected data points as 'guides to the eye' only.

In particular, we observe an average increase of the reversible V_{ON} shift of 2.1 (± 0.2), 2.9 (± 0.2) and 3.7 (± 0.3) V for devices incorporating blends of F8BT:DAE_TF with loadings of 1, 5 and 10 w/w %, respectively (see Figure 34a, statistic over 4 irradiation cycles). We ascribe this phenomenon to the presence of an increasing concentration of switchable trap-states within our blends. Notably, the device performance is fully recovered after the exposure to the visible light. Indeed, such irradiation it is expected

restore the matrix charge transport properties as it switches the DAEs back to the open form, thus removes the charge trap-states from the host material bandgap. Interestingly, after UV irradiation, and upon relatively large applied bias, the current density and luminance values rise steeply to the values recorded after the VIS irradiation.

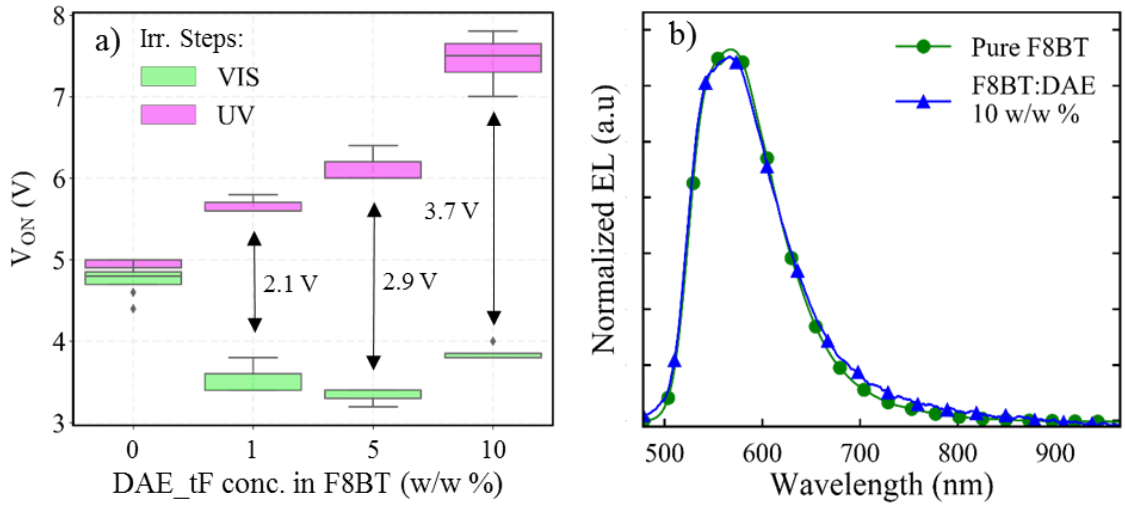

Figure 34: a) Statistics of the V_{ON} variation under UV and VIS light irradiation at different DAE concentrations, over 8 irradiation steps; b) overlap of normalized EL spectra of OLEDs based on neat F8BT and on the most concentrated blend. Markers on selected data points as 'guides to the eye' only.

We think that such a steep signal increase is the consequence of two factors. First, once the photo-generated traps are completely filled by charge carriers, the device is expected to quickly transit from the trap-filling regime to the space charge limited one (SCLC)[82]. Secondly, I observe that the device turn-on starts not uniformly on the emissive area. Indeed, it take place initially on a restricted device area and, straight after, it propagates over the entire emissive area. This rapid increment of the actual device emissive area, during the voltage scan, is mirrored in the extremely steep rise of device characteristics. Such devices were not optimized to achieve high performances (see the simple stack without any charge transport or blocking layers) and, more importantly, the necessity to

preserve them over multiple measuring and irradiation cycles lead us to limit the voltage scan for each characteristic to relatively low values, so our devices hardly reached the maximum external quantum efficiency. The average maximum EQE value of our devices, it is pretty similar among the different blends, 0.14 ± 0.03 %, with the exception of the most concentrated blend which showed a, markedly lower EQE of ~ 0.05 %, probably due to the excessive doping that might have hindered the charge transport within the polymeric matrix and enhanced exciton quenching phenomena. In Figure 34b, the normalized electroluminescence (EL) spectrum of the most concentrate blend is overlapped to the one collected from the device based on pure F8BT. As expected the F8BT emission (560 nm, peak) is not modified and no additional spectral features can be attributed to the photochromic molecule.

4.5 Single carrier devices embedding DAEs

While the results in section 4.4 show the possibility to control OSOLEDs devices via optical stimuli they do not provide detailed description of the trapping mechanism. Indeed, following our EML design (section 4.1), we expected to generate trap states for both negative and positive charge carriers. To prove experimentally our considerations we fabricated switchable single-carrier devices to decouple the effects of DAE-tF isomerization on holes and electrons. For these devices the blend with 10 w/w % loading of DAE-tF was selected as it gave the largest V_{ON} variation upon light irradiation for ambipolar devices.

4.5.1 Device design

Electron-only (e-only) devices were obtained depositing a semi-transparent layer of environmentally oxidized Al on the ITO anode, thus having the final architecture Al (15

nm)/EML (90 nm)/Ca (30nm)/Al (150 nm). Given the similar low work function (WF) of the electrodes, as oxygen lowers the Al work function down to ~ 3.4 eV [118], only electrons are favourably injected in the device and thus subjected to the optically switchable trapping process, see Figure 35a. Differently, in hole-only (h-only) devices, to avoid the injection of electrons, the standard Ca cathode has been replaced with Au, having a WF of ~ 5.1 eV, thus giving the final architecture ITO (150nm)/PEDOT:PSS (40nm)/EML/Au (150 nm).

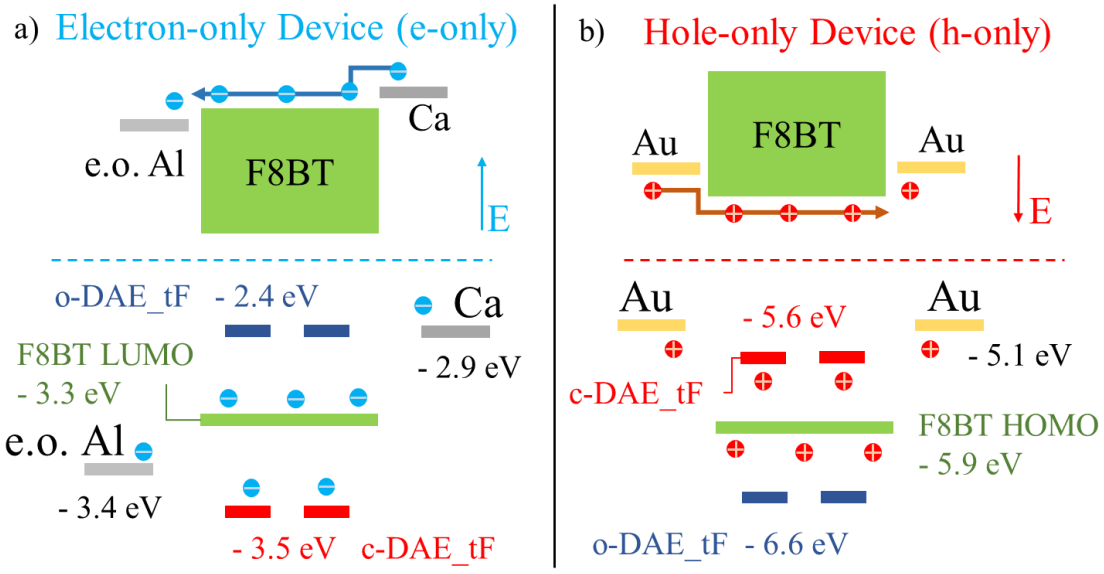

Figure 35: Single carrier devices, schematic of the symmetric contact design and charge transport. a) Electron-only device: top, F8BT LUMO – contacts WF alignment; bottom, optically switchable electrons trap states generation. b) Hole-only device: top, F8BT HOMO – contacts WF alignment; bottom, optically switchable holes trap states generation.

Here symmetric contacts create a ~ 1.8 eV energy barrier for the injection of electrons which ensures that only holes will flow through the device and interact with the photochromic dopant, see Figure 35b. It is worth to underline that such devices are not emissive in the voltage range investigated, which represent the confirmation of the unipolar nature of the electric characteristics collected.

4.5.2 Device performance under light irradiation

A comparison between the electric characteristics (as unipolar device are not emissive) of e- and h-only devices base on F8BT, neat and blended with DAE-tF respectively, is shown in Figure 36.

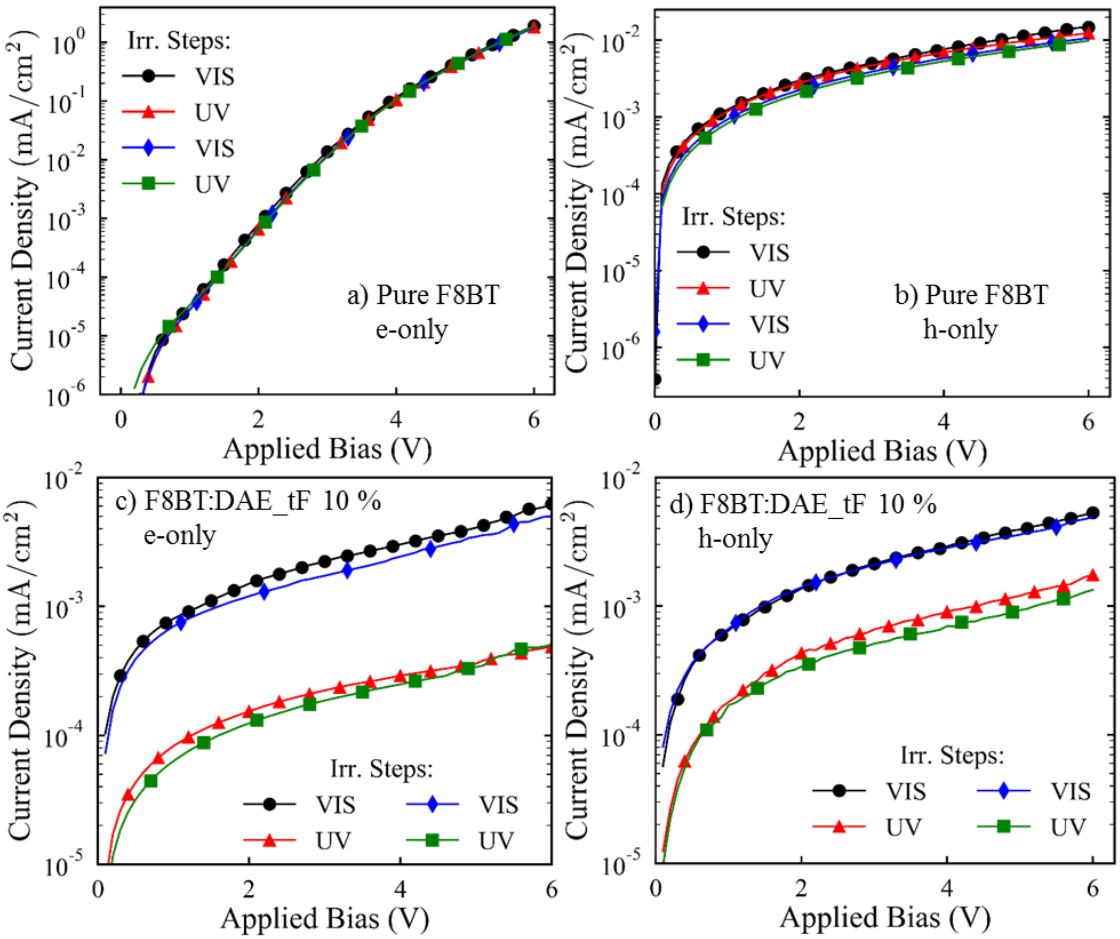

Figure 36: Single carrier devices performance under light irradiation. a,b) neat F8BT electron and hole-only, respectively; c, d) F8BT:DAE_tF 10 w/w % electron and hole-only, respectively. Markers on selected data points as 'guides to the eye' only.

For pristine F8BT, no change in the charge transport properties is detected following the light irradiation cycles neither for electrons nor holes, see Figure 36a-b. Interestingly, the maximum current density of electrons exceeds that of holes by two orders of magnitude. This behaviour can be explained by considering that in our device architectures, the

electrons are injected through an ohmic contact while holes through a rectifying one, see Figure 35. Blending DAE-tF with F8BT (10 w/w %) leads to a reduction of the maximum current density measured, regardless the light-irradiation. Notably, electrons transport appear to be particularly affected by the presence of the photochromic dopants. Here, the maximum current flowing in the e-only device, in presence of DAE-tF, drops by two orders of magnitude (evaluated at 5.0 V). Different is the situation for h-only devices where the addition of the dopant leads "only" to a ~ 50% reduction of the maximum current measured (evaluated at 5.0 V). The strong influence of trap-states on the electrons transport in organic semiconductors has been already reported in literature. Accordingly, our e-only device showed the largest photo-responsivity. Indeed, for these device, under UV and VIS light irradiation, we measured a current density variation more than twice larger than what observed for the h-only counterpart, see Figure 36 b-c.

4.6 Micro-OLEDs incorporating DAEs

4.6.1 Micro-electrodes engineering

For an OLED device, its dimension is unambiguously defined by the geometric overlap between anode and cathode electrodes. The fabrication of micro-structured switchable OLEDs (μ-OLEDs) compelled us to think about an efficient and cost effective route to miniaturize such electrodes. We decided to make use of the direct laser writing tool available at Scriba Nanotechnologie s.r.l. (Bologna, Italy) which allows the creation of micrometric patterns avoiding the tedious and time consuming steps typical of a photolithographic process. Furthermore, laser ablation can be used with a large varied of substrates and materials as it does not require specific chemical interactions or surface treatment. Indeed, here a high power IR pulsed laser (Nd:YAG, $\lambda = 1064$ nm) is focused

on the surface to achieve, locally, the direct sublimation of the target material allowing the straightforward creation of complex patterns in the micrometric range.

For the micro anode, we optimized the ablation process parameters in order to partially remove the conductive ITO layer from our substrates and obtain the designed pattern. Each anode pad, having an initial width of 1500 µm, was patterned into three parallel micro-stripes of ITO (Figure 37a), allowing us to drive and light-up three µ-OLEDs in parallel.

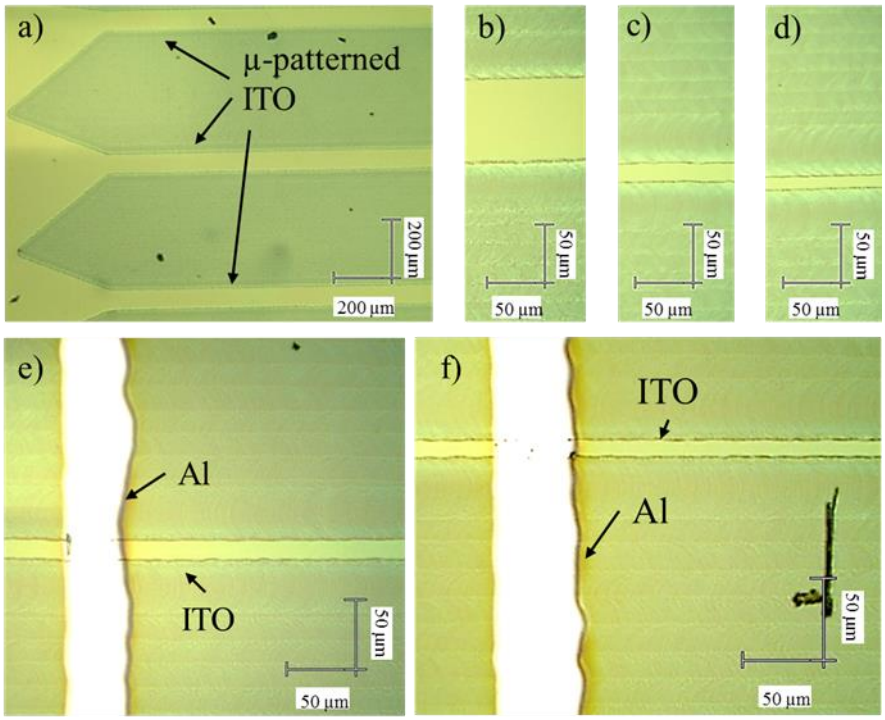

Figure 37: Microscopic OLEDs (µ-LEDs) fabrication: a) Macroscopic ITO pad patterned into three parallel micro-stripes via direct lithography (laser ablation), b) to d) ITO stripes of different width (70, 15 and 10 µm); e, f) µ-LEDs of ~ 500 µm^2 area.

This solution eased the detection of the device light output as intensity scales with the device area. Specifically, we tuned the direct lithography tool to create ITO stripes, having width of 70, 15 and 10 µm, see Figure 37 b, c and d, respectively. The same

equipment was used to cut a 100 µm thick nickel plate (see section 4.2.3) to generate shadow masks for the deposition of ~ 50 µm wide cathode electrodes, see Figure 37.

4.6.2 Device performances under irradiation

Microscopic OLEDs, with an active area of ~ 500 µm^2 see Figure 37e – f, incorporating the photochromic dopant (F8BT: DAE-tF 5 w/w %) were fabricated. In Figure 38 are shown the micrographs of the µ-devices in the OFF state (Figure 38a) and in the different brightness levels reached during a voltage scan (Figure 38b – d).

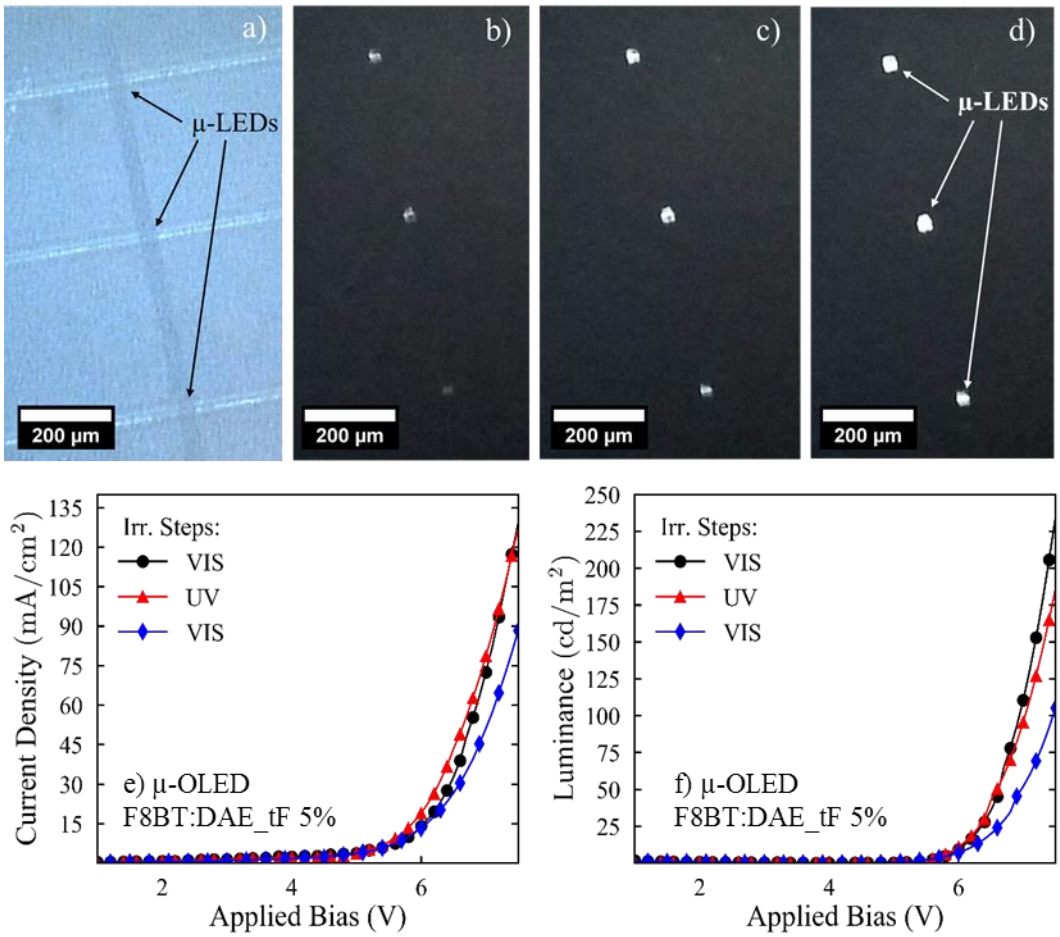

Figure 38: a) to d) µ-LEDs turning ON during a linear voltage scan; e, f) optically switchable µ-LEDs current density and luminance characteristics under UV and VIS irradiation. Markers on selected data points as 'guides to the eye' only.

While the analogous macroscopic device (emissive area of 4.5 mm^2, see section 4.4) clearly showed the impact of the DAE-tF isomerization on the optoelectronic performances, unexpectedly, µ-OLEDs were not light-responsive, as shown in Figure 38e-f. Here, the light irradiation does not induce any device V_{ON} variation, additionally the maximum luminance and current density steadily drop after each irradiation. We think that different aspects might have affected the µ-OLEDs light-responsivity. The large current density reached in our micrometric devices might have heavily degraded the DAEs (or favoured the formation of the not photochromic by-product), thus suppressing their light responsivity. Additionally, the characterization and irradiation of these micro devices, in a nitrogen filled glovebox resulted particularly challenging. This might have affected the accuracy of the irradiation and characterization procedure.

4.7 Conclusions

We successfully designed, fabricated and characterized stimuli-responsive OLEDs based on F8BT: DAE-tF blends. We firstly assessed the retained DAEs photochromic activity in the solid state via UV and PL spectroscopy measurement. Then, we demonstrated the ability of our devices to be optically controlled over light irradiation. We designed our emissive layer to allow the generation of optically switchable trap states for both holes and electrons achieving, in our best performing device, a maximum, reversible and optically induced, V_{ON} shift of 2.9 V with a maximum current density and luminance ON/OFF ratio of ~ 20 and ~ 90, respectively. Furthermore we proved the validity of our design strategy via the fabrication and characterization of light-responsive single carrier devices. Our data confirm that both the charge carriers are trapped when the DAE-tF is in its closed form. Electrons resulted more affected by the optically switchable trapping

process as the electrons current variation under light irradiation almost doubles the modulation observed for the positive carriers.

We also tested the fatigue resistance of our devices over four irradiation cycle, without observing significant performance degradation. Furthermore, we fabricated optoelectronic devices embedding switchable components having emitting area of ~ 500 μm^2. While the macroscopic devices showed a clear responsivity to the irradiation steps, our microscopic devices were unresponsive. We ascribe the loss of such ability to the higher current densities in our micro-sized devices which might have permanently degraded the photochromic dopant. In addition, the complexity of the characterization setup, together with our ability to measure three µ-devices in parallel, might have led to the inability to detect any photo-responsive behaviour. Further attempts to investigate the optical switchability of micron-sized emitting devices, light-emitting transistors (OLETs), is reported in section 5

5 Optically Switchable Light-emitting Transistors (OSOLETs)

Recently it has been demonstrated that it is possible to fabricate optically switchable multifunctional OTFT and OLEDs blending organic semiconductors with photochromic diarylethenes, see section 2.5.3.2. Organic light-emitting transistors (OLETs) combine the electrical behaviour of OTFTs with the electroluminescence emission typically seen in OLEDs, see section 2.4. Here, for the first time, we have fabricated optically switchable organic light-emitting transistors (OSOLETs), with channel length of 2.5 μm, through a judicious combination of light-emitting semiconductors and photochromic molecules. The irradiation of the solution-processed films with specific wavelengths enables the efficient and reversible tuning of charge transport and electroluminescence simultaneously, with a degree of modulation up to an on/off ratio of 500, in the three primary colours. Different emitting micro-patterns can be written and erased, through a non-invasive and mask-free process, in a single OSOLET, thereby making our devices of interest for optically gated highly-integrated full-colour displays and active optical memory technologies.

Diarylethenes derivatives were received form by Dr. Martin Herder from Prof. Stefan Hecht's group (Humboldt University of Berlin). OLETs were received from Dr. Lili Hou from Prof. Paolo Samorí's group (University of Strasbourg). At UCL, I worked on the design and realization of a specifically designed set-up and data elaboration routines for the characterization of the devices light-responsive optoelectronic properties.

5.1 Active layer design: materials selection

Three commercially-available semiconducting light-emitting polymers poly(9,9-dioctylfluorene-alt-bithiophene) (F8T2), poly[2-methoxy-5-(3',7'-dimethyloctyloxy)-para-phenylenevinylene] (MDMO-PPV), and poly(9,9-dioctylfluorene) (F8) were used to fabricate OLETs having fluorescence emission ranging from blue to red (Figure 39a), thus covering the entire visible spectrum (Figure 40c-e). In view of the different HOMO levels energy for the three polymers, three different DAEs derivatives, namely DAE_tBu and DAE_F, were chosen to generate the switchable trap states for positive charge carriers. In Figure 39b it is shown the energetics, limited to the HOMO levels of three different blends investigated.

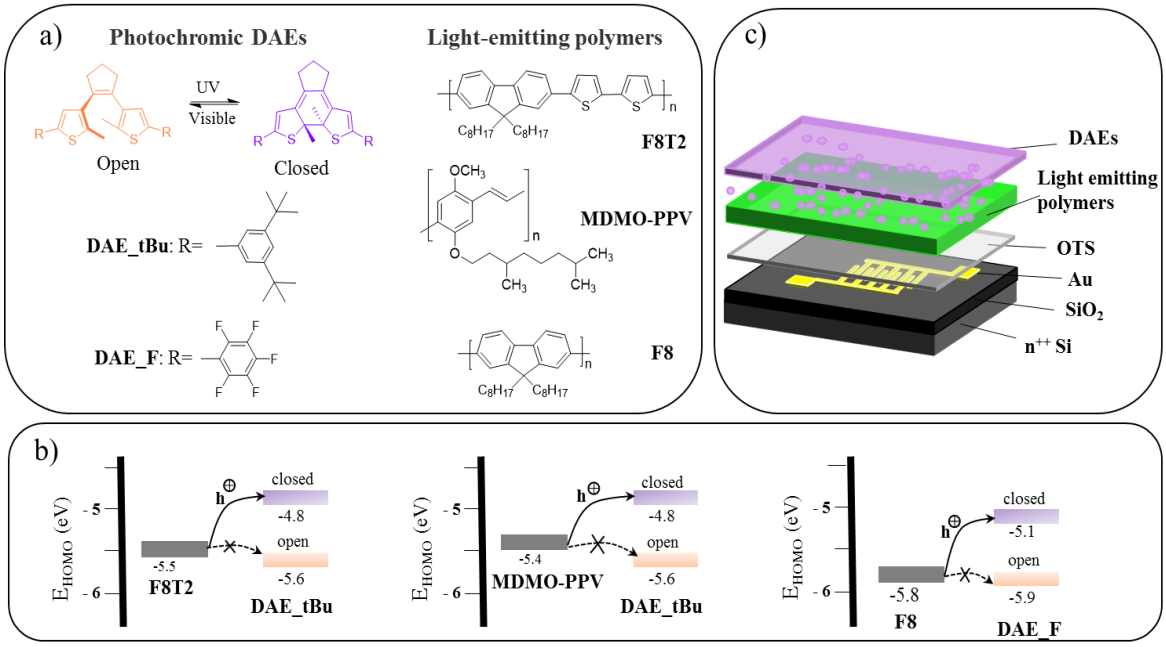

Figure 39: Molecules, energetics, and device structure of OSOLETs. a) Chemical structures of diarylethenes derivatives (DAE_tBu and DAE_F) and light-emitting polymers (green: F8T2; red: MDMO-PPV; blue: F8). b) Energetics of the blends investigated and the switchable charge trapping mechanism based on the variation of the DAEs HOMO energy levels. c) OLET device structure (only the blend composition is changed among the samples investigated). Revised from [119]

Here, the values associated to the DAEs HOMO levels have been confirmed in previous studies [105], [117], [120] while cyclic voltammetry (CV) measurements were carried out by our partner, at University of Strasbourg, to determine the molecular frontier levels of the emitting polymers. When the DAEs are in the open forms, their HOMO levels lay at higher energies (with a gap of ~ 100 and 200 meV) than the polymers frontier levels. Conversely, after UV irradiation, the HOMO levels of the DAEs closed isomers are shifted to energies that are ~ 600 meV lower compared to the polymers HOMO levels, thus providing the opportunity for a marked holes trapping. The OSOLETs were fabricated in a bottom-gate bottom-contact configuration with SiO_2/Si as substrates and the pre-patterned gold interdigitated electrodes as source and drain contacts, see Figure 39c.

5.2 Experimental details

5.2.1 Materials and characterization

Butyl acetate, p-xylene, and ethyl acetate were used without any further purification. MDMO-PPV, (Sigma-Aldrich), F8, (Sigma-Aldrich), and (F8T2, Ossila) were used as received. The synthesis, photochemistry in solution and energy levels determination of DAE_tBu and DAE_F were previously reported [105], [117], [120] . UV/visible absorption spectra were collected on a JASCO 650 spectrometer under ambient conditions. Photoluminescence spectra were measured on a Cary Eclipse fluorescence spectrophotometer under ambient conditions. AFM images were recorded using a Nanoscope (Veeco Multimode V) in tapping mode in air.

For UV/VIS absorption and PL spectroscopies, UV light irradiation was carried out using an analysis lamp (312 nm, 6 W, Herolab) for 20 s, and visible light irradiation was

performed using a white lamp (Dolan-Jenner MI-150 Illuminator) coupled with a long pass filter (> 520 nm) for 30 s. The patterned images of the OLETs were created by using a focused laser (focus ca. 2 μm^2, 532 nm, 60 mW cm^{-2}), and the writing process was controlled under a microscope with a 50× objective on a Renishaw 1000 Raman setup.

5.2.2 Device fabrication and characterization

OLETs were fabricated as described in section 3.2.3.1. The light responsive emissive layers were deposited as follows.

The green emitting layer was spun from a 10 mg/mL solution of F8T2 in anhydrous p-xylene, the thickness was ~ 80 nm. The device was annealed at 170 ℃ for 20 min. DAE_tBu was dissolved in anhydrous n-butyl acetate at a concentration of 1 mg/mL, and spun on top of the F8T2 film. The samples were annealed at 80 ℃ for 1 h to allow the diffusion of DAE molecules into F8T2 matrix.

The red emitting layer was spun from an 8 mg/ml solution of MDMO-PPV in anhydrous p-xylene, and the thickness was ~ 80 nm. The device was annealed at 170 ℃ for 20 min. DAE_tBu was dissolved in anhydrous n-butyl acetate at a concentration of 1 mg/mL, and spun on top of the MDMO-PPV film. Subsequent annealing was applied at 80 ℃ for 1 h to allow the diffusion of DAE molecules into MDMO-PPV matrix.

The blue emitting layer was spun from a 20 mg/mL solution of F8 in anhydrous p-xylene, and the thickness was ~ 100 nm. The device was briefly annealed at 170 ℃ for 2 min. DAE_F was dissolved in anhydrous ethyl acetate with the concentration of 2 mg/mL, and spun on top of the F8 film. Subsequent annealing at 40 ℃ for 1.5 h was applied to allow the diffusion of DAE molecules into F8 matrix.

The neat light-emitting polymers based OLETs were prepared using the same method as described above without deposition of DAEs. OSOLETs were characterized as described

in section 3.2.3.2. The irradiation on the OSOLETs was carried out inside the glovebox, in N_2 atmosphere. A UV LED (Thorlabs LED315W, 0.6 mW, 315 nm, FWHM = 10 nm) and a green LED (Thorlabs LED528EHP, 7 mW, 528 nm, FWHM = 35 nm) were used. In general, the PSS was reached under UV irradiation for 10 mins and recovery within 90 s under visible light. The EL images were recorded on a microscope (Leica S6D) with a charge coupled device (CCD) colour camera.

5.3 Blends characterization

5.3.1 DAEs switchability in the solid state

We assessed the retained photochromic properties of DAEs in the solid state, DAE_tBu and DAE_F were dissolved in anhydrous ethyl acetate (concentration of 1 mg/ml and 2 mg/ml, respectively) and subsequently spin-coated on quartz substrates. The reversible formation of the two DAE isomers in the solid state was confirmed collecting the films absorption spectra after UV (312 nm) and VIS (530 nm) light irradiation, see Figure 40a, b. For each blend, in the solid state, we investigated also the impact of the DAE photo-switching on the fluorescence spectrum on the emissive matrix, see Figure 40. We observed a reduction of the PL intensity of F8T2/DAE_tBu, MDMO-PPV/DAE_tBu and F8/DAE_F after UV irradiation. The ratio of PL peak intensity before and after UV irradiation was 1/0.63, 1/0.68 and 1/0.97, respectively. Such variation seems to be consistent with the integral of the spectral overlap between absorption spectra of DAEs, in the closed form, and the PL spectra of the emitting polymers. The following irradiation with visible light increases, as expected, the PL intensity.

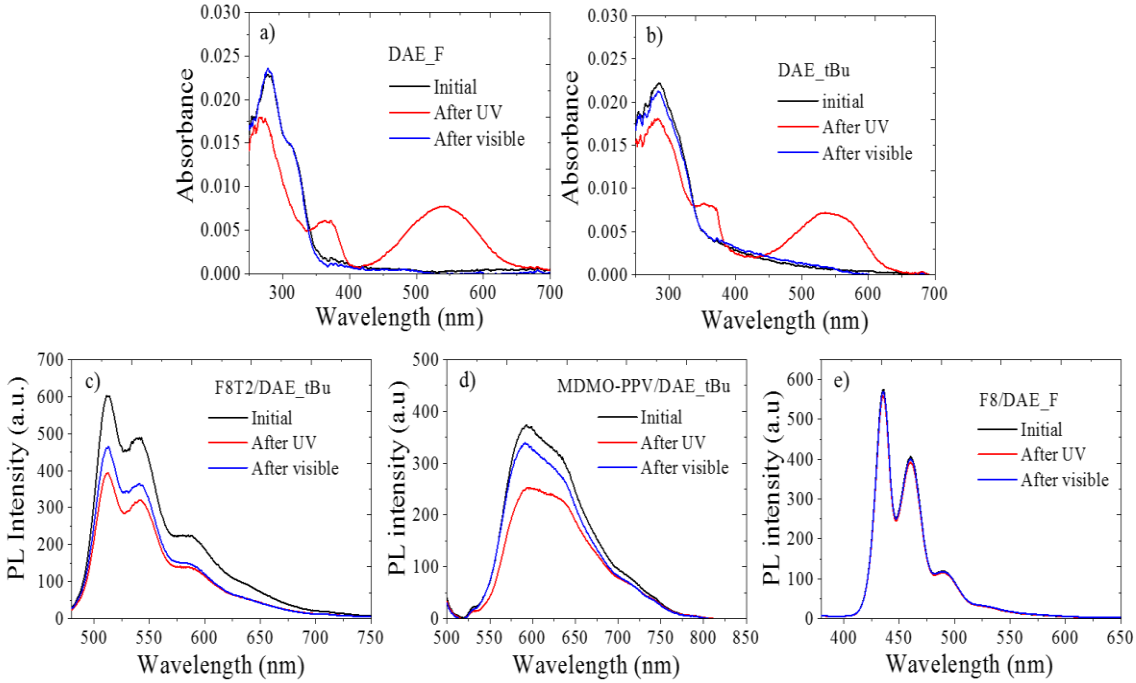

Figure 40: UV/VIS absorption spectra of the films of a) DAE_tBu, and b) DAE_F after UV (312 nm) and visible irradiation (> 520 nm). PL spectra of the films of c) F8T2/DAE_tBu, d) MDMO-PPV/DAE_tBu, e) F8/DAE_F, and their response after UV and visible light irradiation. The films of light-emitting polymer/DAE were prepared on quartz substrates using the same condition and procedure as the fabrication of OSOLETs. Adapted from [119].

The non-complete recovery of PL intensity can be ascribed by the degradation of the emitting polymers under irradiation in ambient conditions.

5.3.2 Morphology: atomic force microscopy

In Figure 41 is reported the AFM investigation on our blends. The infiltration of DAE_tBu via our permeation process did not modify the F8T2 morphology nor cause phase segregation. In case of MDMO-PPV, only minor surface roughness variations were detected between pristine and doped polymer. However, the exposure of neat F8 to ethyl acetate (bad solvent for F8) and to the successive thermal treatment, not only enhance diffusion of DAE_F into the polymeric matrix, but it markedly promotes the formation of supramolecular structures (such as the crystalline phase [121] and the conformational

isomer β-phase [122]) of F8, which aggregate in micron-sized clusters resulting in a marked increase of surface roughness (from Rrms = 3.0 nm for the neat F8 film to Rrms = 12.3 nm for the F8/DAE_F film) [123].

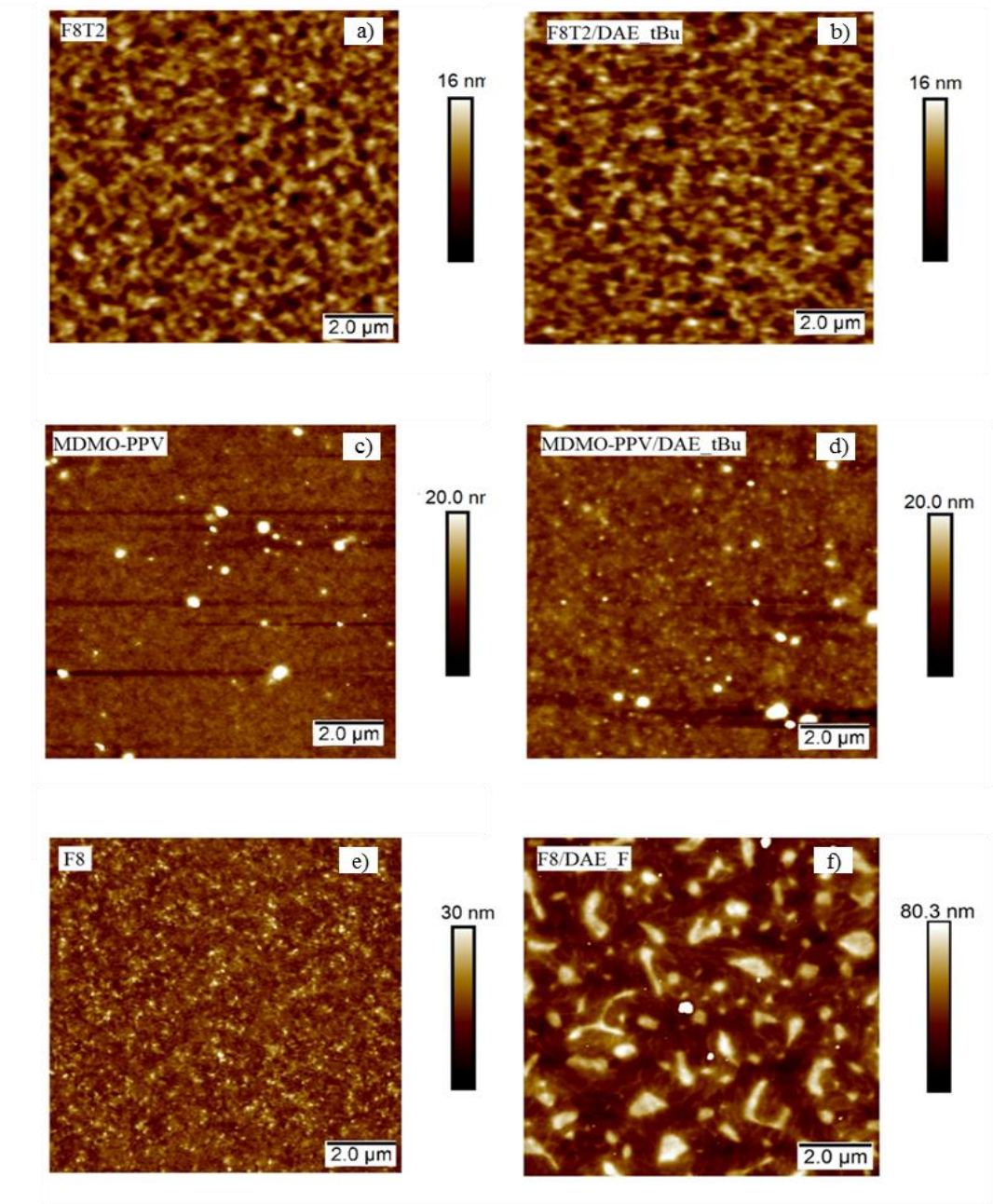

Figure 41: AFM images of the film of a) neat F8T2, b) F8T2/DAE_tBu, c) neat MDMO-PPV, d) MDMO-PPV/DAE_tBu, e) neat F8, and f) F8/DAE_F. Reproduced from [119].

5.4 OLETs performances under light irradiation and optical patterning

The optoelectronic performance of our OSOLETs under visible and UV irradiation was measured in nitrogen atmosphere via a specifically designed setup, see section 3.2.3.2. The devices were characterized via a transfer characteristics, the results are shown Figure 42.

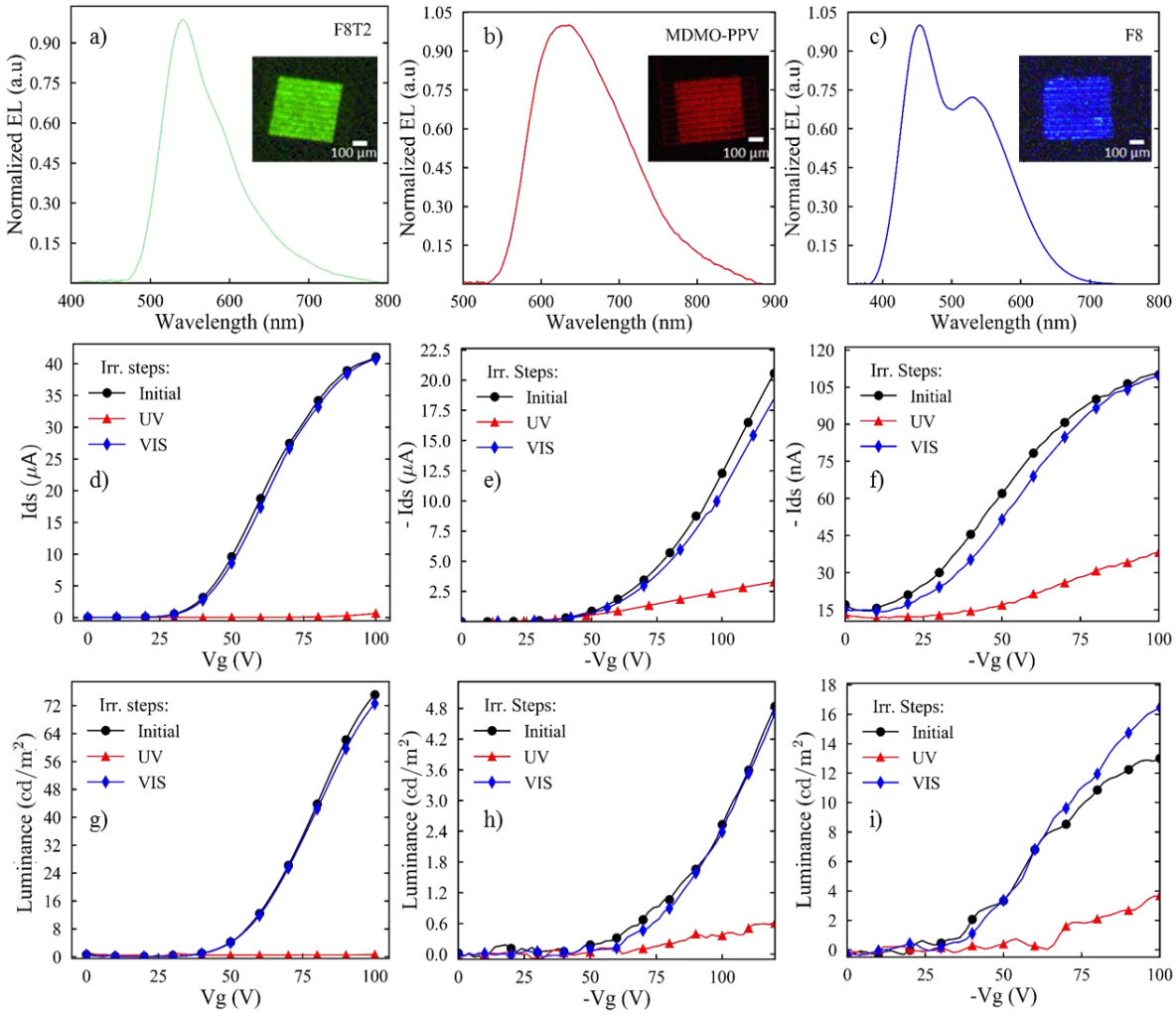

Figure 42: OSOLETs EL spectra, optical micrographs, and optoelectronic characteristics. a) to c) EL spectra and optical images of OSOLETs based on F8T2/DAE_tBu, MDMO-PPV/DAE_tBu and F8/DAE_F blends. d) to f), transfer characteristics, and optical output (g to i), of OSOLETs based on F8T2/DAE_tBu (V_D = -100 V), MDMO-PPV/DAE_tBu (V_D = -120 V) and F8/DAE_F (V_D = -100 V) after UV and visible light irradiation. Revised from [119]*. Markers on selected data points as 'guides to the eye' only.*

In our devices the emitting area is the TFT channel, 2.5 µm long and 1 cm wide, as shown in the inset of the graphs in Figure 42a-c. Electroluminescence peaks are at 540 nm (FWHM = 90 nm), 630 nm (FWHM = 143 nm), for the green and red-emitting OLETs, respectively. The blue emitting device, shows a broader electroluminescence spectrum, featuring two emission bands peaked at ~450 nm and ~ 550 nm. The first, dominant, is attributed to the F8 emission, differently, the green signal is commonly detected in F8 based optoelectronic devices, it is ascribed to inter-chain states and/or fluorenone defects [12], [124], [125]. Notably, the emission of our light-responsive OLETs cover well the whole visible region (400-700 nm).

Although light emission requires ambipolar injection, most of the charge transport in our OSOLETs can be described as essentially unipolar. Indeed, we measure a dependence of the drain current on the applied V_{GS} which is in line with previous literature on non-switchable OLETs [126]–[128],where the negative V_{GS} accumulates holes within the device channel. Nevertheless, the light emission provides evidence for electron injection and diffusion for several nm inside the channel.

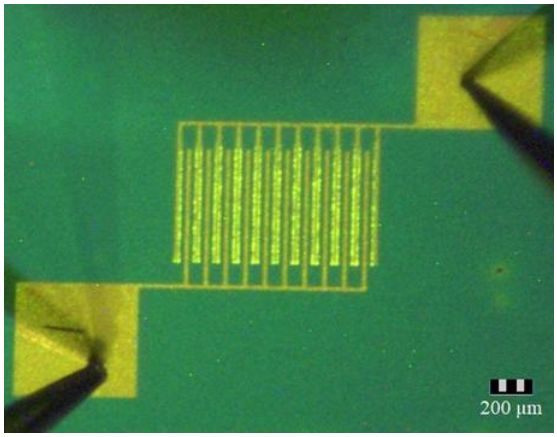

Figure 43: Micrograph of a F8T2 based OLET with channel length (L) of 20 µm. The image shows the luminescence in the proximity of the drain electrode from which electrons are injected. Reproduced from [119].

In Figure 43, we report the micrograph of an F8T2 based OLET with a larger channel length (20 μm), where is it clearly visible that the device electroluminescence is generated only in the proximity of the drain electrode, demonstrating that electrons, minority carriers, undergo radiative recombination near the injection zone. However, given the limited resolution of our camera and the narrow channel length (2.5 μm) of our OSOLETs, we observed light emission over the whole channel area, as shown in the optical image in Figure 42a-c. In addition, considering the LUMO levels of selected semiconductors (F8T2 = -3.1 eV, MDMO-PPV = -3.3 eV, F8 = -2.8 eV) and photochromic compounds (DAE_tBu: open > -2.0, close = -2.5 eV; DAE_F: open = -2.0 eV, close = -2.9 eV) we can expect that no or negligible (in case of F8) trapping action affects the negative carriers. Initially, we focus our analysis on the device performance, without considering the photo-responsive behaviour. The transfer characteristics of green, red, and blue OSOLETs reported in Figure 42d-f. The device holes motilities were calculated, as reported in section 3.2.3.2, when the DAEs were in their open form and gave the values of ~ 1.5×10^{-3}, 1×10^{-4}, and 5×10^{-7} $cm^2\ V^{-1}s^{-1}$, respectively. For the sake of comparison, we extrapolated for the pristine green-, red-, and blue-emitting OLETs mobility of ~ 5×10^{-3}, 2.0×10^{-4}, and 8×10^{-5} $cm^2\ V^{-1}s^{-1}$, respectively. In case of F8T2 and MDMO-PPV we observe a reduction of mobility which can be ascribed to the scattering (and/or residual trapping) induced by the DAEs blended in the polymeric matrix. However, the mobility in the blue OSOLETs with DAE_F in its open isomer drops by two orders of magnitude with respect to the one based on the neat polymer. Here, domain boundaries and disordered interphase regions in the F8/DAE_F bicomponent film, see section 5.3.2, hinder the charge transport through the active layer [129]. The luminance of the OSOLETs is reported in Figure 43g-i, and it follows the trend observed for the drain current. In terms of electroluminescent intensity, OLETs based on pristine F8T2 and MDMO-PPV (reference devices) outperform the

analogous devices based on the photochromic blends, see Figure 44. Interestingly, the opposite situation is observed in case of F8. Here, the doped device (F8/DAE_F), despite the reduction of the output current with respect to the reference device, shows an increase of luminance, which can be ascribed to the higher PL efficiency (PLQY) of F8 in the so-called β-phase as already reported by Perevedentsev and Hsu et al [122], [130]. Therefore, F8T2 and MDMO-PPV based OLETs exhibit a minor variation of EQE, between reference and switchable devices (EQE at Vg = –80 V: MDMO-PPV 2×10^{-3} %, MDMO_PPV/DAE_tBu 6×10^{-3} %, F8T2 0.4×10^{-2} %, and F8T2/DAE_tBu 1.0×10^{-2} %). However, the formation of F8 β-phase leads to a remarkable increase of the EQE (again at Vg = –80 V) of the F8/DAE_F bicomponent device (1.2 %) compared to the F8 reference device (1.2×10^{-2} %). Although the controlled formation of the β-phase of F8 via dipping in solvent/non-solvent mixtures has already been exploited to improve the EQE of F8-based OLEDs [131], no similar investigation has been reported on OLETs yet. Considering the device light-responsivity, we can clearly observe that the irradiation of our OSOLETs with UV light (315 nm, 0.6 mW) induces a remarkable decrease of both drain current and luminance, which we attribute to the ring-closing isomerization of the DAEs and subsequent efficient trapping of the majority of carriers. The best switching performance is measured for devices based on the F8T2/DAE_tBu blend, here the on/off ratios (the ratio of the current/luminance in the initial state and after UV irradiation) in both drain current (ISD) and EL exceed 500 (see Figure 42d, g). Such a large degree of modulation is comparable with the reports of photo-programmable OLEDs and non-volatile organic memories [110], [132]. A marked modulation of the drain current and luminance was also observed for MDMO-PPV/DAE_tBu OSOLET devices (85 % decrease in current and 87 % decrease in luminance, at Vg = –120 V, see Figure 42e, h) as well as for F8/DAE_F OSOLET devices (65 % decrease in current and 75 % decrease

in luminance, at Vg = –100 V, see Figure 42f, i). Importantly, the exposure of our devices to green (528 nm) light converts the DAEs back to their open form, leading to the full recovery of the initial OSOLET state. Under the same irradiation conditions, OLETs based on neat polymers did not show any modulation of output current and EL (see Figure 44).

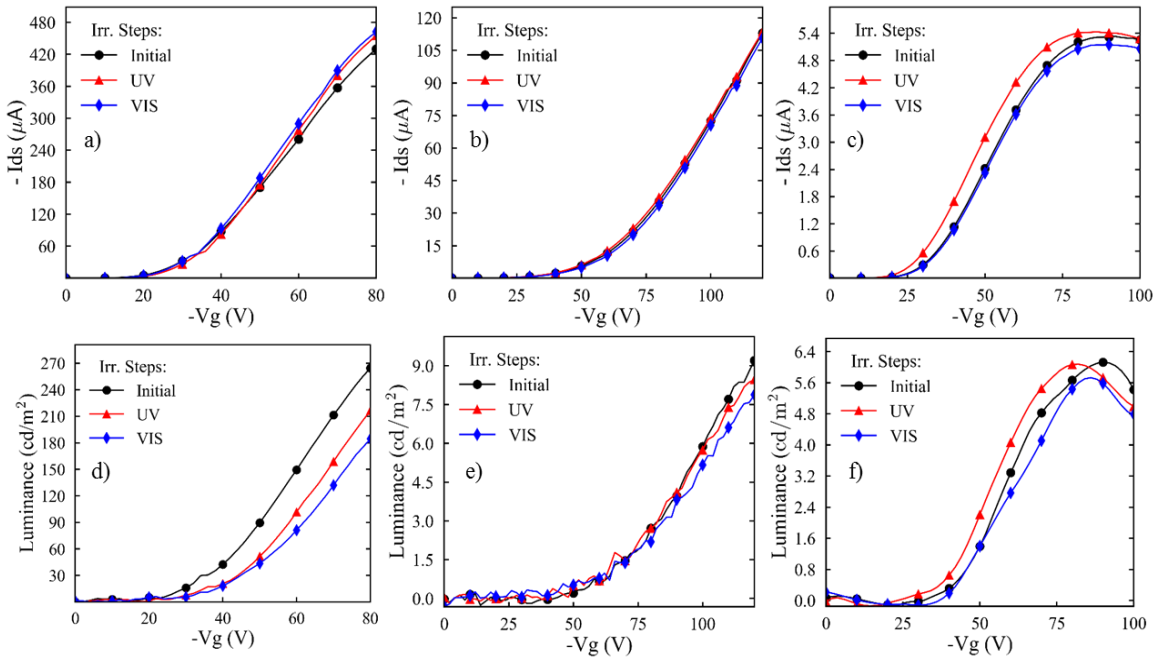

Figure 44: Transfer and luminance characteristics under UV and visible irradiation of a), b) neat F8T2 OLET at drain voltage –100 V, c), d) MDMO-PPV OLET at drain voltage –120 V, and e), f) F8 OLET at drain voltage –100 V. Markers on selected data points as 'guides to the eye' only.

It should be noted that the energy transfer from the light-emitting polymers to DAEs in their closed form, favoured by the spectral overlap of the emission of the polymers with the absorption of the DAEs in ring-closed form, can also contribute to the modulation of the intensity of the emitted light. The effect of DAEs photo-switching on both transfer current and luminance of the OSOLETs was monitored over three cycles alternating UV and visible irradiation (Figure 45). The optical modulation of both maximum drain current and luminance of the three-color OSOLETs, normalized to the initial value for

each measurement, is reversible and stable over several cycles. More importantly, since light is used as an external control of our OSOLETs, it is possible to generate emitting patterns with high spatial and temporal resolution on a single transistor as demonstrated by optical images of patterns created and erased in a single OSOLET (Figure 46). In the initial configuration, the F8T2/DAE_tBu OSOLET was in an all light-emitting on state (Figure 46a).

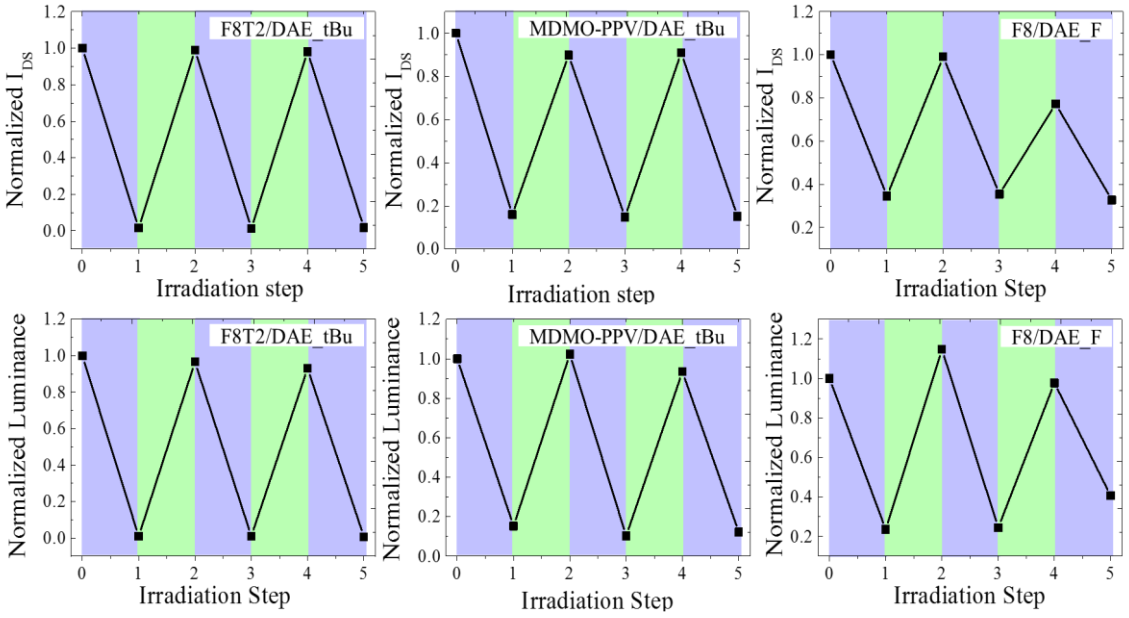

Figure 45: Reversible modulation of OSOLETs' current and luminance over three irradiation cycles with UV light (315 nm, 0.6 mW, 10 min, violet shaded areas) and visible green light (528 nm, 7 mW, 90 s, green shaded areas). All values are normalized to initial value before any irradiation and the connecting lines serve as 'guides to the eye'. Revised from [119].

Then, the device was irradiated homogenously using UV light leading to an all-dark state (Figure 46b). Using a focused green laser (532 nm) we can form patterns on the OSOLET with the aid of a microscope. Figure 46c shows a light-emitting on area with a 'H' shaped pattern on the same device. Subsequently, the irradiation of the entire device with green light erased the patterns and the all light-on state is restored (Figure 46d). The second pattern can be written in the same pixel with another step of UV irradiation and followed

by one more laser writing step. Figure 46f exhibits a pattern image of an array of dots, obtained in the same device area, demonstrating the reversible and repeatable patterning of the emissive area up to micron/sub-micron scale.

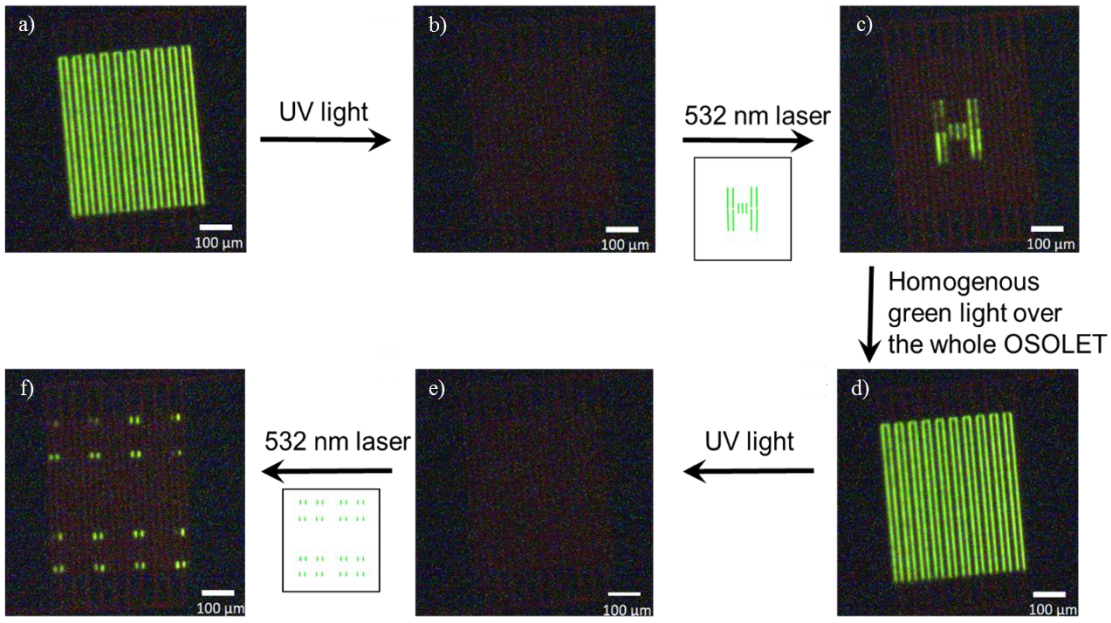

Figure 46: Emitting pattern created and erased within a single OSOLET, performed at Strasbourg University. a) Optical image of a F8T2/DAE_tBu OSOLET device biased with Vd = Vg = –100 V. b) Optical image of a dark state in the same device after UV irradiation. c) Optical image of an 'H' shape emitting pattern 'written' focused green laser. d) Optical image of the device after uniform green light irradiation. Steps b) and c) are repeated to achieve the pattern f). The darker areas of the patterns are due to the variation of the intensity and/or focus of the laser.

5.5 Conclusions

We realized and characterized a novel OLET device in which the charge transport and electroluminescence, in the range of the three primary colours, can be switched effectively and reversibly using light as an external stimulus. The active layer in such optically switchable organic light-emitting transistor (OSOLET) comprises an organic

light-emitting semiconductor and a photochromic DAE derivative. The photo-tunable HOMO-LUMO energy levels of DAEs can either transport or trap the charge carriers, toggled by UV and visible light irradiation. Such a dual external control is achieved through the engineering of the energy levels of the light-emitting polymers and those of the DAEs isomers. We demonstrate also the possibility to write and erase emitting patterns in a single OSOLET through a non-invasive and mask-free process, with a spatial resolution of a few micrometres. The stimuli-responsive multifunctional devices proposed in this work are all readily fabricated via solution processing, thus potentially transferrable to roll-to-roll compatible or ink-jet printing lines to produce low-cost and flexible stimuli-responsive (nano)electronics on a large scale. Ink-jet printing appears being a most suitable deposition method to fabricate full colour displays. In principle, light emission from OLETs in any region of the visible spectrum can be tuned by choosing appropriate photochromic molecules in combination with suitable light-emitting polymers. Future efforts will be directed towards optically switchable OLETs that can be operated at a lower driving power/voltage and yield stronger brightness and a higher ON/OFF ratio. A lowering of the operating voltage and enhancement of the brightness can be achieved via the careful selection of (i) the light-emitting materials, which should possess high charge carrier mobility and PL efficiencies, (ii) the optimal devices structures, with a shorter channel length, and (iii) the adoption of non-symmetric electrodes which should favour the injection of both charge carriers [95], [133]. Our approach opens intriguing perspectives towards the development of novel optically gated, integrated full-colour displays, micro-sized light sensors, active optical memories and logic circuitries.

6 Red-emitting LEDs based on graphene quantum dots

In this chapter is described the application of bottom-up synthetized, red-emitting, graphene quantum dots (GQDs), namely dibenzo[hi,st]ovalene derivatives (DBOV), in light-emitting diodes (LEDs). Differently from devices based on top-down synthesized GQDs, my LEDs show voltage-independent electroluminescence and colour purity comparable with inorganic Cd-based quantum dot LEDs. To prevent concentration quenching we blended our GQDs with F8BT. The same blends used for the device fabrication were morphologically investigated via AFM and optically characterized via absorption (also transient absorption) and fluorescence (also time-resolved) spectroscopy. Bottom-up synthesized atomically precise GQDs (with HOMO and LUMO levels measured via cyclic voltammetry) were received form Dr. Akimitsu Narita from Prof. Klaus Müllen's group (Max Planck Institute for Polymer Research). Ultrafast transient absorption spectroscopy measurements were performed at Italian Institute of Technology (IIT) in Milan by Dr Giuseppe Paternó from prof. Scotognella's group. Blends characterization, device design, fabrication and characterization were carried out at UCL.

6.1 Emissive layer design

GQDs were blended with a conjugated emitting polymer as the host-guest nature of the emissive layer reduces impact of the PL concentration quenching [134], [135]. As host material F8BT was selected, known as a potent host material for NIR OLEDs [136], [137], especially in view of the good spectral overlap between the host emission (peaked at 560 nm) the DBOV absorption spectrum, a key prerequisite to reach efficient host-guest energy transfer [138] (Figure 47a). Further desirable features of our host material are the ability to transport electrons efficiently [84] and undergo both triplet-triplet annihilation (TTA) and thermally activated delayed fluorescence (TADF) [139]. These properties are expected to improve both the charge carriers balance and the host-guest energy transfer in our devices emissive layer [139]–[141]. In addition F8BT and DBOV form a type I heterojunction given that F8BT's and DBOV LUMO level is found at ~3.3 ± 0.1 eV and 3.2 ± 0.1 eV below vacuum respectively, whereas their HOMO is found at ~ 5.9 ± 0.1 eV and 4 .8 ± 0.1 eV, below vacuum respectively.

6.2 Experimental details

6.2.1 Thin film deposition and device fabrication

Fused silica and ITO-coated glass substrates (Ossila, 20 Ω/square) were cleaned as described in section 3.2.2.1. In a N_2 glovebox, F8BT (Ossila, M_w < 250000 g/mol) and DBOV were dissolved in anhydrous toluene (10 mg/ml), left stirring overnight, filtered via a PTFE filter (pores of 0.2 μm) and then used to obtain solutions having F8BT:DBOV 0.5, 1, 2.5 and 5 w/w % concentration. After further 3 hrs of stirring, F8BT and blends solutions were spin-coated (1200 rpm, thickness of ~ 100 nm) on fused silica substrates for optical and morphological investigations. Film thicknesses were measured using a

Dektak stylus profilometer. Surface morphology investigation of the blends under study has been performed in air via AFM (Bruker Dimension Icon – PeakForce tapping mode) on an area of 500 nm^2.

The blends were used in OLEDs, fabricated and characterized as described in section 3.2.2.

6.2.2 Thin film optical characterization

PL spectra of F8BT:DVOB blends, 0.5, 1, 2.5 and 5 w/w % thin films (spin casted on fused silica substrates) and DBOV in dry toluene were measured in air, at room temperature, excited via a 450 nm (528 nm for DBOV in solution) laser diode module (average power <1 mW, collimated beam) and collected with an ANDOR-Shamrock 163 spectrometer coupled with an ANDOR-Newton charge-coupled device (CCD) unit. The absolute PLQY of thin films and pure DBOV solution, was measured using an integrating sphere. Time resolved fluorescence decay were collected via the spectrometer Lifespec II (Edinburgh Instruments). Lifetimes (τ) were obtained through a reconvolutive bi-exponential global fitting algorithm applied simultaneously to the PL decays (both at 630 nm and 750 nm) of all our blends.

6.3 Steady state and time-resolved PL

Thin film samples of F8BT: DBOV blends with 0.5, 1, 2.5 and 5 w/w % GQDs loadings were spin-coated on fused silica substrates, from solutions in anhydrous toluene, to a thickness of ~100 nm.

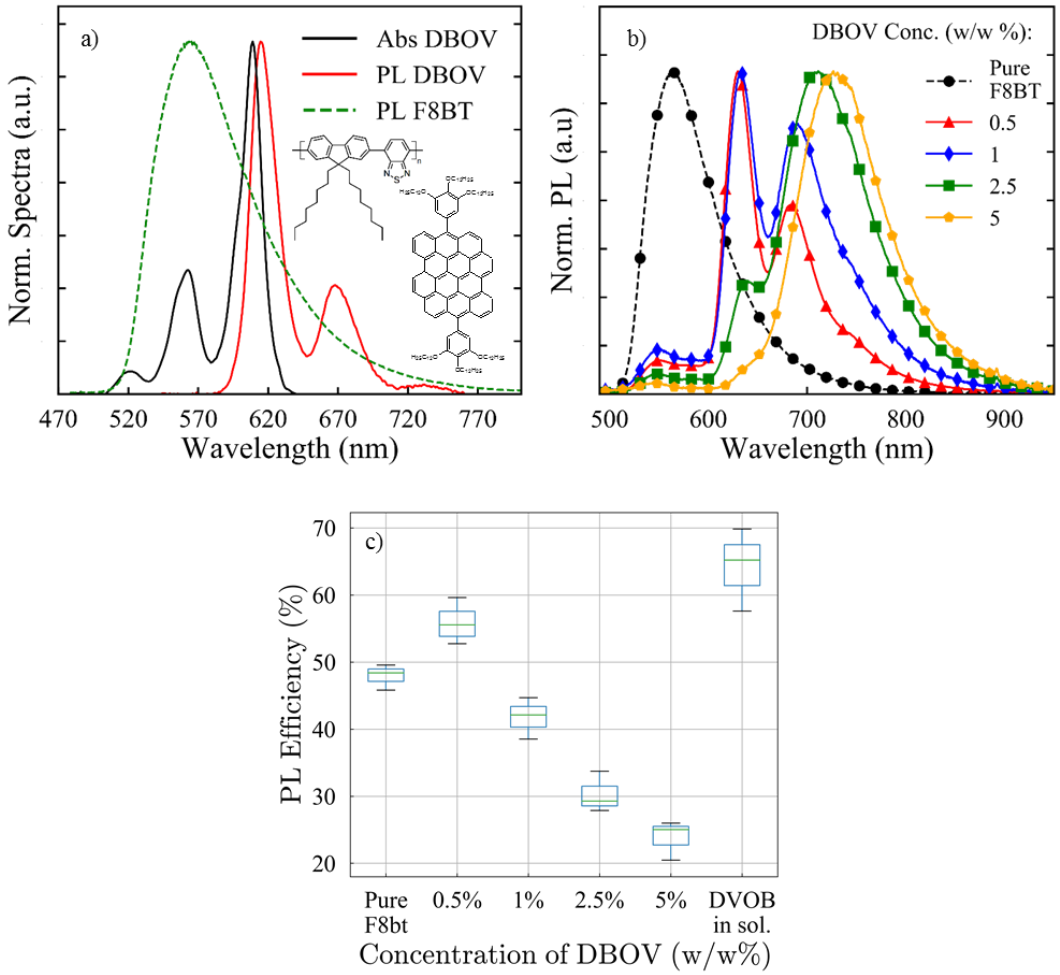

Figure 47: a) Absorption and PL spectra of DBOV (1.3 10^{-6} M in dry toluene), PL spectrum of F8BT (in solid state).inset: chemical structure of F8BT and DBOV. b) PL spectra of F8BT: DBOV blends in the solid state. Statistics over 5 absolute PLQY measurements for each blend investigated. Markers on selected data points as 'guides to the eye' only.

Figure 47a shows absorption and PL spectra of molecularly dissolved DBOV in anhydrous toluene solution, showing a ~7 nm Stokes shift and a clear vibronic structure. Indeed, the main emission peak at 614 nm (2.01 eV) is followed by less pronounced vibronic components peaked at 668 nm (1.85 eV) and 731 nm (1.69 eV). Notably, there is no evidence of inhomogeneous spectral broadening, typical of GQDs obtained via top-down preparation routes (e.g. exfoliation). Turning to the emissive properties of our blends in the solid state, the least concentrated film still shows a 60% PLQY with

emission peaked at 630 nm. To the best of our knowledge, such a value is the highest PLQY in the solid state reported so far for red-emitting graphene-based materials [142]. Increasing the DBOV loading, the highest PLQY achieved progressively decreases to 0.45, 0.34 and 0.26 for the concentrations of 1, 2.5 and 5 w/w %, respectively (see Figure 47c), most likely due to species with significant charge-transfer character (such as excimers/exciplexes or aggregates). Incidentally, for GQDs concentrations larger than 1%, a dominant red-shifted emission (peaked at ~ 750 nm) is detected which takes up to 76% of the overall PL spectrum (comparing the peak integral for $\lambda \geq 700$ nm).

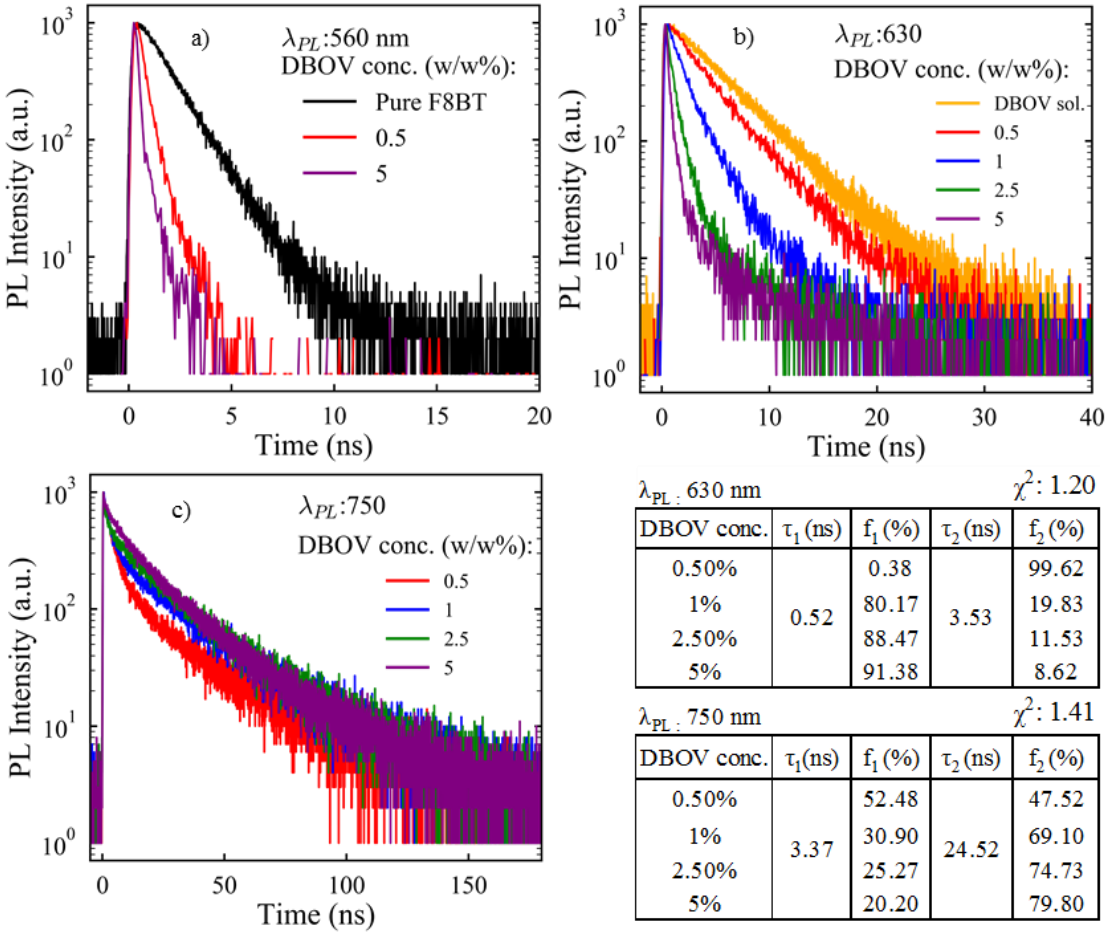

λ_{PL}: 630 nm χ^2: 1.20

DBOV conc.	τ_1 (ns)	f_1 (%)	τ_2 (ns)	f_2 (%)
0.50%	0.52	0.38	3.53	99.62
1%		80.17		19.83
2.50%		88.47		11.53
5%		91.38		8.62

λ_{PL}: 750 nm χ^2: 1.41

DBOV conc.	τ_1 (ns)	f_1 (%)	τ_2 (ns)	f_2 (%)
0.50%	3.37	52.48	24.52	47.52
1%		30.90		69.10
2.50%		25.27		74.73
5%		20.20		79.80

Figure 48: Time-resolved PL of F8BT:DBOV blends. PL decay collected in the solid state at a) 560 nm (F8BT PL), b) 630 nm (DBOV PL) and c) 750 nm. The decay of DBOV in solution (b – orange line) is also plotted. Lifetimes and relative weights resulting from the bi-exponential global fitting on the blends PL decay at 630 nm (top) and 750 nm (bottom).

Notably, a very effective host-guest energy transfer is observed already in the least concentrated blend (Figure 47b), as shown by the quenching of the fluorescence emission for $\lambda \leq 600$ nm (mainly ascribed to the F8BT emission) and by the ~ 77% host-guest energy transfer rate (Figure 48a) calculated from time-resolved data. The nature of our blends emission was studied, at 630 nm and 750 nm, via time-correlated single photon counting (TCSPC) measurements. The fluorescence decays, see Figure 48b and c, were processed through a bi-exponential reconvolutive global fitting. From the florescence at 630 nm, heavily quenched at increasing GQDs concentrations, lifetimes of $\tau_1 = 0.52$ ns and $\tau_2 = 3.53$ ns were obtained, common to all blends, which I attribute to the emission from F8BT and DBOV, respectively ($\chi^2 = 1.2$, please see the table in Figure 48). Indeed, from the GQDs emission decay in solution, also plotted in Figure 48b, I obtain a lifetime of 4.6 ns ($\chi^2 = 1.0$). As expected, upon increasing the dopant ratio, the relative weight of the GQDs emission suffer a ~ 90 % drop, in favour of the quenched F8BT fluorescence.

On the same blends, the fit of the PL decay at 750 nm gave us two characteristic decay times, $\tau_1 = 3.4$ ns and $\tau_2 = 24.5$ ns ($\chi^2 = 1.41$, see the table in Figure 48), which we ascribe to (quenched) GQDs emission (DBOV PL decay in solution at 750 nm gave a lifetime $\tau = 4.9$ ns), and to the radiative decay of long-lived weakly interacting species (aggregates and/or excimers or exciplexes), respectively. The relative weight of the long-lived species, emitting at 750 nm, grows at increasing dopant concentrations, and it becomes dominant (up to 80%) for the two most concentrated blends (2.5 and 5 w/w %).

We investigated further our blends via ultrafast transient absorption (TA), see Figure 49a, these experiments were carried in IIT by Dr G. Paternó. The transient spectrum reports the typical TA features of F8BT, namely: photobleaching (PB) due to ground state absorption at 500 nm, broad stimulated emission (SE) band centred at 560 nm and photo-induced absorption (PA, excited state absorption) in the red-NIR part of the spectrum.

Comparing the data collected for the blends with those relative to the pure F8BT, I find additional evidence of the efficient host-guest energy transfer previously discussed. Indeed, I observe the quenching of the F8BT SE signal by increasing the DBOV loading.

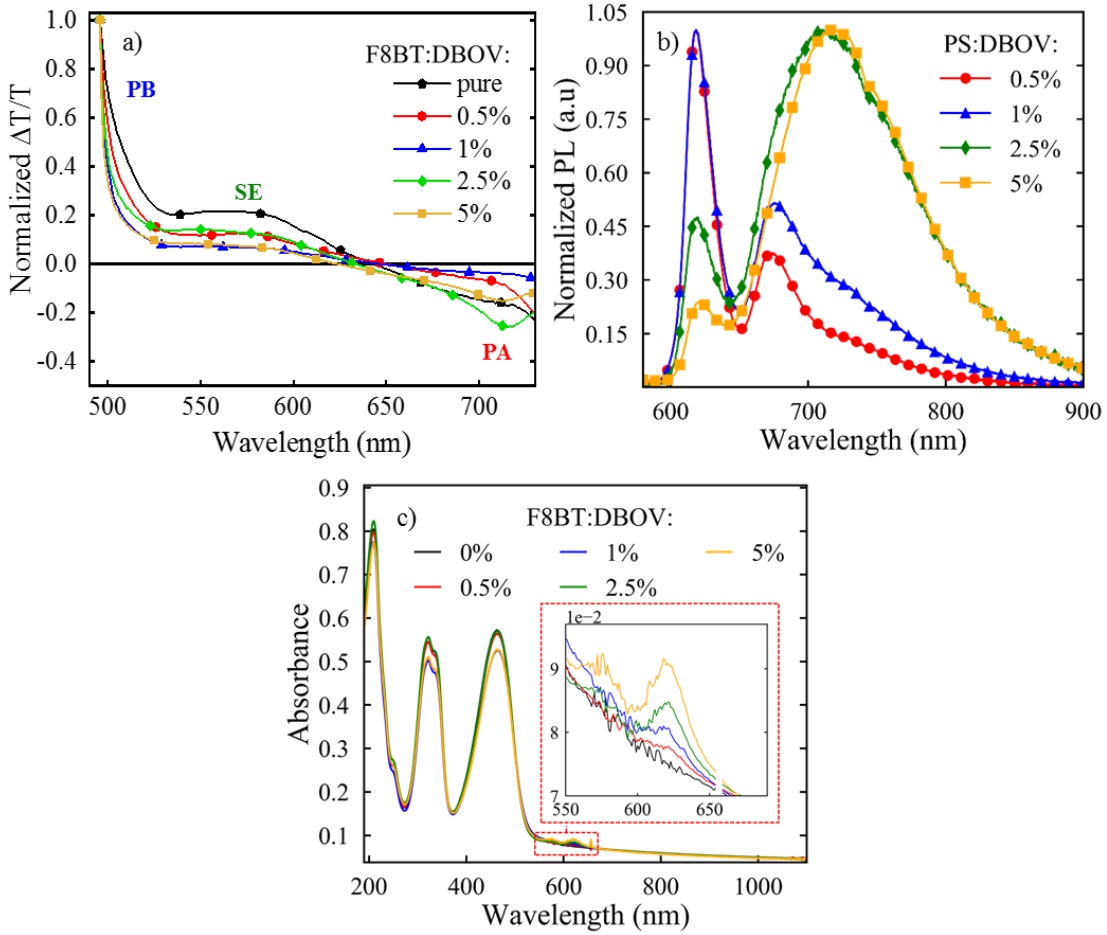

Figure 49: a) ultrafast transient absorption spectra of the blends investigated (pump-probe delay 1 ps); b) PL spectra of DBOV in PS at different dopant loadings; c) absorption spectra of DBOV blended with F8BT. Markers on selected data points as 'guides to the eye' only.

Importantly, we note the appearance of an additional and well-defined PA signal at ~730 nm for samples with a higher GDQs loading (Figure 49a). This is ascribed to the absorption of bimolecular excited species, whose radiative decay generates the signal observed at ~750 nm.

Furthermore we collected the photoluminescence of DBOV in polystyrene (PS) to

investigate further the origin of the emission at 750 nm, see Figure 49b. The blend emission spectra follow an evolution similar to what observed in F8BT. Considering that the PS aliphatic backbone does not favour the formation of exciplexes with DBOV, we conclude that the red-shifted emission is mainly due to the formation of emissive excimers at increasing GQDs loadings. We exclude aggregates because of the substantial lifetimes observed for this red-shifted emission, and also for lack of aggregates signatures in the absorption spectra, see Figure 49 c.

Importantly, we think that self-absorption might play only a minor role in the red-shifting of the overall emission. Indeed, in our blends, we detect the fluorescence of long-living species (up to $\tau > 20$ ns) their absorption spectrum is largely dominated by the F8BT absorption peaks (see Figure 49c).

6.4 Morphological characterization

In the range of the concentrations investigated we did not observe any phase segregation as suggested by the AFM measurements on our blends in the solid state, see Figure 50.

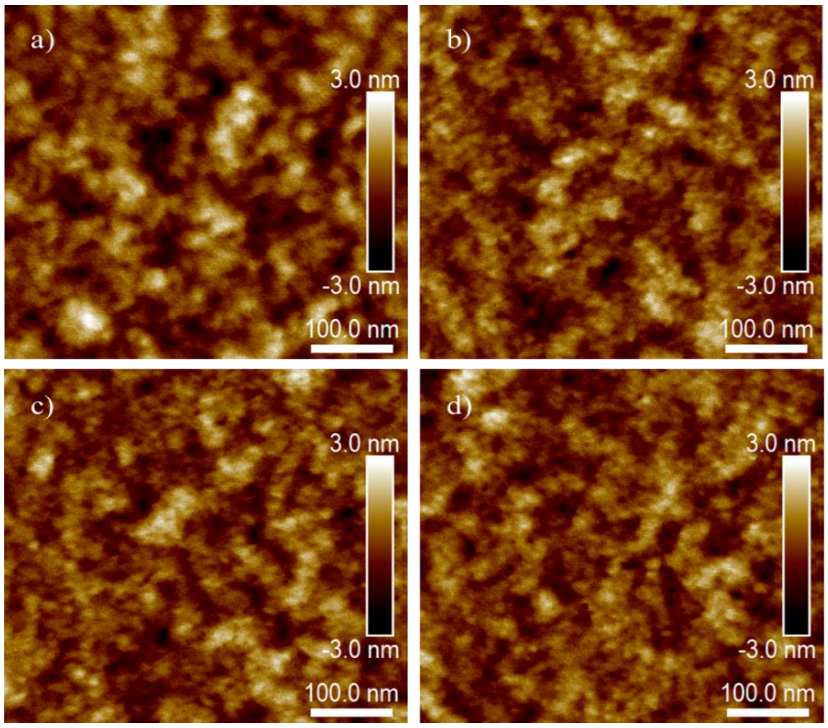

Figure 50: AFM images of thin films of F8BT:DBOV blends with different dopant loadings: a) 0, b) 1%, c) 2.5, d) 5 w/w %.

The analysis was performed in air via a Bruker Dimension Icon equipment (PeakForce tapping mode) on an area of 500 nm^2.

6.5 Device performances

We fabricated solution processed GQDs LEDs with the stack architecture ITO/PEDOT:PSS/F8BT:GQDs/Ca/Al as reported in Figure 51a. In the same panel are plotted the EL spectra of devices with increasing loadings of nanographene dots. The F8BT EL is heavily quenched already in the least doped blend, thanks to the already

proved efficient host-guest energy transfer, in favour of the DBOV narrow (FWHM ~30 nm) electroluminescence as shown in the inset in Figure 51c. Gradually, the formation of DBOV excimers shifts the EL peak towards the NIR region, with an EL maximum at 750 nm for the 5 w/w % blend. In Figure 51, we report the current density-voltage-radiance (J-V-R) characteristics and EQE versus current density of LEDs incorporating atomically defined GQDs with loading of 0, 0.5, 1, 2.5 and 5 w/w %. Remarkably, the diode incorporating the 0.5 w/w % GQDs-F8BT blend exhibits an EQEs of 0.67 %, (efficacy of 0.56 Cd/A at 7.1 V) with a turn-on voltage (V_{ON}) of 2.9 V and a maximum EL of 2.93 mW/cm^2 (1300 cd/m^2) peaked at 630 nm.

To the best of our knowledge this is one of the highest efficiencies reported for red-emitting nanographenes. We consider the exceptional performance of these devices to be meanly related to the excellent host-guest energy transfer within our blends and to the unique emissive properties of our GQDs, enabled by the specifically-designed bottom-up synthetic process. Namely, the latter ensures GQDs having an identical, planar, and atomically-precise structure with a well-defined combination of armchair and zig-zag edges. Therefore, such dots are less affected by structural defects or unwanted doping groups, a common drawback for GQDs obtained via top-down or solvothermal synthetic routes, which represent one of the major issues for GQDs-based red-emitting optoelectronic devices. Interestingly the devices with the highest GQDs loadings (5 w/w %) of DBOV, achieve NIR emission (750 nm, peak) with a maximum EQE of 0.28% (0.034 cd/A) and a maximum radiance of 1.5 mW/cm^2 (107 cd/m^2). Our devices exhibit current-independent emission. In fact I measured the EL at increasing device driving voltages, observing no shift of the EL spectra (see Figure 52a, b).

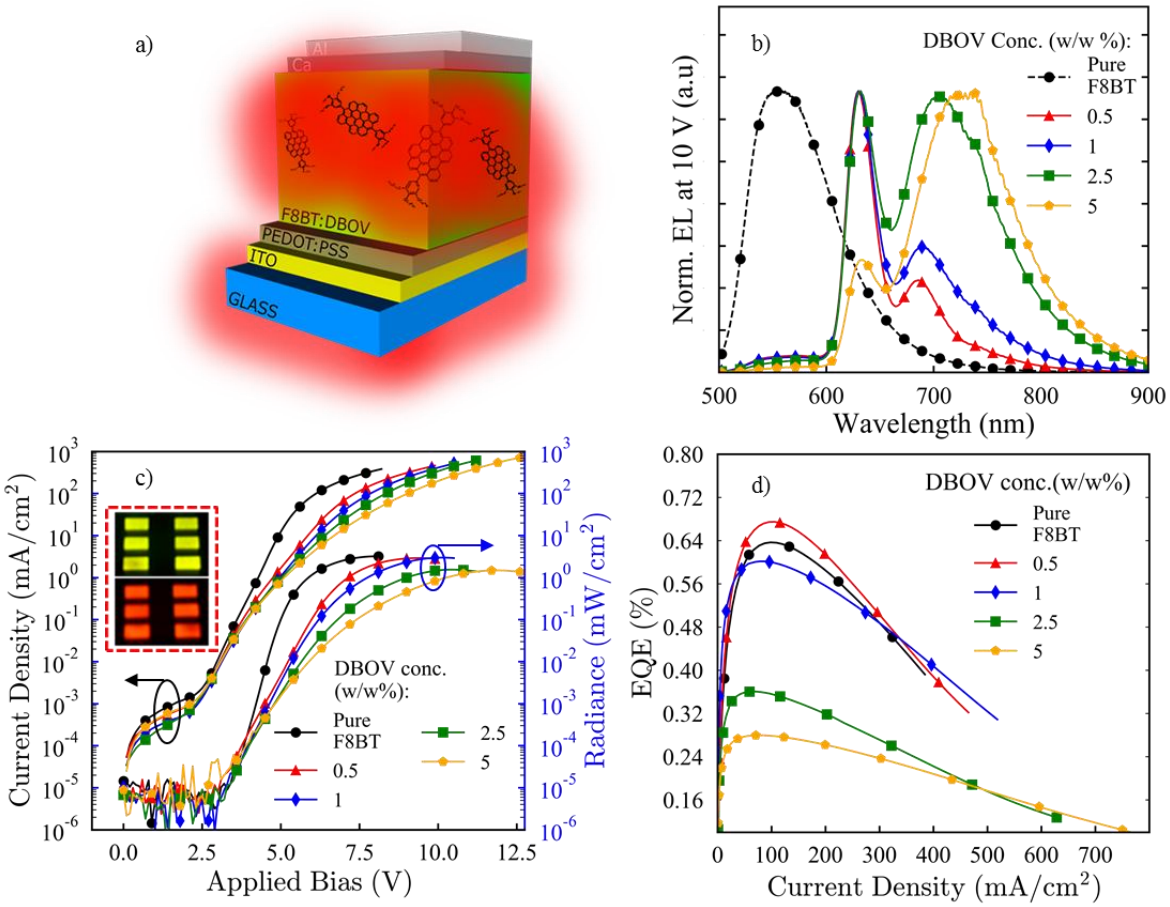

Figure 51: Optoelectronic performances of F8BT based devices incorporating different loading of DBOV. a) Device stack architecture; b) Electroluminescence spectra; c) J-V-R characteristics; inset: pure F8BT (up) and F8BT:DBOV 0.5 w/w % (down) devices emission at 5V; d) Best performing devices EQE. Markers on selected data points as 'guides to the eye' only.

Performance statistics for devices based on the different blends are showed in Figure 52b and c. Interestingly, devices V_{ON} slightly reduces increasing the GQDs concentration from 3.4 ± 0.1 V (neat F8BT) to 2.9 ± 0.3 V (F8BT: DBOV 5 w/w %) 32. This behaviour, already reported for GQDs, suggests that GQDs contribute to the charge transport thus majority carriers are favourably injected directly on the less energetic DBOV HOMO level.

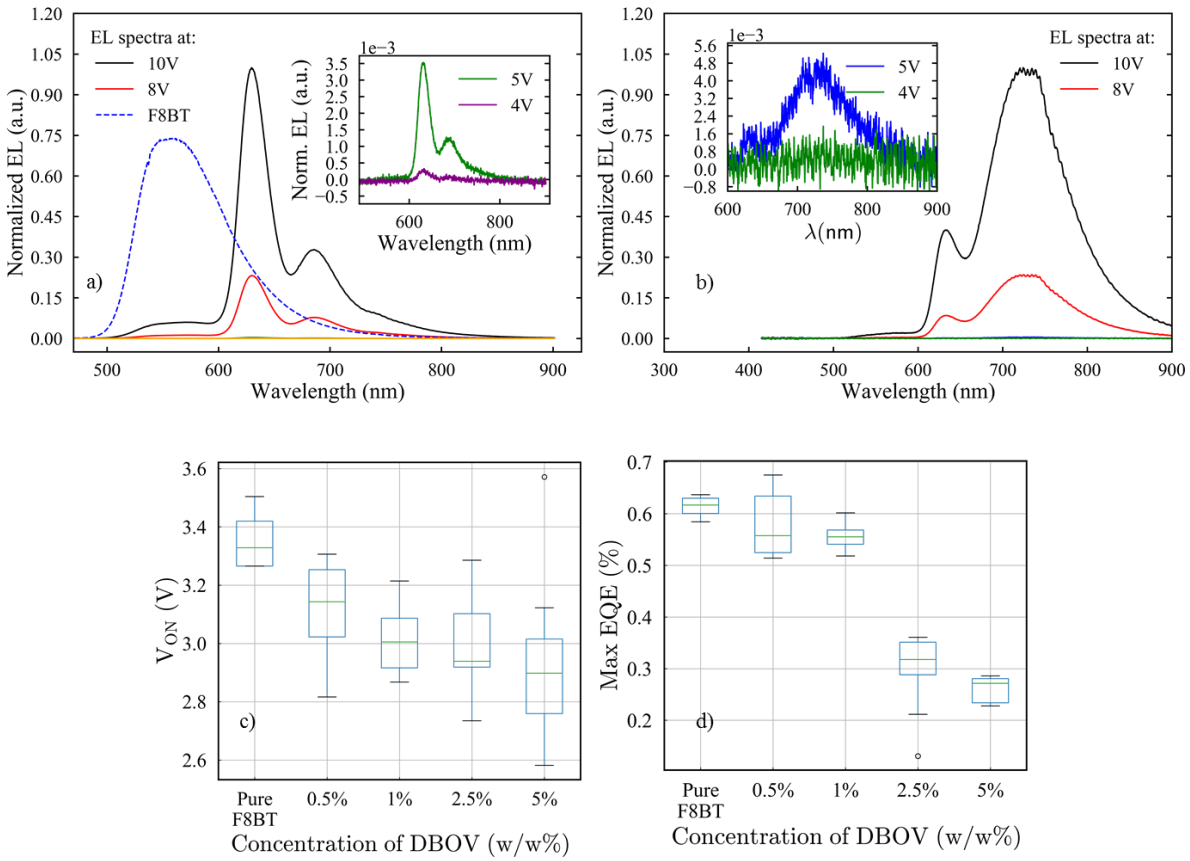

Figure 52: EL spectra of LEDs incorporating different F8BT:DBOV blends at different applied bias values; Blends: a) 0.5 – in dashed blue line the EL of pure F8BT, b) 5 w/w %. In each plot the spectra are normalized against the one collected at 10V. Device performance statistics for 10 LEDs for each blend.

We achieved the maximum radiance of 3.01 mW/cm^2 (980 cd/m^2) for devices based on the 1 w/w % blend which takes advantage of the still high EQE (0.57 ± 0.06%) and larger current density (than in the 0.5 % blend) passing through the devices.

6.6 Conclusions

In summary, we report the fabrication of fully solution processed light-emitting diodes incorporating highly emissive and atomically defined GQDs, blended in F8BT, with electroluminescence in the red region (630 nm) of the visible spectrum and a FWHM of 30 nm, comparable with the colour purity of inorganic Cd-based QDs. Our devices show

voltage independent EL spectra, and reach maximum EQE of 0.67% (0.56 cd/A) and radiance of 2.93 mW/cm^2 (1300 cd/m^2) for GQDs loadings of 0.5 w/w %. To the best of our knowledge, such devices are among the brightest and most efficient GQDs-based, solution-processed red-emitting LED ever reported. We ascribe these results to the properties of our blend which combines the extremely efficient host-guest energy transfer with the record 60% DBOV PLQY in the solid state. The latter is enabled by the specifically developed bottom-up synthetic process which allows the design of defect-free GQDs having a unique combination of armchair and zig-zag edges and monodisperse dimension. The current result proves that efficient red-emitting GQDs-based LEDs can be achieved. This paves the way to solution-processed optoelectronic devices based on highly emissive and potentially biocompatible GQDs, emitting in the whole visible spectrum.

7 Conclusions and outlook

Following the growing interest toward multifunctional devices, which are sensitive to external stimuli, two different light-responsive emitting-devices, embedding photochromic dopants, were designed and realized. Their optoelectronic performance can be remotely controlled via light-irradiation.

Finally, were investigated the optoelectronic performances of devices based on a new, promising class of emitting materials: graphene quantum dots. This study was initially moved by the search for innovative chromophores showing fluorescence with minimal spectral overlap with the absorption spectrum of our photochromic dopants.

7.1 Light-responsive devices

In chapter 3 is reported an example of optically switchable light-emitting diode based on blends of F8BT with different loadings of DAE-tF, a diarylethene derivative. The blend has been designed to generate optically-switchable charge traps for both holes and electrons. The dual action of on transport of the charge carriers has been demonstrated, for the first time, via the fabrication and characterization of optically-switchable single carriers devices. Furthermore, direct laser lithography has been used to pattern device electrodes in a custom design to achieve the fabrication of micro-sized OLEDs incorporating DAE-tF.

Chapter 4 furthers the research activity toward the fabrication of micro-sized light-responsive devices. Here, optically switchable organic light emitting transistors OLETs having a 2.5 μm channel length have been characterized. Different emitting polymers and DAEs derivatives were judiciously combined to achieve the light-responsivity for devices emitting in the whole visible spectrum. It was also demonstrated also the possibility to pattern the emissive area to the mesoscale via a light-irradiation.

Both the experiments described in the thesis show the potential of light-responsive devices, in which the optoelectronic performance can be tuned remotely and reversibly via light irradiation. Such OSOLEDs and OSOLETs, once the technology will be mature, might be used for smart display application, smart signage and visual light communication (VLC). At the moment efforts must be spent towards the improvement of the overall device performances and on testing of the device performance cyclability over tens of thousands irradiation cycles.

7.2 Red-emitting graphene quantum dots

In the final section of the dissertation has been investigated the performance of LEDs based on air-stable, non-toxic red-emitting GQDs. In this work, thanks to the atomically defined and monodisperse material, synthesized via a bottom-up approach, and the right choice of the host material and device architecture were achieved device performance which represents the state of the art for LEDs based on red-emitting GQDs. This result paves the way for a new LED technology based on air-stable, biocompatible and metal-free GQDs. Such materials are often described as future alternative to the colloidal QDs, which are often highly toxic and obtained via expensive synthetic routes. Further efforts need to be spent to bring the overall device performance closer to OLED technology based on fluorescent emitting-polymers or on phosphorescent organometallic complexes.

8 Bibliography

[1] Das, R. and H. Peter, “Printed organic and flexible electronics forecasts players and opportunities: 2017-2027.” IDtechEX, 2017.

[2] Skotheim, T. A. and J. R. Reynolds, *Handbook of conducting polymers.* CRC, 2007.

[3] Cheng, G., Y. Zhang, Y. Zhao, Y. Lin, C. Ruan, S. Liu, T. Fei, Y. Ma, and Y. Cheng, “White organic light-emitting devices with a phosphorescent multiple emissive layer,” *Appl. Phys. Lett.*, vol. 89, no. 4, 2006.

[4] Liu, Y., L. S. Cui, M. F. Xu, X. B. Shi, D. Y. Zhou, Z. K. Wang, Z. Q. Jiang, and L. S. Liao, “Highly efficient single-layer organic light-emitting devices based on a bipolar pyrazine/carbazole hybrid host material,” *J. Mater. Chem. C*, vol. 2, no. 14, pp. 2488–2495, 2014.

[5] Nakayama, T., K. Hiyama, K. Furukawa, and H. Ohtani, “Development of Phosphorescent White OLED with Extremely High Power Efficiency and Long Lifetime,” *SID Dig.*, vol. 5, pp. 1018–1021, 2007.

[6] Morgado, J., F. Cacialli, R. Iqbal, S. Moratti, A. Holmes, G. Yahioglu, L. Milgrom, and R. Friend, “Forster energy transfer and control of the luminescence in blends of an orange-emitting poly(p-phenylenevinylene) and a red-emitting tetraphenylporphyrin,” *J. Mater. Chem.*, vol. 11, pp. 278–283, 2001.

[7] Cacialli, F. and P. Bruschi, “Site-selective chemical-vapor-deposition of submicron-wide conducting polypyrrole films: Morphological investigations with the scanning electron and the atomic force microscope,” *J. Appl. Phys.*, vol. 80, no.

1, p. 70, 1996.

[8] Morgado, J., F. Cacialli, J. Grüner, N. C. Greenham, and R. H. Friend, "Luminescence properties of poly(p -phenylenevinylene): Role of the conversion temperature on the photoluminescence and electroluminescence efficiencies," *J. Appl. Phys.*, vol. 85, no. 3, pp. 1784–1791, Feb. 1999.

[9] Ho, P. K. H., J. I.-S. Kim, J. H. Burroughes, H. Becker, S. F. Y. Li, T. M. Brown, F. Cacialli, and R. H. Friend, "Molecular-scale interface engineering for polymer light-emitting diodes," *Nature*, vol. 404, no. 6777, pp. 481–484, 2000.

[10] Morgado, J., F. Cacialli, R. H. Friend, R. Iqbal, G. Yahioglu, L. R. Milgrom, S. C. Moratti, and A. B. Holmes, "Tuning the red emission of a soluble poly(p-phenylene vinylene) upon grafting of porphyrin side groups," *Chem. Phys. Lett.*, vol. 325, no. 5–6, pp. 552–558, 2000.

[11] Slooff, L. H., A. Polman, F. Cacialli, R. H. Friend, G. A. Hebbink, F. C. J. M. Van Veggel, and D. N. Reinhoudt, "Near-infrared electroluminescence of polymer light-emitting diodes doped with a lissamine-sensitized Nd3+ complex," *Appl. Phys. Lett.*, vol. 78, no. 15, pp. 2122–2124, 2001.

[12] Lim, S.-F., R. H. Friend, I. D. Rees, J. Li, Y. Ma, K. Robinson, A. B. Holmes, E. Hennebicq, D. Beljonne, and F. Cacialli, "Suppression of Green Emission in a New Class of Blue-Emitting Polyfluorene Copolymers with Twisted Biphenyl Moieties," *Adv. Funct. Mater.*, vol. 15, no. 6, pp. 981–988, Jun. 2005.

[13] Sardone, L., V. Palermo, E. Devaux, D. Credgington, M. de Loos, G. Marletta, F. Cacialli, J. van Esch, and P. Samorì, "Electric-Field-Assisted Alignment of Supramolecular Fibers," *Adv. Mater.*, vol. 18, no. 10, pp. 1276–1280, May 2006.

[14] Shirakawa, H., E. J. Louis, A. G. MacDiarmid, C. K. Chiang, and A. J. Heeger, "Synthesis of electrically conducting organic polymers: halogen derivatives of polyacetylene, (CH) x," *J. Chem. Soc. Chem. Commun.*, no. 16, p. 578, Jan. 1977.

[15] Pope, M., H. P. Kallmann, and P. Magnante, "Electroluminescence in Organic Crystals," *J. Chem. Phys.*, vol. 38, no. 8, pp. 2042–2043, Apr. 1963.

[16] Burroughes, J. H., D. D. C. Bradley, A. R. Brown, R. N. Marks, K. Mackay, R. H. Friend, P. L. Burns, and A. B. Holmes, "Light-emitting diodes based on conjugated polymers," *Nature*, vol. 347, no. 6293, pp. 539–541, Oct. 1990.

[17] Sze, S. M. and K. K. Ng, *Physics of semiconductor devices*. Wiley-Interscience, 2007.

[18] Tang, C. W. and S. A. VanSlyke, "Organic electroluminescent diodes," *Appl. Phys. Lett.*, vol. 51, no. 12, pp. 913–915, Sep. 1987.

[19] Tang, C. W., "Two- layer organic photovoltaic cell," *Appl. Phys. Lett.*, vol. 48, no. 2, pp. 183–185, Jan. 1986.

[20] Brabec, C. J., N. S. Sariciftci, and J. C. Hummelen, "Plastic Solar Cells," *Adv. Funct. Mater.*, vol. 11, no. 1, pp. 15–26, Feb. 2001.

[21] Koezuka, H., A. Tsumura, and T. Ando, "Field-effect transistor with polythiophene thin film," *Synth. Met.*, vol. 18, no. 1–3, pp. 699–704, Feb. 1987.

[22] Horowitz, G., "Organic field-effect transistors," *Adv. Mater.*, vol. 10, no. 5, pp. 365–377, 1998.

[23] Coropceanu, V., J. Cornil, D. A. da Silva Filho, Y. Olivier, R. Silbey, and J.-L. Brédas, "Charge Transport in Organic Semiconductors," *Chem. Rev.*, vol. 107, no.

4, pp. 926–952, Apr. 2007.

[24] Brédas, J.-L., D. Beljonne, V. Coropceanu, and J. Cornil, “Charge-Transfer and Energy-Transfer Processes in π-Conjugated Oligomers and Polymers: A Molecular Picture,” *Chem. Rev.*, vol. 104, no. 11, pp. 4971–5004, Nov. 2004.

[25] Cornil, J., D. Beljonne, J.-P. Calbert, and J.-L. Brédas, “Interchain Interactions in Organic π-Conjugated Materials: Impact on Electronic Structure, Optical Response, and Charge Transport,” *Adv. Mater.*, vol. 13, no. 14, pp. 1053–1067, Jul. 2001.

[26] Friend, R. H., R. W. Gymer, A. B. Holmes, J. H. Burroughes, R. N. Marks, C. Taliani, D. D. C. Bradley, D. A. Dos Santos, J. L. Brédas, M. Lögdlund, and W. R. Salaneck, “Electroluminescence in conjugated polymers,” *Nature*, vol. 397, no. 6715, pp. 121–128, Jan. 1999.

[27] Tregnago, G., “Photophysics and applications of organic semiconductors,” *Dr. thesis, UCL (University Coll. London).* , Apr. 2015.

[28] van Mullekom, H., “Developments in the chemistry and band gap engineering of donor–acceptor substituted conjugated polymers,” *Mater. Sci. Eng. R Reports*, vol. 32, no. 1, pp. 1–40, Feb. 2001.

[29] Friend, R. H., D. D. C. Bradley, and P. D. Townsend, “Photo-excitation in conjugated polymers,” *J. Phys. D. Appl. Phys.*, vol. 20, no. 11, pp. 1367–1384, Nov. 1987.

[30] Salaneck, W. R., R. H. Friend, and J. L. Brédas, “Electronic structure of conjugated polymers: consequences of electron–lattice coupling,” *Phys. Rep.*, vol. 319, no. 6, pp. 231–251, Oct. 1999.

[31] Baldo, M. A., D. F. O'Brien, M. E. Thompson, and S. R. Forrest, "Excitonic singlet-triplet ratio in a semiconducting organic thin film," *Phys. Rev. B*, vol. 60, no. 20, pp. 14422–14428, Nov. 1999.

[32] Troisi, A., "Charge transport in high mobility molecular semiconductors: classical models and new theories," *Chem. Soc. Rev.*, vol. 40, no. 5, p. 2347, Apr. 2011.

[33] Shuai, Z., H. Geng, W. Xu, Y. Liao, and J.-M. André, "From charge transport parameters to charge mobility in organic semiconductors through multiscale simulation," *Chem. Soc. Rev.*, vol. 43, no. 8, p. 2662, Mar. 2014.

[34] Blom, P. W. M. and M. C. J. M. Vissenberg, "Charge transport in poly(p-phenylene vinylene) light-emitting diodes," *Mater. Sci. Eng. R Reports*, vol. 27, no. 3–4, pp. 53–94, May 2000.

[35] Morin, J.-F., M. Leclerc, D. Adès, and A. Siove, "Polycarbazoles: 25 Years of Progress," *Macromol. Rapid Commun.*, vol. 26, no. 10, pp. 761–778, May 2005.

[36] Balzani, V., P. Ceroni, and A. Juris, *Photochemistry and photophysics : concepts, research, applications*. Wiley, 2014.

[37] Lakowicz, J. R., *Principles of fluorescence spectroscopy*. Springer, 2006.

[38] Minaev, B., G. Baryshnikov, and H. Agren, "Principles of phosphorescent organic light emitting devices," *Phys. Chem. Chem. Phys.*, vol. 16, no. 5, pp. 1719–1758, 2014.

[39] Gordon, M. (Michael) and W. R. Ware, *The exciplex*. Academic Press, 1975.

[40] Scholes, G. D. and G. Rumbles, "Excitons in nanoscale systems," *Nat. Mater.*, vol. 5, no. 9, pp. 683–696, Sep. 2006.

[41] Lee, H., Y.-C. Cheng, and G. R. Fleming, "Coherence Dynamics in Photosynthesis: Protein Protection of Excitonic Coherence," *Science (80-.).*, vol. 316, no. 5830, pp. 1462–1465, Jun. 2007.

[42] Turro, N. J., V. Ramamurthy, and J. C. (Juan C. . Scaiano, *Principles of molecular photochemistry : an introduction*. University Science Books, 2009.

[43] Novoselov, K. S., V. I. Fal'Ko, L. Colombo, P. R. Gellert, M. G. Schwab, and K. Kim, "A roadmap for graphene," *Nature*, vol. 490, no. 7419, pp. 192–200, 2012.

[44] Nevius, M. S., M. Conrad, F. Wang, A. Celis, M. N. Nair, A. Taleb-Ibrahimi, A. Tejeda, and E. H. Conrad, "Semiconducting Graphene from Highly Ordered Substrate Interactions," *Phys. Rev. Lett.*, vol. 115, no. 13, p. 136802, Sep. 2015.

[45] Castro, E. V, K. S. Novoselov, S. V Morozov, N. M. R. Peres, J. M. B. L. dos Santos, J. Nilsson, F. Guinea, A. K. Geim, and A. H. C. Neto, "Biased Bilayer Graphene: Semiconductor with a Gap Tunable by the Electric Field Effect," *Phys. Rev. Lett.*, vol. 99, no. 21, p. 216802, Nov. 2007.

[46] Balog, R., B. Jørgensen, L. Nilsson, M. Andersen, E. Rienks, M. Bianchi, M. Fanetti, E. Lægsgaard, A. Baraldi, S. Lizzit, Z. Sljivancanin, F. Besenbacher, B. Hammer, T. G. Pedersen, P. Hofmann, and L. Hornekær, "Bandgap opening in graphene induced by patterned hydrogen adsorption," *Nat. Mater.*, vol. 9, p. 315, Mar. 2010.

[47] Zhang, Y., T.-T. Tang, C. Girit, Z. Hao, M. C. Martin, A. Zettl, M. F. Crommie, Y. R. Shen, and F. Wang, "Direct observation of a widely tunable bandgap in bilayer graphene," *Nature*, vol. 459, p. 820, Jun. 2009.

[48] Ohta, T., A. Bostwick, T. Seyller, K. Horn, and E. Rotenberg, "Controlling the

Electronic Structure of Bilayer Graphene," *Science (80-.).*, vol. 313, no. 5789, p. 951 LP-954, Aug. 2006.

[49] Li, X., M. Rui, J. Song, Z. Shen, and H. Zeng, "Carbon and Graphene Quantum Dots for Optoelectronic and Energy Devices: A Review," *Adv. Funct. Mater.*, vol. 25, no. 31, pp. 4929–4947, 2015.

[50] Shen, J., Y. Zhu, X. Yang, and C. Li, "Graphene quantum dots: Emergent nanolights for bioimaging, sensors, catalysis and photovoltaic devices," *Chem. Commun.*, vol. 48, no. 31, pp. 3686–3699, 2012.

[51] Han, M. Y., B. Özyilmaz, Y. Zhang, and P. Kim, "Energy Band-Gap Engineering of Graphene Nanoribbons," *Phys. Rev. Lett.*, vol. 98, no. 20, p. 206805, May 2007.

[52] Yan, X., B. Li, and L. Li, "Colloidal Graphene Quantum Dots with Well-Defined Structures," *Acc. Chem. Res.*, vol. 46, no. 10, pp. 2254–2262, Oct. 2013.

[53] Bacon, M., S. J. Bradley, and T. Nann, "Graphene quantum dots," *Particle and Particle Systems Characterization*, vol. 31, no. 4. pp. 415–428, 2014.

[54] Fan, Z., Y. Li, X. Li, L. Fan, S. Zhou, D. Fang, and S. Yang, "Surrounding media sensitive photoluminescence of boron-doped graphene quantum dots for highly fluorescent dyed crystals, chemical sensing and bioimaging," *Carbon N. Y.*, vol. 70, pp. 149–156, 2014.

[55] Fan, Z., S. Li, F. Yuan, and L. Fan, "Fluorescent graphene quantum dots for biosensing and bioimaging," *RSC Adv.*, vol. 5, no. 25, pp. 19773–19789, Feb. 2015.

[56] Zhang, M., L. Bai, W. Shang, W. Xie, H. Ma, Y. Fu, D. Fang, H. Sun, L. Fan, M. Han, C. Liu, and S. Yang, "Facile synthesis of water-soluble, highly fluorescent

graphene quantum dots as a robust biological label for stem cells," *J. Mater. Chem.*, vol. 22, no. 15, p. 7461, Mar. 2012.

[57] Rosillo-Lopez, M., T. J. Lee, M. Bella, M. Hart, and C. G. Salzmann, "Formation and chemistry of carboxylic anhydrides at the graphene edge," *RSC Adv.*, vol. 5, no. 126, pp. 104198–104202, Dec. 2015.

[58] Salzmann, C. G., V. Nicolosi, and M. L. H. Green, "Edge-carboxylated graphene nanoflakes from nitric acid oxidised arc-discharge material," *J. Mater. Chem.*, vol. 20, no. 2, pp. 314–319, 2010.

[59] Zheng, H., Y. Zheng, N. Liu, N. Ai, Q. Wang, S. Wu, J. Zhou, D. Hu, S. Yu, S. Han, W. Xu, C. Luo, Y. Meng, Z. Jiang, Y. Chen, D. Li, F. Huang, J. Wang, J. Peng, *et al.*, "All-solution processed polymer light-emitting diode displays," *Nat. Commun.*, vol. 4, no. 1, p. 1971, Dec. 2013.

[60] Dong, Y., J. Shao, C. Chen, H. Li, R. Wang, Y. Chi, X. Lin, and G. Chen, "Blue luminescent graphene quantum dots and graphene oxide prepared by tuning the carbonization degree of citric acid," *Carbon N. Y.*, vol. 50, no. 12, pp. 4738–4743, Oct. 2012.

[61] Qu, D., M. Zheng, L. Zhang, H. Zhao, Z. Xie, X. Jing, R. E. Haddad, H. Fan, and Z. Sun, "Formation mechanism and optimization of highly luminescent N-doped graphene quantum dots," *Sci. Rep.*, vol. 4, no. 1, p. 5294, May 2015.

[62] Shen, J., Y. Zhu, C. Chen, X. Yang, and C. Li, "Facile preparation and upconversion luminescence of graphene quantum dots," *Chem. Commun.*, vol. 47, no. 9, pp. 2580–2582, Feb. 2011.

[63] Zhu, S., Q. Meng, L. Wang, J. Zhang, Y. Song, H. Jin, K. Zhang, H. Sun, H. Wang,

and B. Yang, “Highly photoluminescent carbon dots for multicolor patterning, sensors, and bioimaging,” *Angew. Chemie - Int. Ed.*, vol. 52, no. 14, pp. 3953–3957, 2013.

[64] Ding, H., S.-B. Yu, J.-S. Wei, and H.-M. Xiong, “Full-Color Light-Emitting Carbon Dots with a Surface-State-Controlled Luminescence Mechanism,” *ACS Nano*, vol. 10, no. 1, pp. 484–491, Jan. 2016.

[65] Bao, L., C. Liu, Z.-L. Zhang, and D.-W. Pang, “Photoluminescence-Tunable Carbon Nanodots: Surface-State Energy-Gap Tuning,” *Adv. Mater.*, vol. 27, no. 10, pp. 1663–1667, Mar. 2015.

[66] Westenhoff, S., I. A. Howard, J. M. Hodgkiss, K. R. Kirov, H. A. Bronstein, C. K. Williams, N. C. Greenham, and R. H. Friend, “Charge Recombination in Organic Photovoltaic Devices with High Open-Circuit Voltages,” *J. Am. Chem. Soc.*, vol. 130, no. 41, pp. 13653–13658, Oct. 2008.

[67] Wu, Y. and W. Zhu, “Organic sensitizers from D–π–A to D–A–π–A: effect of the internal electron-withdrawing units on molecular absorption, energy levels and photovoltaic performances,” *Chem. Soc. Rev.*, vol. 42, no. 5, pp. 2039–2058, Feb. 2013.

[68] Poplavskyy, D. and J. Nelson, “Nondispersive hole transport in amorphous films of methoxy-spirofluorene-arylamine organic compound,” *J. Appl. Phys.*, vol. 93, no. 1, pp. 341–346, Jan. 2003.

[69] Dieckmann, A., H. Bässler, and P. M. Borsenberger, “An assessment of the role of dipoles on the density- of- states function of disordered molecular solids,” *J. Chem. Phys.*, vol. 99, no. 10, pp. 8136–8141, Nov. 1993.

[70] Zhang, X., Y. Zhang, Y. Wang, S. Kalytchuk, S. V. Kershaw, Y. Wang, P. Wang, T. Zhang, Y. Zhao, H. Zhang, T. Cui, Y. Wang, J. Zhao, W. W. Yu, and A. L. Rogach, "Color-switchable electroluminescence of carbon dot light-emitting diodes," *ACS Nano*, vol. 7, no. 12, pp. 11234–11241, 2013.

[71] Ke, C. C., Y. C. Yang, and W. L. Tseng, "Synthesis of Blue-, Green-, Yellow-, and Red-Emitting Graphene-Quantum-Dot-Based Nanomaterials with Excitation-Independent Emission," *Part. Part. Syst. Charact.*, vol. 33, no. 3, pp. 132–139, 2016.

[72] Son, D. I., B. W. Kwon, D. H. Park, W.-S. Seo, Y. Yi, B. Angadi, C.-L. Lee, and W. K. Choi, "Emissive ZnO–graphene quantum dots for white-light-emitting diodes," *Nat. Nanotechnol.*, vol. 7, p. 465, May 2012.

[73] Dai, W., Y. Lei, M. Xu, P. Zhao, Z. Zhang, and J. Zhou, "Rare-Earth Free Self-Activated Graphene Quantum Dots and Copper-Cysteamine Phosphors for Enhanced White Light-Emitting-Diodes under Single Excitation," *Sci. Rep.*, vol. 7, no. 1, pp. 1–11, 2017.

[74] Kim, J. K., S. Bae, Y. Yi, M. J. Park, S. J. Kim, N. Myoung, C. Lee, B. H. Hong, and J. H. Park, "Origin of White Electroluminescence in Graphene Quantum Dots Embedded Host / Guest Polymer Light Emitting Diodes," *Nat. Publ. Gr.*, no. April, pp. 1–11, 2015.

[75] Yuan, F., Z. Wang, X. Li, Y. Li, Z. Tan, L. Fan, and S. Yang, "Bright Multicolor Bandgap Fluorescent Carbon Quantum Dots for Electroluminescent Light-Emitting Diodes," *Adv. Mater.*, vol. 29, no. 3, 2017.

[76] Song, S. H., M.-H. Jang, J. Chung, S. H. Jin, B. H. Kim, S.-H. Hur, S. Yoo, Y.-H.

Cho, and S. Jeon, “Highly Efficient Light-Emitting Diode of Graphene Quantum Dots Fabricated from Graphite Intercalation Compounds,” *Adv. Opt. Mater.*, vol. 2, no. 11, pp. 1016–1023, 2014.

[77] Kwon, W., Y. H. Kim, J. H. Kim, T. Lee, S. Do, Y. Park, M. S. Jeong, T. W. Lee, and S. W. Rhee, “High color-purity green, orange, and red light-emitting didoes based on chemically functionalized graphene quantum dots,” *Sci. Rep.*, vol. 6, pp. 1–10, 2016.

[78] Cheng, T. C., T. A. Ku, K. Y. Huang, A. S. Chou, P. H. Chang, C. C. Chang, C. F. Yue, C. W. Liu, P. H. Wang, K. T. Wong, and C. I. Wu, “Surface modification of graphene using HBC-6ImBr in solution-processed OLEDs,” *J. Appl. Phys.*, vol. 123, no. 2, 2018.

[79] Matsui, K., S. Oda, K. Yoshiura, K. Nakajima, N. Yasuda, and T. Hatakeyama, “One-Shot Multiple Borylation toward BN-Doped Nanographenes,” *J. Am. Chem. Soc.*, vol. 140, no. 4, pp. 1195–1198, 2018.

[80] Cacialli, F., “Organic semiconductors for the new millennium,” *Philos. Trans. R. Soc. London. Ser. A Math. Phys. Eng. Sci.*, vol. 358, no. 1765, pp. 173–192, Jan. 2000.

[81] Blom, P. W. M., M. J. M. de Jong, and M. G. van Munster, “Electric-field and temperature dependence of the hole mobility in poly(p-phenylene vinylene),” *Phys. Rev. B*, vol. 55, no. 2, pp. R656–R659, 1997.

[82] Blom, P. W. M., M. J. M. De Jong, and J. J. M. Vleggaar, “Electron and hole transport in poly(p-phenylene vinylene) devices,” *Appl. Phys. Lett.*, vol. 68, no. 23, pp. 3308–3310, 1996.

[83] Blom, P. W. M., M. J. M. De Jong, S. Breedijk, M. J. M. de Jong, and S. Breedijk, "Temperature dependent electron-hole recombination in polymer light-emitting diodes," *Appl. Phys. Lett.*, vol. 71, no. June, p. 930, 1997.

[84] Zhang, Y. and P. W. M. Blom, "Electron and hole transport in poly(fluorene-benzothiadiazole)," *Appl. Phys. Lett.*, vol. 98, no. 14, 2011.

[85] Mandoc, M. M., B. De Boer, G. Paasch, P. W. M. Blom, B. de Boer, G. Paasch, and P. W. M. Blom, "Trap-limited electron transport in disordered semiconducting polymers," *Phys. Rev. B*, vol. 75, no. 19, pp. 12–15, 2007.

[86] Wetzelaer, G. A. H., M. Kuik, H. T. Nicolai, and P. W. M. Blom, "Trap-assisted and Langevin-type recombination in organic light-emitting diodes," *Phys. Rev. B*, vol. 83, no. 16, p. 165204, Apr. 2011.

[87] DiBenedetto, S. A., A. Facchetti, M. A. Ratner, and T. J. Marks, "Molecular Self-Assembled Monolayers and Multilayers for Organic and Unconventional Inorganic Thin-Film Transistor Applications," *Adv. Mater.*, vol. 21, no. 14–15, pp. 1407–1433, Apr. 2009.

[88] Ahn, T., H. J. Suk, J. Won, and M. H. Yi, "Extended lifetime of pentacene thin-film transistor with polyvinyl alcohol (PVA)/layered silicate nanocomposite passivation layer," *Microelectron. Eng.*, vol. 86, no. 1, pp. 41–46, Jan. 2009.

[89] Fan, C.-L., Y.-Z. Lin, and C.-H. Huang, "Combined scheme of UV/ozone and HMDS treatment on a gate insulator for performance improvement of a low-temperature-processed bottom-contact OTFT," *Semicond. Sci. Technol.*, vol. 26, no. 4, p. 045006, Apr. 2011.

[90] Ahles, M., A. Hepp, R. Schmechel, and H. Von Seggern, "Light emission from a

polymer transistor," *Appl. Phys. Lett.*, vol. 84, no. 3, pp. 428–430, 2004.

[91] Cicoira, F. and C. Santato, "Organic light emitting field effect transistors: Advances and perspectives," *Adv. Funct. Mater.*, vol. 17, no. 17, pp. 3421–3434, 2007.

[92] Zhang, C., P. Chen, and W. Hu, "Organic Light-Emitting Transistors: Materials, Device Configurations, and Operations," *Small*, vol. 12, no. 10, pp. 1252–1294, 2016.

[93] Zaumseil, J. and H. Sirringhaus, "Electron and ambipolar transport in organic field-effect transistors," *Chem. Rev.*, vol. 107, no. 4, pp. 1296–1323, 2007.

[94] Zaumseil, J., R. H. Friend, and H. Sirringhaus, "Spatial control of the recombination zone in an ambipolar light-emitting organic transistor," *Nat. Mater.*, vol. 5, no. 1, pp. 69–74, Jan. 2006.

[95] Capelli, R., S. Toffanin, G. Generali, H. Usta, A. Facchetti, and M. Muccini, "Organic light-emitting transistors with an efficiency that outperforms the equivalent light-emitting diodes," *Nat. Mater.*, vol. 9, no. 6, pp. 496–503, Jun. 2010.

[96] Irie, M., "Diarylethenes for Memories and Switches," *Chem. Rev.*, vol. 100, no. 5, pp. 1685–1716, May 2000.

[97] Irie, M., T. Fukaminato, K. Matsuda, and S. Kobatake, "Photochromism of diarylethene molecules and crystals: Memories, switches, and actuators," *Chemical Reviews*, vol. 114, no. 24. American Chemical Society, pp. 12174–12277, 24-Dec-2014.

[98] Kobatake, S. and M. Irie, “Single-Crystalline Photochromism of Diarylethenes,” *Bull. Chem. Soc. Jpn.*, vol. 77, no. 2, pp. 195–210, Feb. 2004.

[99] Morimoto, M. and M. Irie, “Photochromism of diarylethene single crystals: crystal structures and photochromic performance,” *Chem. Commun.*, no. 31, p. 3895, Jul. 2005.

[100] Masahiro Irie, *,†, † Thorsten Lifka, † and Seiya Kobatake, and N. Kato‡, “Photochromism of 1,2-Bis(2-methyl-5-phenyl-3-thienyl)perfluorocyclopentene in a Single-Crystalline Phase,” 2000.

[101] Li, W., C. Jiao, X. Li, Y. Xie, K. Nakatani, H. Tian, and W. Zhu, “Separation of Photoactive Conformers Based on Hindered Diarylethenes: Efficient Modulation in Photocyclization Quantum Yields,” *Angew. Chemie Int. Ed.*, vol. 53, no. 18, pp. 4603–4607, Apr. 2014.

[102] Herder, M., “Improving the design of diarylethene photoswitches and their exploitation as remote-controlled building blocks,” Humboldt University, Berlin, 2015.

[103] Gilat, S. L., S. H. Kawai, and J.-M. Lehn, “Light-Triggered Molecular Devices: Photochemical Switching Of optical and Electrochemical Properties in Molecular Wire Type Diarylethene Species,” *Chem. - A Eur. J.*, vol. 1, no. 5, pp. 275–284, Aug. 1995.

[104] Seefeldt, B., K. Altenhöner, O. Tosic, T. Geisler, M. Sauer, and J. Mattay, “Kinetic studies on visible-light-switchable photochromic fluorophores based on diarylethenes,” *Photochem. Photobiol. Sci.*, vol. 10, no. 9, pp. 1488–1495, Sep. 2011.

[105] Gemayel, M. El, K. Börjesson, M. Herder, D. T. Duong, J. A. Hutchison, C. Ruzié, G. Schweicher, A. Salleo, Y. Geerts, S. Hecht, E. Orgiu, and P. Samorì, "Optically switchable transistors by simple incorporation of photochromic systems into small-molecule semiconducting matrices," *Nat. Commun.*, vol. 6, no. 1, p. 6330, May 2015.

[106] Orgiu, E., N. Crivillers, M. Herder, L. Grubert, M. Pätzel, J. Frisch, E. Pavlica, D. T. Duong, G. Bratina, A. Salleo, N. Koch, S. Hecht, and P. Samorì, "Optically switchable transistor via energy-level phototuning in a bicomponent organic semiconductor," *Nat. Chem.*, vol. 4, no. 8, pp. 675–679, Jun. 2012.

[107] Shallcross, R. C., P. O. Körner, E. Maibach, A. Köhnen, and K. Meerholz, "A photochromic diode with a continuum of intermediate states: Towards high density multilevel storage," *Adv. Mater.*, vol. 25, no. 34, pp. 4807–4813, 2013.

[108] Koppen, S., W. Langel, T. Loewenstein, A. Hastall, M. Mingebach, Y. Zimmermann, A. Neudeck, D. Schlettwein, S. Koppen, W. Langel, T. Loewenstein, A. Hastall, M. Mingebach, Y. Zimmermann, A. Neudeck, D. Schlettwein, S. Koppen, and W. Langel, "Textile electrodes as substrates for the electrodeposition of porous ZnO.," *Phys. Chem. Chem. Phys.*, vol. 10, no. 14, pp. 1907–1915, 2008.

[109] Van Der Holst, J. J. M., M. A. Uijttewaal, R. Balasubramanian, R. Coehoorn, P. A. Bobbert, G. A. De Wijs, and R. A. De Groot, "Modeling and analysis of the three-dimensional current density in sandwich-type single-carrier devices of disordered organic semiconductors," *Phys. Rev. B - Condens. Matter Mater. Phys.*, vol. 79, no. 8, pp. 1–11, 2009.

[110] Zacharias, P., M. C. Gather, A. Köhnen, N. Rehmann, and K. Meerholz,

"Photoprogrammable Organic Light-Emitting Diodes," pp. 4038–4041, 2009.

[111] Qian, Y., X. Xu, W. Li, J. Wang, B. Wei, Q. Wei, X. Yan, W. Hu, Y. Lu, L. Xie, X. Zhang, and W. Huang, "Photo-induced storage and mask-free arbitrary micro-patterning in solution-processable and simple-structured photochromic organic light-emitting diodes," *Org. Electron. physics, Mater. Appl.*, vol. 26, pp. 476–480, 2015.

[112] Ye, J., C. Liu, C. Ou, M. Cai, S. Chen, Q. Wei, W. Li, Y. Qian, L. Xie, B. Mi, Z. Gao, and W. Huang, "Universal Strategy for Cheap and Color-Stable Single-EML WOLEDs Utilizing Two Complementary-Color Nondoped Emitters without Energy Transfer," *Adv. Opt. Mater.*, vol. 2, no. 10, pp. 938–944, Oct. 2014.

[113] de Mello, J. C., H. F. Wittmann, and R. H. Friend, "An improved experimental determination of external photoluminescence quantum efficiency," *Adv. Mater.*, vol. 9, no. 3, pp. 230–232, Mar. 1997.

[114] Johansson, N., F. Cacialli, K. Z. Xing, G. Beamson, D. T. Clark, R. H. Friend, and W. R. Salaneck, "A study of the ITO-on-PPV interface using photoelectron spectroscopy," *Synth. Met.*, vol. 92, no. 3, pp. 207–211, Feb. 1998.

[115] Kim, J. S., F. Cacialli, M. Granström, R. H. Friend, N. Johansson, W. R. Salaneck, R. Daik, and W. J. Feast, "Characterisation of the properties of surface-treated indium-tin oxide thin films," *Synth. Met.*, vol. 101, no. 1–3, pp. 111–112, May 1999.

[116] Frisch, J., M. Herder, P. Herrmann, G. Heimel, S. Hecht, and N. Koch, "Photoinduced reversible changes in the electronic structure of photochromic diarylethene films," *Appl. Phys. A*, vol. 113, no. 1, pp. 1–4, 2013.

[117] Herder, M., B. M. Schmidt, L. Grubert, M. Pätzel, J. Schwarz, and S. Hecht, "Improving the fatigue resistance of diarylethene switches," *J. Am. Chem. Soc.*, vol. 137, no. 7, pp. 2738–2747, Feb. 2015.

[118] Blyth, R. I. R., S. A. Sardar, F. P. Netzer, and M. G. Ramsey, "Influence of oxygen on band alignment at the organic/aluminum interface," *Appl. Phys. Lett.*, vol. 77, no. 8, pp. 1212–1214, Aug. 2000.

[119] Hou, L., X. Zhang, G. F. Cotella, G. Carnicella, M. Herder, B. M. Schmidt, M. Pätzel, S. Hecht, F. Cacialli, and P. Samorì, "Optically switchable organic light-emitting transistors," *Nat. Nanotechnol.*, vol. 14, no. 4, pp. 347–353, Apr. 2019.

[120] Herder, M., F. Eisenreich, A. Bonasera, A. Grafl, L. Grubert, M. Pätzel, J. Schwarz, and S. Hecht, "Light-Controlled Reversible Modulation of Frontier Molecular Orbital Energy Levels in Trifluoromethylated Diarylethenes," *Chem. - A Eur. J.*, vol. 23, no. 15, pp. 3743–3754, Mar. 2017.

[121] Grell, M., D. D. C. Bradley, M. Inbasekaran, and E. P. Woo, "A glass-forming conjugated main-chain liquid crystal polymer for polarized electroluminescence applications," *Adv. Mater.*, vol. 9, no. 10, pp. 798–802, Jan. 1997.

[122] Perevedentsev, A., N. Chander, J.-S. Kim, and D. D. C. Bradley, "Spectroscopic properties of poly(9,9-dioctylfluorene) thin films possessing varied fractions of β-phase chain segments: enhanced photoluminescence efficiency via conformation structuring," *J. Polym. Sci. Part B Polym. Phys.*, vol. 54, no. 19, pp. 1995–2006, Oct. 2016.

[123] Caruso, M. E., S. Lattante, R. Cingolani, and M. Anni, "Microscopic investigation of the poly(9,9-dioctylfluorene) photoluminescence dependence on the deposition

conditions by confocal laser microscopy," *Appl. Phys. Lett.*, vol. 88, no. 18, p. 181906, May 2006.

[124] Honmou, Y., S. Hirata, H. Komiyama, J. Hiyoshi, S. Kawauchi, T. Iyoda, and M. Vacha, "Single-molecule electroluminescence and photoluminescence of polyfluorene unveils the photophysics behind the green emission band," *Nat. Commun.*, vol. 5, no. 1, p. 4666, Dec. 2014.

[125] List, E. J. W., R. Guentner, P. Scanducci de Freitas, and U. Scherf, "The Effect of Keto Defect Sites on the Emission Properties of Polyfluorene-Type Materials," *Adv. Mater.*, vol. 14, no. 5, p. 374, Mar. 2002.

[126] Hepp, A., H. Heil, W. Weise, M. Ahles, R. Schmechel, and H. von Seggern, "Light-Emitting Field-Effect Transistor Based on a Tetracene Thin Film," *Phys. Rev. Lett.*, vol. 91, no. 15, p. 157406, Oct. 2003.

[127] Santato, C., R. Capelli, M. A. Loi, M. Murgia, F. Cicoira, V. A. L. Roy, P. Stallinga, R. Zamboni, C. Rost, S. F. Karg, and M. Muccini, "Tetracene-based organic light-emitting transistors: optoelectronic properties and electron injection mechanism," *Synth. Met.*, vol. 146, no. 3, pp. 329–334, Nov. 2004.

[128] Roelofs, W. S. C., W. H. Adriaans, R. A. J. Janssen, M. Kemerink, and D. M. de Leeuw, "Light Emission in the Unipolar Regime of Ambipolar Organic Field-Effect Transistors," *Adv. Funct. Mater.*, vol. 23, no. 33, pp. 4133–4139, Sep. 2013.

[129] Redecker, M., D. D. C. Bradley, M. Inbasekaran, and E. P. Woo, "Mobility enhancement through homogeneous nematic alignment of a liquid-crystalline polyfluorene," *Appl. Phys. Lett.*, vol. 74, no. 10, pp. 1400–1402, Mar. 1999.

[130] Hsu, B. B. Y., J. Seifter, C. J. Takacs, C. Zhong, H.-R. Tseng, I. D. W. Samuel, E.

B. Namdas, G. C. Bazan, F. Huang, Y. Cao, and A. J. Heeger, “Ordered Polymer Nanofibers Enhance Output Brightness in Bilayer Light-Emitting Field-Effect Transistors,” *ACS Nano*, vol. 7, no. 3, pp. 2344–2351, Mar. 2013.

[131] Lu, H.-H., C.-Y. Liu, C.-H. Chang, and S.-A. Chen, “Self-Dopant Formation in Poly(9,9-di-n-octylfluorene) Via a Dipping Method for Efficient and Stable Pure-Blue Electroluminescence,” *Adv. Mater.*, vol. 19, no. 18, pp. 2574–2579, Sep. 2007.

[132] Scott, J. C. and L. D. Bozano, “Nonvolatile Memory Elements Based on Organic Materials,” *Adv. Mater.*, vol. 19, no. 11, pp. 1452–1463, Jun. 2007.

[133] Hsu, B. B. Y., C. Duan, E. B. Namdas, A. Gutacker, J. D. Yuen, F. Huang, Y. Cao, G. C. Bazan, I. D. W. Samuel, and A. J. Heeger, “Control of Efficiency, Brightness, and Recombination Zone in Light-Emitting Field Effect Transistors,” *Adv. Mater.*, vol. 24, no. 9, pp. 1171–1175, Mar. 2012.

[134] Ghosh, S., X.-Q. Li, V. Stepanenko, and F. Würthner, “Control of H- and J-Type π Stacking by Peripheral Alkyl Chains and Self-Sorting Phenomena in Perylene Bisimide Homo- and Heteroaggregates,” *Chem. - A Eur. J.*, vol. 14, no. 36, pp. 11343–11357, Nov. 2008.

[135] Spano, F. C. and C. Silva, “H- and J-Aggregate Behavior in Polymeric Semiconductors,” *Annu. Rev. Phys. Chem.*, vol. 65, no. 1, pp. 477–500, Apr. 2014.

[136] Zampetti, A., A. Minotto, B. M. Squeo, V. G. Gregoriou, S. Allard, U. Scherf, C. L. Chochos, and F. Cacialli, “Highly Efficient Solid-State Near-infrared Organic Light-Emitting Diodes incorporating A-D-A Dyes based on α,β-unsubstituted ‘BODIPY’ Moieties,” *Sci. Rep.*, vol. 7, no. 1, p. 1611, Dec. 2017.

[137] Fenwick, O., J. K. Sprafke, J. Binas, D. V. Kondratuk, F. Di Stasio, H. L. Anderson,

and F. Cacialli, “Linear and cyclic porphyrin hexamers as near-infrared emitters in organic light-emitting diodes,” *Nano Lett.*, vol. 11, no. 6, pp. 2451–2456, Jun. 2011.

[138] “Excitation Energy Transfer,” in *Molecular Fluorescence*, Weinheim, Germany: Wiley-VCH Verlag GmbH & Co. KGaA, 2012, pp. 213–261.

[139] Dey, A., A. Rao, and D. Kabra, “A Complete Quantitative Analysis of Spatio-Temporal Dynamics of Excitons in Functional Organic Light-Emitting Diodes,” *Adv. Opt. Mater.*, vol. 5, no. 2, p. 1600678, Jan. 2017.

[140] Howard, I. A., J. M. Hodgkiss, X. Zhang, K. R. Kirov, H. A. Bronstein, C. K. Williams, R. H. Friend, S. Westenhoff, and N. C. Greenham, “Charge Recombination and Exciton Annihilation Reactions in Conjugated Polymer Blends,” *J. Am. Chem. Soc.*, vol. 132, no. 1, pp. 328–335, Jan. 2010.

[141] Wallikewitz, B. H., D. Kabra, S. Gélinas, and R. H. Friend, “Triplet dynamics in fluorescent polymer light-emitting diodes,” *Phys. Rev. B*, vol. 85, no. 4, p. 045209, Jan. 2012.

[142] Wang, Z., F. Yuan, X. Li, Y. Li, H. Zhong, L. Fan, and S. Yang, “53% Efficient Red Emissive Carbon Quantum Dots for High Color Rendering and Stable Warm White-Light-Emitting Diodes,” *Adv. Mater.*, vol. 29, no. 37, p. 1702910, Oct. 2017.

9 Appendix

9.1 Appendix 1: EQE Calculation

Evaluation of the ratio of light detected by the photodetector (PD) over the overall emitted light in the forward direction (approximated to a semi-sphere).

$A_{PD} = \pi r^2 \rightarrow r = \sqrt{\frac{A_{PD}}{\pi}} = R\sin(\theta)$

$\theta = \tan^{-1}(\frac{r}{d})$

$A_{half-plane} = 2\pi R^2$ (hemisphere)

Detected Radiation (DR) is the ration between the photodiode area and the total emission area (in the forward direction) of the device - which is approximated to a hemisphere.

$$\text{Detected Radiation (DR)} = \frac{A_{PD}}{A_{half-plane}} = \frac{\pi R^2 \sin(\tan^{-1}(\frac{\sqrt{\frac{APD}{\pi}}}{d}))^2}{2\pi R^2} = \frac{\sin(\tan^{-1}(\frac{\sqrt{\frac{APD}{\pi}}}{d}))^2}{2}$$

With:
A_{PD} = area Photodiode
d = distance sample-photodiode
PD = photodiode
S = source

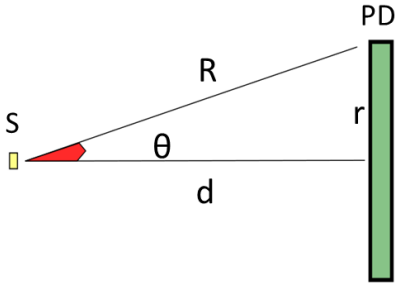

Figure 53: Estimation of the fraction of the emitted light impinging on the photodiode.

The value DR is corrected via factor (1 + R_c) which takes in account the cathode and capping layer reflectivity (R_c). Aluminium is approximated to a perfect mirror. The average wavelength of the device emission is calculated as follow to obtain the corresponding average detector responsivity:

$$\lambda_{av} = \frac{\int EL\ spectrum(\lambda) * \lambda\ d\lambda}{\int EL\ spectrum\ (\lambda)\ d\lambda}$$

$$\text{Average Det. Resp} = \frac{\int EL\ spectrum\ (\lambda) * Responsivity(\lambda)\ d\lambda}{\int EL\ spectrum(\lambda)\ d\lambda}$$

The emitted light power and the device external quantum efficiency (EQE) are calculated as follows:

$$\text{Light power (W)} = \frac{PD\ current}{preamp\ gain\ *\ Det.Resp.*Detected\ Radiation}$$

$$\text{EQE (\%)} = \frac{n\ emitted\ photons}{n\ electrons\ injected} = \frac{\frac{emitted\ light\ power}{average\ enrgy\ of\ photons}}{\frac{current\ in\ the\ device}{electron\ charge}} = \frac{light\ power * \frac{\lambda average}{10^9 c*h}}{\frac{I}{q}} *100$$

With:
I = Current flowing in the device (A)
Light power = Emitted light power (W)
c = 3 e^{8} m s^{-1}
q = 1.6 e^{-19} C
h = 6.63 e^{-34} m^2 kg s^{-1}

9.2 Appendix 2: Emitting device characterization code

```
import numpy as np

from tabulate import tabulate

from scipy.signal import savgol_filter

from scipy.interpolate import interp1d

import elaboration as el

import matplotlib.pyplot as plt

import pandas as pd

import Fitting as fit

import scipy.optimize as opt


def
oled(xspec,yspec,namespec,wi,wf,vdata,idata,phdata,ivname,ivlist,num=0
,step=1000,kind='linear',apix=4.5,\

      aphd=100,distdevph=50,preampgain=1e+6,actlayertk=100):


    # Constants

    #apix=a_pix         #area pxel in mm2
```

```
    #det_sens=detsens   #detector sensitivity in elec/photon
    #aphd=a_phd         #area photodiode in mm2   100mm2
    #distdevph          #distance device photodiode in mm
    # preamp gain
    # actlayertk activelayer thickness in nm

detectedoverleavinglight=((np.sin(np.arctan(((aphd/np.pi)**0.5)/distde
vph)))**2)

    ########### Cand per Watt calc
    ### Luminosity is the average human eye light sensitive
    ### SiliconResponse is the detector responsivity curve over the
electromagnetic spectrum

    xlum,ylum=np.genfromtxt('C:\\Users\\gcotella\\Python\\Reference
spectra\\Luminosity.dat',usecols=(0,1),delimiter='\t',unpack=True)

xsires,ysires=np.genfromtxt('C:\\Users\\gcotella\\Python\\Reference
spectra\\SiliconResponse.dat',usecols=(0,1),delimiter='\t',unpack=True)

    xlum_int,ylum_int=el.interp(xlum,ylum,wi,wf,step,kind)   # spectra
interpolation
    xsires_int,ysires_int=el.interp(xsires,ysires,wi,wf,step,kind)

    detect_resp=[]
```

```
    candperwatt=[]
    av_lambdas=[]
    curdens={}
    radiance={}
    eqe_100={}

    xloc=xspec[namespec[num]]
    nyloc=el.maxnorm(yspec[namespec[num]]) #norm spec
    xspec_int,yspec_int=el.interp(xloc,nyloc,wi,wf,step,kind)      #EL
interpolation

    aspec=el.area(xspec_int,yspec_int,[wi,wf])  #integral spectrum
    spec_sires=[a*b for a,b in zip(yspec_int,ysires_int)]  # product
spectrum*siresp
    aspec_sires=el.area(xspec_int,spec_sires,[wi,wf]) #integral product
    R0=aspec_sires/aspec # Detector response
    detect_resp.append(R0)

    spec_lum=[c*d for c,d in zip(yspec_int,ylum_int)]  #  procuct
spectrum*luminosity
    aspec_lum=el.area(xspec_int,spec_lum,[wi,wf]) # intgral product
    ratio=aspec_lum/aspec
    canwatt=(683.002/np.pi)*ratio # Candela per Watt
    candperwatt.append(canwatt)
```

```
    wave_spec=[a*b for a,b in zip(xspec_int,yspec_int)] # average EL
spectrum
    av_lambda=el.area(xspec_int,wave_spec,[wi,wf])/aspec #area spectrum
    av_lambdas.append(av_lambda)

    ############################

    for i in range(len(ivname)):

        lightnc=phdata[ivname[ivlist[i]]]
        light=[a-min(lightnc) for a in lightnc]

totlightmw=[(1e3*a)/(preampgain*RO*detectedoverleavinglight)for  a  in
light] #tot output

        lightareamwcm2=[100*a/apix for a in totlightmw] # for unit area
        lightareamwm2=[a*1e+4     for     a     in     lightareamwcm2]
#radiance plotted
        luminance=[(a/1000)*canwatt for a in lightareamwm2] #cd/m2
        radiance[ivname[ivlist[i]]]=lightareamwm2

        curr=idata[ivname[ivlist[i]]]
        volt=vdata[ivname[ivlist[i]]]
        currdensity=[1e+5*a/apix for a in curr] #ma/cm2               #
curr density plotted
        curdens[ivname[ivlist[i]]]=currdensity
```

```
        c=3e+8 #light speed in m/sec

        h=6.63e-34 # Plank's constat

        q=1.60e-19 #electron charge


        eqe=[((a/1000)*(av_lambda/(1e9*c*h)))/(b/q)    for    a,b    in
zip(totlightmw,curr)]

        eqe100= [a*100 for a in eqe]


        #elctricfield=[1e9*a/actlayertk for a in volt] #V/cm

        #efficacy=[a/b/10  for  a,b  in  zip(lightareacdm2,currdensity)]
#Cd/A

        #lumperwatt=[(a*np.pi)/(b*c)/10       for       a,b,c       in
zip(lightareacdm2,currdensity,volt)]



    return curdens,luminance,radiance,eqe_100
```